

Aqueous metallo-megasupramolecules: From stability to extensional flow properties

Thesis by
Jacqueline Rose Tawney

In Partial Fulfillment of the Requirements for the
degree of
Aerospace Engineering

CALIFORNIA INSTITUTE OF TECHNOLOGY
Pasadena, California

2025
Defended August 9th, 2024

© 2025

Jacqueline Rose Tawney
ORCID: 0000-0002-4276-0652

All rights reserved

*I dedicate this thesis to my guardian angel, my pap. I've never been more sure of
and more grateful for his eternal love guiding me towards the Dream.*

ACKNOWLEDGEMENTS

I am incredibly grateful for the support I have received during my time at Caltech. I want to start by thanking my caring, curious, and courageous mentor, Professor Julie Kornfield. Without Julie's guidance, encouragement, and compassion, I certainly would not have made it this far. She has taught me so many lessons that I will take far beyond the lab. I trust this is just the beginning for us.

Thank you to my committee, Prof. Mory Gharib, Prof. Jane Bae, Prof. Dan Meiron, and Dr. Chris Nelson. It truly warms my heart to have each of them participate in this. I am so grateful for their unique contributions to my graduate school journey as well as their perspectives on my thesis work. I am also so thankful for the GALCIT admin who enliven our space.

Thank you to the Kornfield group members—my fellow grad students, postdocs, undergrads, and our admin. They helped me in so many ways, from encouraging words of wisdom, sympathy, snacks, to turning off the GPC late at night so I could go home (even under precarious circumstances!). Special thanks to Red and Rob for laying the foundation of this work and helping make my interdisciplinary transition much more possible and fun.

Thank you to the Women in GALCIT, my fellow GGSC members, the Center for Inclusion and Diversity, and my co-facilitators and students in my *Advocacy* course. Each of these communities helped me push through challenges and grow into a compassionate leader and resilient community builder. They give me hope that it's possible to create a world we wish to live in at any scale.

Thank you to my parents, siblings, aunt and uncle, grandmothers, cousin/aunt/soul-sister, niblings, my many besties near and far that I hold dear, my Palmetto Drive casita and neighbors, the east coast for always welcoming me home, the west coast

for teaching me so much, my therapist, and my self! We did it!

A huge thank you to my husband, Gianfranco, and our cats, Pipo and Bueno. In the darkest of times, when I thought I'd never get this degree, I took the ultimate comfort in already having the greatest prize of all—true love <3

ABSTRACT

The addition of long, flexible polymers (> 1 Mg/mol) to a fluid is known to reduce turbulent drag and control droplet behavior, which has the potential to significantly enhance the efficiency of engineering flows across various industries, from agriculture to aviation. However, hydrodynamic forces can break the polymers and diminish their effectiveness, which is presently a major roadblock to their practical utilization in both applications and research. To address this challenge, the Kornfield group developed end-associative, self-healing polymers for use in fuel and, more recently, for use in water—aqueous terpyridine-ended polyacrylamide (TPAM) supramolecules. This thesis examines the relationships between the molecular structure of TPAM, the amount of metal provided to link pairs of chain ends, and kinetic processes of the resulting supramolecules and the rheological properties and performance they provide.

The most useful polymers for reducing turbulent drag, controlling mist, and tailoring droplet impact behavior have a combination of efficacy at low concentration (< 0.1 %wt), so they only mildly affect the shear viscosity ($< 2x$), and have long extensional relaxation time ($\lambda_E > 1$ ms), so that turbulent eddies or elongating fluid filaments cause them to stretch and elastically resist elongational flow. This thesis explores the fundamental nature of TPAM supramolecules and their potential utility as a rheological modifier, using measurements of their molecular weight distributions and the resulting extensional relaxation time (λ_E) as our primary sources of insight into the relationship between supramolecular structure and flow behavior. We examine the kinetics of redistribution of TPAM molecules among supramolecular species (equilibration) and the kinetics of chemical degradation of TPAM molecules, which cause a rise and fall of λ_E , respectively. This is the first report of the increase in λ_E as larger supramolecules form when the metal ions that link them are introduced to polymers

below their overlap concentration. Study of chemical degradation—desirable in the environment, but not during use—revealed that its rate can be controlled by limiting air exposure, avoiding an excess of metal ions relative to ligands, and storing samples in refrigerated conditions (4°C). Understanding the timescale for the crossover from equilibration to degradation combined with establishing methods to delay degradation for several weeks enables further exploration of TPAM’s structure-property relationships.

We assess how changes in metal-to-ligand ratios (M:L) and unimer lengths influence TPAM’s megasupramolecular size, equilibration and decay dynamics, and λ_E , revealing that lower than stoichiometric metal to ligand ratios (M:L < 1:2 for Ni²⁺ : terpyridine) promote more rapid stabilization of λ_E due to efficient exchange of metal ions when unoccupied ligands are available, while higher ratios (M:L > 1:2) exacerbate degradation (likely due to the catalytic effects of metal ions when they are not bound by ligands). We show that the presence of supramolecules that comprise over 10 unimers gives rise to a $\lambda_E \approx 2$ ms at 0.04 wt%, i.e., long and dilute enough to cause drag reduction. In accord with theoretical predictions, larger unimers have a disproportionate effect in promoting longer megasupramolecules, which further increases λ_E . In the interest of achieving even longer supramolecules (and thus longer λ_E) with the same amount of TPAM, we modify the solution preparation protocol by introducing metal ions to a more concentrated TPAM solution prior to dilution. This exposes new and intriguing topologies with M_w extending beyond the upper limits of our accessible measurement (10 Mg/mol), which expand the envelope of the longest accessible λ_E (from 2~ to 6~ ms with M:L = 1:2 for Ni(II):terpyridine). These complex supramolecules have three times the mass within the same pervaded volume compared to the supramolecules formed when metal is added after unimers are diluted below their overlap concentration. We evaluated their potential as chain scission-resistant, turbulent drag reducing agents. In their

initial state, they can reduce turbulent drag and keep their unimer backbones intact; however, their supramolecular structures and prolonged λ_E are not maintained after multiple passes through contraction flow, turbulent flow, and expansion flow. The fact that their backbones remain intact, in addition to the range of λ_E achieved with the more standard linear topologies (up to 3~ ms with 1 MDa unimers), suggests that TPAM is a viable option for a robust rheological modifier that warrants continued investigation. Our findings not only enhance our knowledge of TPAM's structural and rheological properties under a range of conditions, but we lay the groundwork for ongoing studies and collaborations that will continue to deepen our understanding of aqueous megasupramolecule dynamics and potential applications.

TABLE OF CONTENTS

Acknowledgements	iv
Abstract	vi
Table of Contents	ix
List of Illustrations	xi
List of Tables	xix
Nomenclature	xx
Chapter I: Introduction	1
1.1 Minute amounts of long flexible polymers can enhance engineering flows	1
1.2 Dripping-onto-Substrate Extensional Rheometry (DoSER)	11
1.3 Gel Permeation Chromatography (GPC)	13
1.4 Experimental Materials	14
1.5 Thesis Goals and Overview	15
Chapter II: Aqueous terpyridine-ended polyacrylamide instability characteri- zation and mitigation	20
2.1 Introduction	20
2.2 Initial rise in λ_E	27
2.3 Trithiocarbonate breakage through aminolysis	28
2.4 λ_E decay correlates to the presence of metal ions and exposure to air	31
2.5 Limiting exposure to air decreases the rate of decay of λ_E	34
2.6 Temperature dependence of λ_E decay	36
2.7 Conclusions and Future Work	45
2.8 Supplementary Figures	48
Chapter III: Exploring TPAM megasupramolecular weight distribution and relaxation time by varying metal-ligand ratios and building block size	52
3.1 Introduction	52
3.2 Metal-ligand ratio affects TPAM's associative M_w distribution and λ_E	64
3.3 Unimer M_n affects TPAM's associative M_w distribution and λ_E	72
3.4 TPAM megasupramolecular M_w and λ_E show an exponential power law relationship	79
3.5 Conclusions and Future Work	80
3.6 Supplementary Figures	81
Chapter IV: Expanding TPAM megasupramolecule topology and behavior by varying concentration when metal is added	87
4.1 Introduction: Changing concentration when metal is added changes the topology and behavior	87
4.2 Order of operations changes extensional behavior	91
4.3 Adding Ni(II) to TPAM before dilution reveals a topological wonder	99

4.4 TPAM reduces turbulent drag and resists chain scission, but Metal → Dilute molecules are not "self-healing"	106
4.5 Bulk drag reduction results for PEO, PAM, and TPAM	107
4.6 Conclusions and Future Work	111
4.7 Supplementary Figures	113
Chapter V: Conclusion	116
Chapter A: Quantifying uncertainty and sample reproducibility	119
Appendix B: Drag Reduction and Chain Scission Instrument Development . .	126
B.1 Experimental Methods	126
B.2 Initial PIV: Comparison to canonical flow, improvements, and under- resolved near-wall statistics	130
B.3 Identification of polymer-induced drag reduction structures	133
Appendix C: DoSER Equation Derivation for Determining λ_E	136
Bibliography	139

LIST OF ILLUSTRATIONS

<i>Number</i>	<i>Page</i>
1.1 Sketch of coiled, flexible polymers at their overlap concentration (c^*) (left) compared to a more dilute solution (right).	4
1.2 A sketch of a coiled polymer in equilibrium (left), being stretched out by an elongational force, and then relaxing again. The time it takes the polymer to relax back to its equilibrium configuration is called the "extensional relaxation time" or λ_E	5
1.3 Schematic of the different effects on polymers in shear flow (planar Couette) and extensional flow (parallel plates pulled apart). In mild shear flow, the polymer does not drastically deform. In extensional flow, the polymer is stretched end-to-end.	6
1.4 Instantaneous vorticity map of DI water ($Re_B = 5.2 \times 10^4$) and 6 Mg/mol PEO at 66 wppm ($Re_B = 7.5 \times 10^4$) ($\lambda_E \approx 2$ ms).	8
1.5 A cartoon of terpy-ended PAM (terpys shown as purple crescents) associating with a divalent metal ion (red circles) to form a longer linear species.	11
1.6 Schematic of the DoSER setup.	12
1.7 DoSER data showing the normalized change in the diameter of the filament (D/D_0) over time for DI water (green) and 6 MDa PAM at 200 wppm. The λ_E for the PAM solution shown here is 2.5 ms.	13
1.8 A sketch of the GPC traces (M_w distributions) that result from a distribution of large and small molecules.	14
2.1 Chemical structure of terpyridine-ended polyacrylamide (TPAM).	23

2.2	Sketch of (A) fully intact unimers and a few illustrative end-to-end supramolecules, and (B) putative structures of degraded unimers and their stunted end-to-end supramolecules.	25
2.3	Preliminary evidence of TPAM's temporal λ_E decay on a timescale of several days. [1]	26
2.4	Schematic illustrations of the initial bias in chain configurations that results when metal is added to a dilute solution of unimers ($c < c^*_{unimer}$).	27
2.5	First observation of a short-term rise in λ_E with a maximum around 1 day since metal added.	28
2.6	Evolution of GPC traces for 0.5 μM TPAM mixed with 20 μM ammonia. No change in M_w or degradation of the trithiocarbonate is observed over 12 days.	29
2.7	Evolution of GPC traces for 0.5 μM TPAM mixed with 100mM ammonia at pH 11. Within 12 hours, the trithiocarbonates have broken.	30
2.8	Evolution of M_n (solid bars) and M_w (hatched bars) for 0.5 μM TPAM mixed with 100mM ammonia, corresponding to the GPC traces in Figure 2.7.	30
2.9	Acetic acid buffer solvent protocol illustrating when metal is added to the polymer solution relative to the day the polymer was dissolved. All solutions were dissolved on $d_p = 0$, and metal was added to the solutions on $d_p = 5, 9, 19,$ and 26	32
2.10	MilliQ (un-buffered) solvent protocol illustrating when metal is added to the polymer solution relative to the day the polymer was dissolved. All solutions were dissolved on $d_p = 0$, and metal was added to the solutions on $d_p = 5, 21,$ and 27	32

2.11	Comparison between λ_E decay relative to the day the polymer was dissolved in an acetic acid buffer vs the day the metal was added to solution.	33
2.12	Comparison between λ_E decay relative to the day the polymer was dissolved in MilliQ water vs the day the metal was added to solution.	33
2.13	Illustration of the difference storage condition protocol	34
2.14	Comparison between λ_E decay when stored in a 20 mL plastic vial versus a 5 mL Luer lock syringe.	35
2.15	M_w distributions for TPAM solutions stored in vial versus syringe, indicating an evolution towards the unimer peak.	37
2.16	λ_E evolution over multiple weeks with samples stored at $T_{store} = 22^\circ\text{C}$, 40°C , and 4°C in MilliQ solvent.	40
2.17	Arrhenius plot used to approximate the activation energy of TPAM's chemical degradation mechanism(s).	41
2.18	λ_E evolution over time stored at 40°C with and without metal ions present in MilliQ solvent.	43
2.19	λ_E evolution over multiple weeks with samples stored at $T_{store} = 22^\circ\text{C}$, 40°C , and 4°C in HEPES solvent.	44
2.20	Comparison of λ_E short-term rise at different T_{store} : 4°C (refrigerator), 22°C (room temperature) and 40°C (incubator).	46
2.21	Protocol for mixing TPAM solutions with MEHQ alone vs with MEHQ and metal, implemented in attempt to assess whether or not an oxygen scavenger can mitigate decay induced by air exposure.	48
2.22	DoSER results for TPAM solutions with MEHQ oxygen scavenger, with no apparent harmful or helpful effect at the concentrations considered here.	48

2.23	The structure and concentration of neutral pH buffers, MOPS and HEPES, used in the present study.	48
2.24	DoSER results for TPAM solutions with MOPS and HEPES buffers. Both buffers limit the maximum λ_E	49
2.25	Protocol to collect aliquots from the GPC waste line.	49
3.1	Schematic of the dynamic equilibrium of megasupramolecular species that can exist given the same amount of unimer and metal ions.	55
3.2	An illustration of megasupramolecule formation from TPAM unimers.	57
3.3	By varying the M:L ratio (x-axis), we can create different respective amounts of free metals, ligands, and metal-ligand complexes (y-axis, normalized by the initial free ligand concentration L_0). The plot presented here is calculated for terpyridine and Ni(II) using the system of equilibrium and conservation equations given by Eqns 3.1 through 3.4).	59
3.4	Figure from Learsch [1] used with permission. It shows the relaxation time λ_E for covalent PAM with varying weight average molecular weight (M_w) and concentration.	63
3.5	M_w distributions collected with GPC for TPAM with NiCl ₂ added such that the M:L ratio = 0.25, 0.35, 0.4, 0.45, 0.5, and 0.75.	65
3.6	Evolution of λ_E for $M_{uni} = 0.84$ MDa unimers observed with respect to days since metal added (d_m) for M:L ratio = 0.25, 0.35, 0.4, 0.45, 0.5, 0.75, and 1.5.	69
3.7	Evolution of λ_E for $M_{uni} = 0.71$ MDa unimers observed with respect to days since metal added (d_m) for M:L ratio = 0.25, 0.35, 0.4, 0.45, 0.5, 0.75, and 1.5.	73

3.8	Evolution of λ_E for $M_{uni} = 1.0$ MDa unimers observed with respect to days since metal added (d_m) for M:L ratio = 0.25, 0.35, 0.4, 0.45, 0.5, 0.75, and 1.5.	74
3.9	GPC traces for three different unimer lengths (0.71, 0.84, and 1.0 MDa) with one Ni(II) ion added for every four terpys (M:L = 0.25).	76
3.10	Maximum λ_E values observed for each M:L ratio for each unimer M_n	77
3.11	λ_E versus M_w for each unimer M_n over their sweep of M:L = 0.25, 0.35, 0.4, 0.45, 0.5, and 0.75.	79
3.12	M_w distributions collected with GPC for 0.71 MDa TPAM with NiCl ₂ added such that the M:L ratio = 0.25, 0.35, 0.4, 0.45, 0.5, and 0.75.	82
3.13	M_w distributions collected with GPC for 1.0 MDa TPAM with NiCl ₂ added such that the M:L ratio = 0.25, 0.35, 0.4, 0.45, 0.5, and 0.75.	83
3.14	GPC traces for solutions of 0.04wt% aqueous TPAM for three different unimer lengths (0.71, 0.84, and 1.0 MDa).	84
4.1	GPC traces for TPAM with metal added at different concentrations (ranging 0.01 to 1 wt%) before the final dissolution to 0.01 wt%, normalized to the maximum signal height. (Reproduced, Kim 2022)	88
4.2	Sketch of TPAM at $c/c^* \approx 3.5$, which results in approximately 7 terpyridines present within the pervaded volume of one TPAM.	89
4.3	Sketch of the adapted Metal \rightarrow Dilute protocol to test effect of order of operations.	91
4.4	DoSER results for the filament diameter changing over time for solutions prepared with Metal \rightarrow Dilute protocol versus Dilute \rightarrow Metal protocol, and M:L = 0.5 and 1.5.	92
4.5	λ_E for Metal \rightarrow Dilute protocol for M:L ratio = 0.5, 0.75, 1, 1.5, 2, and 3 from $d_m = 0.25$ to 6.	93

4.6	λ_E evolution over days since metal added for solutions prepared with Metal \rightarrow Dilute protocol with Ni(II) added such that M:L = 0.25, 0.5, 0.75, 1, and 2.	95
4.7	λ_E evolution over days since metal added at different storage temperatures (40°C, 22°C, and 4°C) for Metal \rightarrow Dilute protocol.	97
4.8	λ_E evolution over time for solutions prepared at Metal \rightarrow Dilute versus Dilute \rightarrow Metal.	98
4.9	GPC results for solutions prepared at Metal \rightarrow Dilute versus Dilute \rightarrow Metal, indicating a 3x difference in M_w at the same elution time for the different protocols.	100
4.10	A speculative sketch of what the topology of the current TPAM supramolecules might look like with Metal \rightarrow Dilute protocol.	100
4.11	A comparison between the GPC traces for Kim's 0.45 μm syringe filtered solutions (HK Filtered) versus the current solutions, both filtered (JRT Filtered) and not (JRT No Filter).	102
4.12	A sketch of the fractionation of polymers with microfiltration.	104
4.13	GPC curves on the original, retentate, and filtrate solutions.	105
4.14	Percent change in λ_E for the retentate and filtrate within 0.22 and 0.45 μm centrifuge filters, compared to the original unfiltered solution.	105
4.15	Re_B changes with pass through the system for 66 wppm 6 MDa PEO and 6.7 MDa PAM, and 200 wppm TPAM prepared with M:L = 0.5 using Metal \rightarrow Dilute protocol.	108
4.16	λ_E changes with pass through the system for 66 wppm 6 MDa PEO and 6.7 MDa PAM, and 200 wppm TPAM prepared with M:L = 0.5 using Metal \rightarrow Dilute protocol.	110

4.17	GPC traces change with pass through the system for 200 wppm TPAM prepared with M:L = 0.5 using Metal → Dilute protocol, but the unimers remain intact.	111
4.18	λ_E evolution over days since metal added at different storage temperatures (22°C and 4°C) for Metal → Dilute protocol mixed with M:L = 1.5.	113
4.19	Shear viscosity measurements for MilliQ (no TPAM), TPAM unimers, TPAM + Ni(II) solution with Dilute → Metal protocol, and TPAM + Ni(II) solution with Metal → Dilute protocol.	114
A.1	Protocol for assessing variability between different higher concentration starting solutions ("parents") and their diluted + metal added megasupramolecular "child" solutions.	120
A.2	λ_E over days since metal added for replicate solutions from two different parent solutions in acetic acid buffer (pH 5.6).	121
A.3	λ_E over days since metal added for replicate solutions from two different parent solutions in MOPS buffer (pH 7).	122
A.4	λ_E over days since metal added for three different solvents: unbuffered MilliQ, acetic acid (pH 5.6), and MOPS (pH 7).	122
A.5	λ_E over days since metal added for replicate solutions from four different parent solutions in unbuffered MilliQ water (typical pH range of 5.6 to 6.8).	124
A.6	Box and whisker plots for the statistics of λ_E variation on $d_m = 1$ for three different solvents: unbuffered MilliQ (4 parent solutions, $n_{samples} = 10$), acetic acid (pH 5.6) (2 parent solutions, $n_{samples} = 10$), and MOPS (pH 7) (2 parent solutions, $n_{samples} = 7$).	125

B.1	Schematic of the drag reduction instrument, adapted from a DOW 2017 review by Dr. Ryan McMullen, Dr. David Huynh, and Dr. Red Lhota.	127
B.2	First round of non-dimensionalized mean velocity and variance profiles of water at $Re_B = 5.2$, based on PIV data taken with the first calibration target	131
B.3	Original vs new calibration target	132
B.4	Improved non-dimensionalized mean velocity and stream-wise variance profiles.	132
B.5	Stream-wise variance data compared to adjusted reference profile. 50% overlap, 98x98 pixel resolution ($y+$ SR 50. [5])	133
B.6	Instantaneous vorticity map of DI water ($Re_B = 5.2 \times 10^4$).	134
B.7	Instantaneous vorticity maps of 6M PEO during the first pass through the drag reduction instrument ($Re_B = 7.5 \times 10^4$).	135

LIST OF TABLES

<i>Number</i>	<i>Page</i>
3.1 Summary of molecular weight distributions for a solution of 0.04 wt% 0.84 MDa unimers in un-buffered MilliQ water at various M:L ratios.	67
3.2 Summary of molecular weight and mass fraction data for M:L ratio = 0.25 for the various unimer M_n	75
B.1 Molecular weights (weight average and number average) for the polymers discussed in this chapter. HK: Synthesized by Dr. Hojin Kim. .	128

NOMENCLATURE

η_E	extensional viscosity
η_S	shear viscosity
λ_E	Relaxation time
c	concentration
c^*	overlap concentration
d_m	days since metal added
M_n	Number-averaged molar mass
M_w	Weight-averaged molar mass
M_{uni}	Unimer M_n
n_{drops}	number of droplets taken during one DoSER experiment
T_s	storage temperature
DoSER	Dripping-onto-substrate extensional rheometry
M:L	metal to ligand ratio
MilliQ	water from a Millipore Direct-Q 3 purification system
PDI	Polydispersity index (M_w/M_n)
terpy	terpyridine ligand
TPAM	terpyridine-ended polyacrylamide
wppm	weight parts per million (mg/L)
wt%	weight percent (g polymer/g solvent)

Chapter 1

INTRODUCTION

1.1 Minute amounts of long flexible polymers can enhance engineering flows**1.1.1 Drag reduction and droplet control with long, linear, flexible polymers**

Engineers and researchers are on a continuous mission towards more efficient and sustainable systems. Turbulent drag and uncontrolled droplet size are both barriers towards greater efficiency across various industries, from agriculture to aviation. Long, linear, flexible polymer flow additives are capable of mitigating and controlling these factors to enhance flow properties at dilute concentrations, eliciting a practically relevant as well as fundamentally interesting phenomena. A precise description of these "long, linear, flexible, and dilute" polymers, their behavior within the flow, and practical challenges limiting their widespread implementation will be given in the following sections. First, a description of their well-established potential in turbulent drag reduction and droplet control is provided.

Turbulent drag reduction

Turbulent drag, through its chaotic motion and viscous dissipation, causes significant energy losses when transporting fluids across long distances or circulating within a closed system. Long-chain polymers' drag-reducing properties were discovered by accident when Toms was intending to investigate polymeric degradation (which, as we will soon discuss, is still very relevant to the field presently) [1]. Since then, an asymptotic maximum of 80% bulk drag reduction has been achieved with polymers ranging O(1-10) MDa in just O(10-100) weight parts per million (wppm) [2]. This is a massive reduction in drag forces, and thus a massive decrease in energy required to transport a fluid at a given rate (or rather, an increase in flow rate with the same

energy input). The applications for polymer drag reduction (PDR) are plentiful, including pipelines [3], hydraulic fracturing [4], sewage systems [5], irrigation [6], firefighting [7], and even biomedical engineering [8, 9].

Droplet control

Agricultural sprays consist of droplets that supply plants with pesticides and nutrients, but it's known that less than 50% of these chemicals are actually deposited onto the target crops [10]. Droplets that are too large may immediately bounce off the plant leaves, while droplets that are too small can blow away to neighboring farms or nearby residential areas [11]. A U.S. Geological study found that over 90% of the time, pesticides can be found in agricultural, urban, and mixed-land-use streams, while for shallow wells and major deep aquifers, they can be found 50% and 33% of the time [12]. Due to their toxicity and pervasiveness, there have been calls to limit pesticide use. Controlling the droplet deposition on crops has immediate and obvious benefits in terms of creating a safer, cleaner environment, but it could also have major economic impacts. In 2008, it was reported that U.S. farmers spent a total of \$12 billion on pesticides alone, while in 2014 that number reached nearly \$54 billion worldwide [13]. Other interesting applications for understanding and controlling droplet deposition include coating materials, viral droplet spreading, and jet fuel mist-suppression [14].

1.1.2 What do we mean by "polymers", "minute", "long", and "flexible"?

Polymers are everywhere. The first man-made polymer was developed in 1869 as a substitute for limited natural materials such as ivory, and by the turn of the century, we entered "The Polymer Age" [15]. "Polymers" might immediately bring to mind materials such as plastic bags, Styrofoam, or any number of solid plastic objects pervading our modern world. But polymers can also be dissolved in complex solutions to elicit useful properties, such as in glue and nail polish. Polymers are

also commonly found in nature, such as those found in natural rubber, silk, spit, cellulose, and even DNA. The unifying property is that all these materials are chains of many, repeated chemical units called "monomers". In fact, the word "polymer" stems from "poly" meaning "many", and "mer" meaning "parts"—a polymer is a molecule with many (repeating) parts. Different polymer structures (for example, type of atoms that comprise the main chain, or any side or end groups attached to the main chain) result in different material properties.

When we refer to polymers in terms of them being "flexible", "minute amounts", and "long", what do we mean, specifically? "Flexible polymers" are linear chains that exist in a coiled configuration at equilibrium, and when external extensional forces are applied, they can be stretched from end-to-end. "Minute amounts" means the polymers are within the "dilute" regime at a low concentration. Specifically, polymer solutions are considered "dilute" based on the overlap concentration (c^*), shown in Figure 1.1. The coiled polymers are contained within their pervaded volume, and when the pervaded volumes of each coiled polymer begin to touch each other, the overlap concentration has been reached. In the present work, we focus primarily on concentrations below c^* , the dilute regime where the coils do not overlap. We also focus on aqueous polymers, which can be dissolved in water, as opposed to polymers that are only soluble in hydrocarbon-based fluid solvents.

"Long" typically means the linear polymer has a molecular weight equal or greater to 1,000,000 g/mol (units of g/mol is also referred to as Daltons or "Da"). To give a better physical understanding, that is on the order of approximately 10,000 repeat chemical units, a 50 nm radius of gyration (R_g) in the coiled state, or $O(1)$ μm in the extended state.

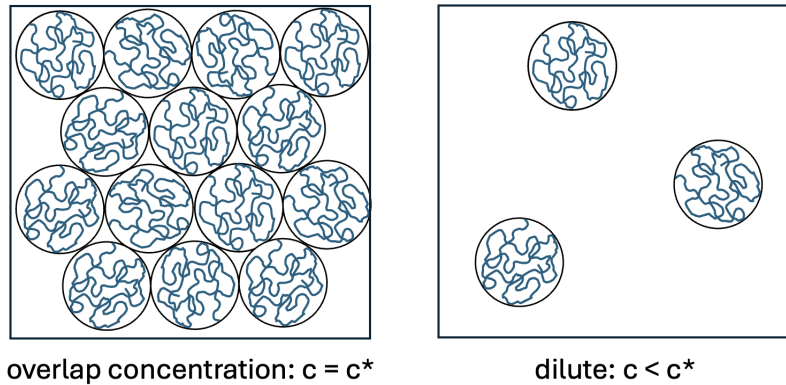


Figure 1.1: Sketch of coiled, flexible polymers at their overlap concentration (c^*) (left) compared to a more dilute solution (right).

1.1.3 Long, flexible, dilute polymers in extensional flows

When an extensional force acts upon the long, flexible polymer in its coiled state in a dilute solution, the polymer stretches out. The time it takes for the polymer to relax back to its coiled equilibrium state from being fully stretched out is called the "extensional relaxation time" or λ_E (sketched in Figure 1.2). Generally, the longer the polymer, the higher the value of λ_E , which results in a higher extensional viscosity (η_E) and interesting (non-Newtonian) behavior. At this point, an astute reader might wonder how *increasing* viscosity leads to a *decrease* in friction and reduction of turbulent drag. The emphasis here is on *extensional* viscosity (η_E) that is most relevant under extensional flows. Extension is evident in flows through expansions, contractions, or jets, but perhaps less obvious, it is also prevalent in turbulent eddies. We describe the difference between non-Newtonian flows in the shear and extensional regimes, and how long, flexible, dilute polymers do, in fact, alter the flow in such a way that increases a turbulent fluids' ability to flow faster with less energy loss.

In mild shear flows, a coiled polymer tends to tumble along, experiencing minimal deformation to its conformational structure, and thus making a minimal impact on the flow behavior. It is the stretching out, or elongating, of the polymer structure that

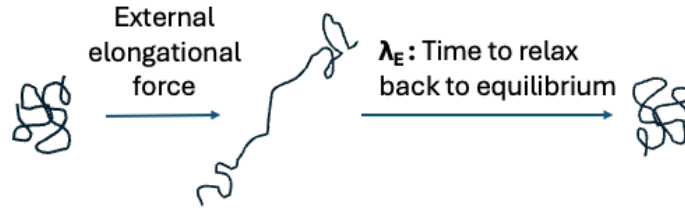


Figure 1.2: A sketch of a coiled polymer in equilibrium (left), being stretched out by an elongational force, and then relaxing again. The time it takes the polymer to relax back to its equilibrium configuration is called the "extensional relaxation time" or λ_E .

elicits exciting behavior (Figure 1.3). Resistance to shear deformation is quantified by the well-known shear viscosity (η_S), while resistance to elongational deformation is called extensional or elongational viscosity (η_E). In a typical Newtonian flow, η_E can be readily determined if η_S is known, thanks to the (Newtonian) Trouton ratio: $\frac{\eta_E}{\eta_S} = 3$ [16]. The validity of this simple scaling of the Trouton ratio depends on the linear relationship between shear stress (τ_S) and velocity gradient ($\frac{du}{dy}$) that is apparent in Newtonian fluids ($\tau_S = \eta_S \frac{du}{dy}$). In non-Newtonian flow, like that of polymer solutions, the relationship between shear stress and velocity gradient is nonlinear, which invalidates the aforementioned Trouton ratio of $\eta_E = 3 \eta_S$. In fact, in dilute solutions of long, flexible polymers, η_E can be $10^3 - 10^5$ times greater than η_S [17]. Reliable characterization of a dilute solution's extensional rheology has been a long-standing challenge, but in 2015, Vivek Sharma and coworkers at the University of Illinois at Chicago introduced the experimental technique, Dripping onto Substrate Rheometry (DoSER) [18], which we have implemented and will discuss in detail later in this chapter.

1.1.3.1 How do polymers reduce turbulent drag?

A detailed description of the precise mechanism(s) that relate the micro-scale molecular structures and the macro-scale bulk fluid behavior is still a widely discussed and debated topic, especially as it pertains to turbulent drag reduction [19]. Part

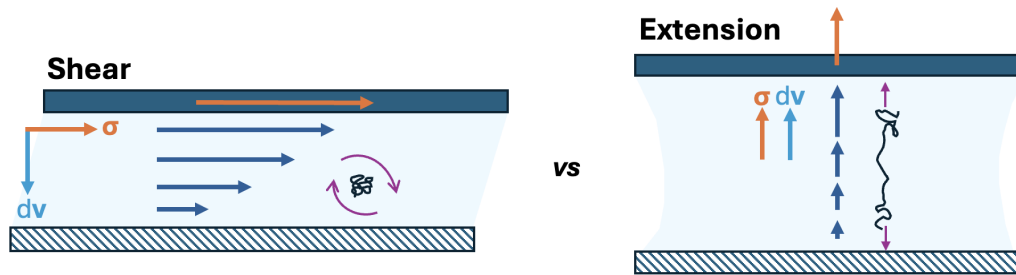


Figure 1.3: Schematic of the different effects on polymers in shear flow (planar Couette) and extensional flow (parallel plates pulled apart). In mild shear flow, the polymer does not drastically deform. In extensional flow, the polymer is stretched end-to-end.

of the challenge is the truly interdisciplinary nature of the problem; polymers have their own complex conformational behavior, while turbulence is known as "the most important unsolved problem of classical physics" (according to Richard Feynman). Whether or not this statement rings true, turbulence is chaotic and inherently challenging, and with the added coupled dynamics of polymer additives, the complexity only increases. Still, great strides have been made by both fluid dynamicists and polymer physicists alike. Many reviews have been published over the years, as researchers have begun to uncover compelling clues, inching the field towards a greater understanding of the underlying mechanism(s) [2, 20, 19, 21, 22].

The seminal review by Virk (1975) illuminated some of the fundamentally accepted influences of polymers on turbulent flow [2]. The statistically observable changes due to the presence of polymers include reduced wall friction, increased buffer layer thickness, and an increasing and changing shape of the log-layer with increasing drag reduction. The log-layer is the region of the flow where, independent of Reynolds number (Re), the velocity profile scales logarithmically with distance from the wall. This is known as "the law of the wall" [23]. The fact that the presumed universal slope and shape is altered suggests underlying dynamical differences in the flow, which have more recently been illuminated by advances in full-field visualization techniques such as particle image velocimetry (PIV) [20] as well as modeling tools

such as direct numerical simulation (DNS) [24].

Drag reduction has been observed for a range of polymer types, indicating that the phenomenon is a mechanical interaction between the polymers and the fluid structure rather than a chemical influence. There are two interpretations of the mechanistic relationship, one considered the "viscous" interpretation [25], and the other the "elastic" interpretation [26]. Both interpretations acknowledge that polymers disrupt the cascade of energy from larger to smaller scales that leads to velocity fluctuations and viscous dissipation. It has been observed experimentally and through modeling that polymers reduce the velocity fluctuations and suppress the generation of turbulence [19]. Both interpretations also involve the Weissenberg number (Wi), which is defined as the ratio of the elastic timescale (λ_E) to a characteristic timescale of the flow (often considered the inverse of the extension rate). As polymers stretch out, they store elastic energy, which is believed to remove energy from the fluctuations and "dampen" the turbulent eddies that contribute to dissipation. To get a sense of the changing flow structures, we turn to our PIV results which are also presented in Appendix B (Figure 1.4).

We compared the vorticity fields of deionized (DI) water and polymeric-induced drag reduction using polyacrylamide (PAM) at a concentration of 66 ppm. The experiments were conducted at 40 PSI, resulting in a bulk Reynolds number (Re_B based on mean velocity and pipe diameter) of 53,000 for DI water and 75,000 for the 66 wppm 6 MDa PEO solution. For DI water, the vorticity field exhibits a multitude of small vortices near the wall, indicative of the turbulent nature of the flow. These small-scale vortices are characteristic of high turbulence intensity and energy dissipation near the boundary layer. However, the introduction of PAM at 66 ppm not only increases the flow rate by 30%, but it also alters the vorticity structure. Consistent with the findings of AbdeIKader et al. (2022) [27] and Zadrazil et al. (2012) [28], the drag reduction run reveals a clear reduction in the number of

small-scale vortices. Instead, the flow exhibits high-strength, more coherent, and elongated inclined shear layers.

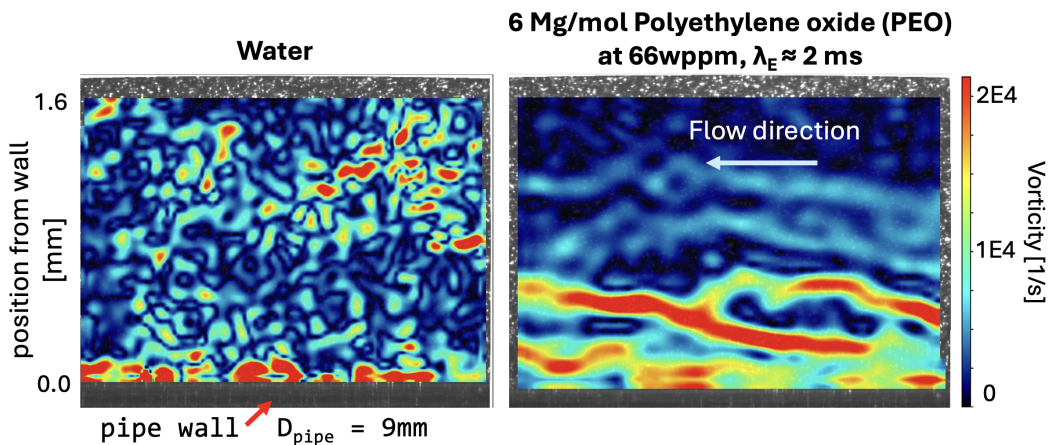


Figure 1.4: Instantaneous vorticity map of DI water ($Re_B = 5.2 \times 10^4$) and 6 Mg/mol PEO at 66 wppm ($Re_B = 7.5 \times 10^4$) ($\lambda_E \approx 2$ ms).

A polymer's ability to stretch and influence the flow is related to their λ_E , which can be modified by varying the type of polymer, its molecular weight (M_w) or its concentration. Higher λ_E (or higher Wi) generally results in greater drag reduction abilities when the solution is dilute (i.e. a minimal effect on η_S); however, it should be noted that this relationship is not linear as it approaches the maximum drag reduction asymptote [29]. To give a sense of scale for the direct influence of λ_E , in the case of one particular channel flow study with polyacrylamide (PAM) by Shaban et al. (2018), as polymer relaxation time increased between 2.6 ms, 3.7 ms, 15.5 ms, to 23 ms (by varying the concentration between 10 - 160 ppm), the respective percent drag reduction increased from 23%, to 42 %, to 50%, up to 60% (what they claim to be the maximum for their system) [29]. This illustrates the significance of λ_E , but here, it comes at a cost of increasing concentration. Higher λ_E can also arise from higher M_w polymers, but increasing M_w comes at the cost of increased susceptibility to chain scission. Owolabi et. al (2017) directly connects the reduction of M_w due to chain scission of PAM (caused by pumping) to a decrease in Wi and drag reduction [30].

1.1.4 Chain scission decreases polymer effectiveness and flow controllability

One of the major obstacles to the many practical applications of long, flexible, linear polymer flow-modifier additives is that high elongational stresses can ultimately degrade the polymers via mechanical scission, decreasing their molecular weight and subsequently their relaxation time and effectiveness [31, 32]. The extensional forces on a polymer may break the covalent bonds causing irreversible damage. It is well understood that the larger the polymer molecular weight, the higher the effective polymer relaxation time and drag reduction, but also the more susceptible the backbone is to breakage [33]. More recently, it has been shown that broader molecular weight distributions have a higher initial impact on drag reduction, but the distribution quickly narrows to due scission of the largest molecules first [34]. While it is valuable to gain fundamental insight on the multifaceted dynamics driving polymer scission, it is equally important that we take steps to mitigate it. Of course, mitigation of chain scission would benefit their effectiveness and efficiency within a wide range of applications, but the benefit would go even deeper than that. In a recent review by Saeed et al. (2023), they highlight the significance of overcoming mechanical chain scission to enable the future of polymeric drag reduction studies [21]. They state that the major outstanding fundamental questions all point towards needing higher Reynolds number tests ($> 10^6$) that focus on the modification of coherent structures that occur due to polymeric drag reduction. However, these experiments are hindered by the fact that the high shear rates in high Re flows can detrimentally induce polymer chain scission [31]. In order to obtain reliable, robust data with a uniform and controlled polymeric condition, we need polymers that can resist chain scission and maintain a constant M_w distribution. This leads us to the star of the current work—end-associative, chain scission resistant megasupramolecules.

1.1.5 End-associative megasupramolecules to combat chain scission

Supramolecules are formed through the self-assembly of smaller molecules via reversible, non-covalent associations, such as hydrogen bonds [35], host-guest interactions [36], or as in our case, metal-ligand coordination. The smaller molecules that comprise supramolecules are referred to as “unimers” in this context, analogous to the monomers that form covalently bonded polymers. The study of supramolecules is vast—there is a plethora of research on supramolecules since their discovery over three decades ago [37, 38, 39]. The evidence that supramolecules are self-healing was a seminal result and has largely been studied in the context of cross-linked gels and rubber [40]. Inspired by the pressing issue of mist control in fuel applications, the first end-associative polymers in the Kornfield group were soluble in hydrocarbon-based fluids and clearly exhibited their ability to control mist and suppress fire [14]. To provide relevant context for the present investigation, we focus in on long, linear, molecules in dilute, aqueous solutions that associate end-to-end through metal-ligand bis-complexes, or "metallo-megasupramolecules".

To combat the challenge of mechanical chain scission in aqueous flows, the Kornfield group developed water-soluble polymers with transient, reversible metal-ligand linkages that allow the polymers to pull apart and reattach under high stress, maintaining their large effective molecular weight [41]. These polymers are made up of polyacrylamide backbones (PAM, 1 Mg/mol) with terpyridine ligands (terpys) attached to the end; when mixed with metal ions, the terpyridines complex the metal, and the unimers link together to form much larger megasupramolecules (5 Mg/mol). The benefit to these metal-ligand associations is that they are reversible, or "self-healing": the polymers still break apart under high stress, but they can re-attach with another metal in solution and maintain their effective large molecular weight.

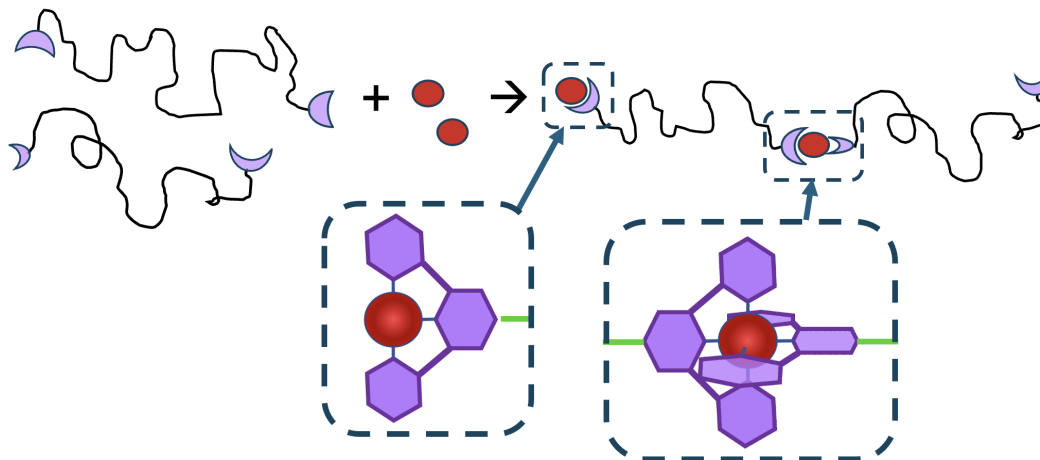


Figure 1.5: A cartoon of terpy-ended PAM (terpys shown as purple crescents) associating with a divalent metal ion (red circles) to form a longer linear species.

1.2 Dripping-onto-Substrate Extensional Rheometry (DoSER)

Dripping onto Substrate Extensional Rheometry (DoSER) is an experimental method used to determine the polymer relaxation time, λ_E , in dilute solutions. The DoSER method is especially useful for solutions with a relatively low relaxation time that may not be captured by more standard or commercial methods such as capillary breakup rheometry (CaBER). As discussed previously in this Introduction, λ_E is a key parameter when describing polymer viscoelastic behavior. Physically, it represents the time it takes for a polymer to recoil into its equilibrium state after being stretched by elongational forces (illustrated in Figure 1.2), and often in practice it's used to calculate non-dimensional numbers that dictate flow behavior, such as Weissenberg number (Wi) which relates the timescale of relaxation to a characteristic timescale of the flow. DoSER was introduced by Vivek Sharma and coworkers [18, 42], and the experimental apparatus design and construction of the present setup is detailed in Dr. Rob Learsch's thesis [43]. A schematic of the DoSER apparatus is shown in Figure 1.6.

In the DoSER method, four primary forces can be at play: inertial, viscous, surface tension (capillary), and elastic. We can determine the polymer relaxation time based

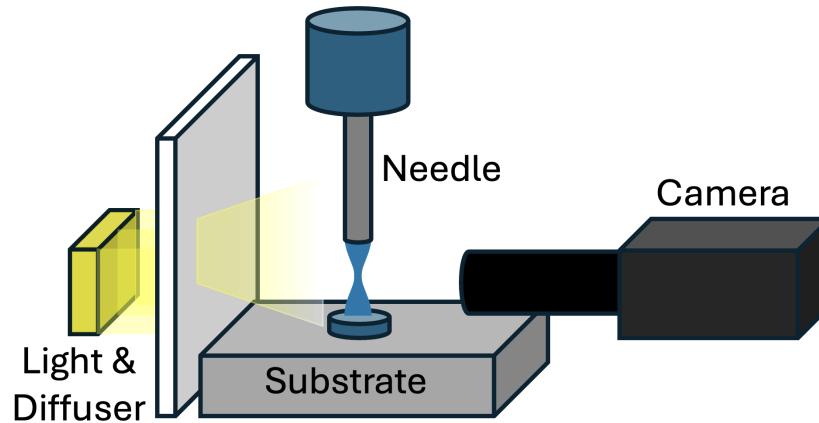


Figure 1.6: Schematic of the DoSER setup.

on observations of the solution's behavior in the elasto-capillary (EC) regime. Prior to the EC regime, fluids can exhibit either inertio-capillary (IC) or visco-capillary (VC) behavior, which can be determined from the Ohnesorge number ($Oh = \frac{\eta}{\sqrt{D_0 \rho \sigma}}$). Oh quantifies the ratio of viscous to elastic forces, where η is viscosity, ρ is density, σ is surface tension, and D_0 is a characteristic length scale. For our aqueous solutions dissolved in pure water, the solutions fall within the IC regime before transitioning to EC.

During a DoSER experiment, a small ($10 \sim \mu\text{L}$) droplet of polymer solution is dispensed from a needle of known diameter (D_0), and gravity pulls the droplet towards a substrate. As the droplet lands on the substrate, it spreads and then retracts due to a balance of inertia, surface tension, and viscosity. For the dilute polymer solutions that are of interest to us, a "liquid bridge" forms as the fluid transitions into the elasto-capillary regime, and this moment is called the critical time, or t_c . This liquid bridge, or filament, is formed between the needle and the substrate, and a high speed camera is used to observe the evolution of the filament diameter over time (Figure 1.7). Equation 1.1 is the relationship used to determine the relaxation time, λ_E , based on the slope of the filament diameter (D_{EC}) changing in time, where G is the elastic modulus. The derivation for Equation 1.1 is provided

in Appendix C.

$$\frac{D_{EC}(t)}{D_0} \approx \left(\frac{GD}{2\sigma} \right)^{1/3} \exp\left(-\frac{t}{3\lambda_E}\right) \quad (1.1)$$

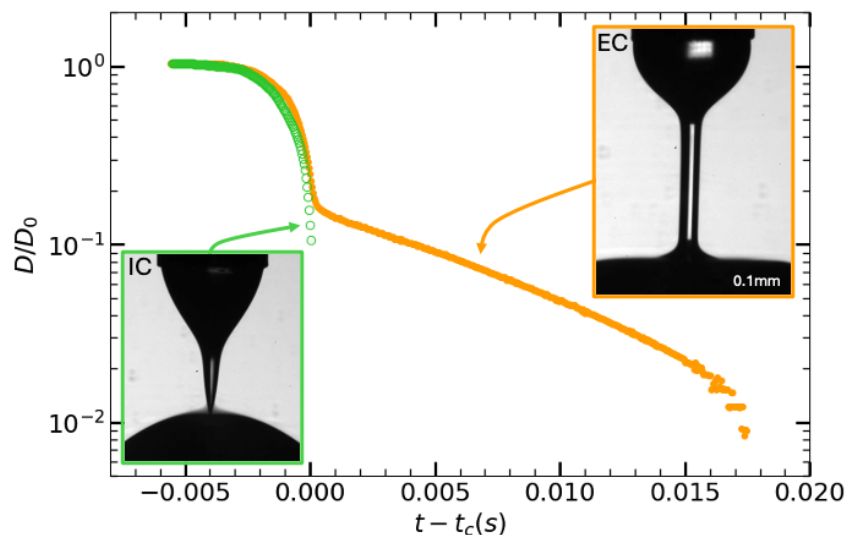


Figure 1.7: DoSER data showing the normalized change in the diameter of the filament (D/D_0) over time for DI water (green) and 6 MDa PAM at 200 wppm. The λ_E for the PAM solution shown here is 2.5 ms.

1.3 Gel Permeation Chromatography (GPC)

The polymer molecular weights and polydispersity indices ($PDI = M_w/M_n$) were measured using a GPC system. GPC is also known as "size exclusion chromatography", as it elutes molecules at different times based on size through a porous column. Larger molecules elute first, while smaller molecules take a different path through more pores, slowing down their elution time relative to their size (Sketched in Figure 1.8). Light scattering is used to detect the size of the molecules, while refractive index measurements are used to detect the relative amounts. As we will learn in Chapter 3 and 4, there is an upper limit to the GPC measurements, and any molecules that exceed the size limitation will be eluted at once, as the first molecules start eluting.

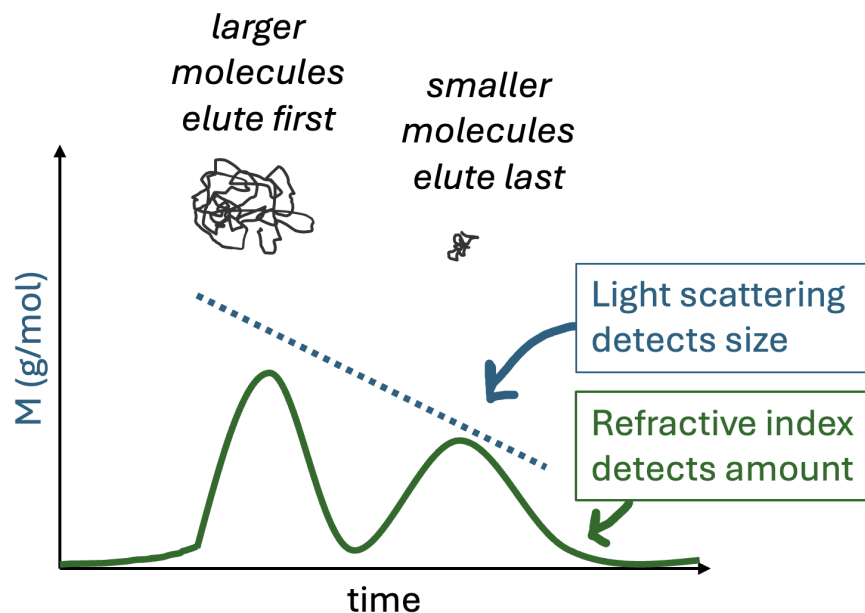


Figure 1.8: A sketch of the GPC traces (M_w distributions) that result from a distribution of large and small molecules.

1.4 Experimental Materials

DoSER: A GSVitec MultiLED G8 with QT lamp head was used as a light source. A Harvard Elite 11 syringe pump controlled the droplet rate at 0.2 mL/min from a 22G needle on a 5 mL Luer lock syringe. A Photron FASTCAM Nova S12 type 1000K-M-32GB was operated at 25,000 frames per second.

GPC: The GPC system contains an Agilent PL Aquagel-OH Mixed-H $8\mu\text{m}$ 300 x 7.5mm column, a Wyatt DAWN 8 multi-angle laser light scattering detector, and a Waters Optilab differential refractometer. The eluent used was DI water containing 200 ppm sodium azide and 8.5 g/L sodium nitrate with a flow rate of 0.3 mL/min at 25°C. The data analysis was conducted with Wyatt Astra Software using the Zimm fitting model (unless otherwise noted), with a dn/dc value of 0.159 mL/g for PAM in water.

1.5 Thesis Goals and Overview

The goals of this thesis center around exploring the fundamental nature of end-associative, self-healing, aqueous terpyridine-ended polyacrylamide (TPAM) and its potential utility as rheological modifier. In Chapter 2, we observe an initial rise in λ_E after the addition of metal at concentrations below overlap, and we identify factors that contribute to chemical degradation that causes its eventual decay. We develop protocols to achieve more stable solutions, enabling us to further explore TPAM behavior in Chapters 3 and 4. In Chapter 3, we assess the effect of varying the metal-to-ligand ratio and unimer length on TPAM megasupramolecular topology, equilibration and decay dynamics, and extensional relaxation time. In Chapter 4, we change the solution preparation protocol by first adding metal to a more concentrated TPAM solution before diluting to the lower concentration that was assessed in Chapter 3. The change in protocol reveals new and complex topologies that unlock significantly longer relaxation times. We further investigate the molecules made in Chapter 4 by assessing their potential as a chain scission-resistant turbulent drag reducer.

References

- [1] B. A. Toms. “Some observations on the flow of linear polymer solutions through straight tubes at large Reynolds numbers”. In: *Proceedings of the International Congress on Rheology II* (1949), pp. 135–141.
- [2] P. S. Virk. “Drag reduction fundamentals”. In: *AIChE Journal* 21.4 (July 1975), pp. 625–656. ISSN: 0001-1541, 1547-5905. DOI: [10.1002/aic.690210402](https://doi.org/10.1002/aic.690210402).
- [3] E.D. Burger, W.R. Munk, and H.A. Wahl. “Flow Increase in the Trans Alaska Pipeline Through Use of a Polymeric Drag-Reducing Additive”. In: *Journal of Petroleum Technology* 34.2 (Feb. 1, 1982), pp. 377–386. ISSN: 0149-2136, 1944-978X. DOI: [10.2118/9419-PA](https://doi.org/10.2118/9419-PA).
- [4] Ke Xu et al. “Progress of Development and Application of Drag Reduction Agents for Slick-Water Fracturing”. In: *Journal of Physics: Conference Series* 2097.1 (Nov. 1, 2021), p. 012022. ISSN: 1742-6588, 1742-6596. DOI: [10.1088/1742-6596/2097/1/012022](https://doi.org/10.1088/1742-6596/2097/1/012022).
- [5] Rhj Sellin. “INCREASING SEWER CAPACITY BY POLYMER DOSING.” In: *Proceedings of the Institution of Civil Engineers* 63.1 (Mar. 1977), pp. 49–67. ISSN: 1753-7789. DOI: [10.1680/iicep.1977.3293](https://doi.org/10.1680/iicep.1977.3293).
- [6] S. Phukan et al. “Application of drag reducing commercial and purified guar-gum for reduction of energy requirement of sprinkler irrigation and percolation rate of the soil”. In: *Agricultural Water Management* 47.2 (Mar. 2001), pp. 101–118. ISSN: 03783774. DOI: [10.1016/S0378-3774\(00\)00103-7](https://doi.org/10.1016/S0378-3774(00)00103-7).
- [7] R.C.R Figueredo and E Sabadini. “Firefighting foam stability: the effect of the drag reducer poly(ethylene) oxide”. In: *Colloids and Surfaces A: Physicochemical and Engineering Aspects* 215.1 (Mar. 2003), pp. 77–86. ISSN: 09277757. DOI: [10.1016/S0927-7757\(02\)00425-9](https://doi.org/10.1016/S0927-7757(02)00425-9).
- [8] Howard L. Greene, Richard F. Nokes, and Lindon C. Thomas. “Biomedical Implications of Drag Reducing Agents”. In: *Biorheology* 7.4 (June 1, 1971), pp. 221–223. ISSN: 18785034, 0006355X. DOI: [10.3233/BIR-1971-7404](https://doi.org/10.3233/BIR-1971-7404).
- [9] Guanjie Li et al. “Effect of drag-reducing polymer on blood flow in microchannels”. In: *Colloids and Surfaces B: Biointerfaces* 209 (Jan. 2022), p. 112212. ISSN: 09277765. DOI: [10.1016/j.colsurfb.2021.112212](https://doi.org/10.1016/j.colsurfb.2021.112212).
- [10] Vance Bergeron et al. “Controlling droplet deposition with polymer additives”. In: *Nature* 405.6788 (June 2000), pp. 772–775. ISSN: 0028-0836, 1476-4687. DOI: [10.1038/35015525](https://doi.org/10.1038/35015525).
- [11] Emilia Hilz and Arnoldus W.P. Vermeer. “Spray drift review: The extent to which a formulation can contribute to spray drift reduction”. In: *Crop Protection* 44 (2013), pp. 75–83. ISSN: 0261-2194. DOI: <https://doi.org/10.1016/j.cropro.2012.10.020>.

- [12] Gilliom, R.J. et al. *Pesticides in the Nation's Streams and Ground Water, 1992–2001*. The Quality of Our Nation's Waters. Series: Circular. U.S. Geological Survey Circular 1291, 2006.
- [13] Jorge Fernandez-Cornejo et al. "Pesticide Use in U.S. Agriculture: 21 Selected Crops, 1960-2008". In: *SSRN Electronic Journal* (2014). ISSN: 1556-5068. DOI: [10.2139/ssrn.2502986](https://doi.org/10.2139/ssrn.2502986).
- [14] Ming-Hsin Wei et al. "Megasupramolecules for safer, cleaner fuel by end association of long telechelic polymers". In: *Science* 350.6256 (Oct. 2, 2015), pp. 72–75. ISSN: 0036-8075, 1095-9203. DOI: [10.1126/science.aab0642](https://doi.org/10.1126/science.aab0642).
- [15] Vivian Powers. *American Chemical Society National Historic Chemical Landmarks. Bakelite: The World's First Synthetic Plastic*. Nov. 9, 1993.
- [16] Fred Trouton. "On the coefficient of viscous traction and its relation to that of viscosity". In: *Proceedings of the Royal Society of London. Series A, Containing Papers of a Mathematical and Physical Character* 77.519 (May 14, 1906), pp. 426–440. ISSN: 0950-1207, 2053-9150. DOI: [10.1098/rspa.1906.0038](https://doi.org/10.1098/rspa.1906.0038).
- [17] Jelena Dinic, Carina D. V. Martínez Narváez, and Vivek Sharma. "Rheology of Unentangled Polymer Solutions Depends on Three Macromolecular Properties: Flexibility, Extensibility, and Segmental Dissymmetry". In: *Macromolecular Engineering*. Ed. by Nikos Hadjichristidis et al. 1st ed. Wiley, Mar. 4, 2022, pp. 1–36. ISBN: 978-3-527-34455-0 978-3-527-81556-2. DOI: [10.1002/9783527815562.mme0067](https://doi.org/10.1002/9783527815562.mme0067).
- [18] Jelena Dinic et al. "Extensional Relaxation Times of Dilute, Aqueous Polymer Solutions". In: *ACS Macro Letters* 4.7 (July 21, 2015), pp. 804–808. ISSN: 2161-1653, 2161-1653. DOI: [10.1021/acsmacrolett.5b00393](https://doi.org/10.1021/acsmacrolett.5b00393).
- [19] Li Xi. "Turbulent drag reduction by polymer additives: Fundamentals and recent advances". In: *Physics of Fluids* 31.12 (Dec. 1, 2019), p. 121302. ISSN: 1070-6631, 1089-7666. DOI: [10.1063/1.5129619](https://doi.org/10.1063/1.5129619).
- [20] Christopher M. White and M Godfrey Mungal. "Mechanics and Prediction of Turbulent Drag Reduction with Polymer Additives". In: *Annual Review of Fluid Mechanics* 40.1 (Jan. 2008), pp. 235–256. ISSN: 0066-4189, 1545-4479. DOI: [10.1146/annurev.fluid.40.111406.102156](https://doi.org/10.1146/annurev.fluid.40.111406.102156).
- [21] Zeeshan Saeed and Brian R. Elbing. "Polymer drag reduction: A review through the lens of coherent structures in wall-bounded turbulent flows". In: *Physics of Fluids* 35.8 (Aug. 1, 2023), p. 081304. ISSN: 1070-6631, 1089-7666. DOI: [10.1063/5.0162648](https://doi.org/10.1063/5.0162648).
- [22] Saleh S. Baakeem et al. "Drag Reduction by Polymer Additives: State-of-the-Art Advancements in Experimental and Numerical Approaches". In: *Industrial & Engineering Chemistry Research* 63.17 (May 1, 2024), pp. 7485–7506. ISSN: 0888-5885, 1520-5045. DOI: [10.1021/acs.iecr.4c00202](https://doi.org/10.1021/acs.iecr.4c00202).

- [23] Theodore von Karman. “Mechanical similitude and turbulence”. In: 1931.
- [24] Kyoungyoun Kim et al. “Effects of polymer stresses on eddy structures in drag-reduced turbulent channel flow”. In: *Journal of Fluid Mechanics* 584 (Aug. 10, 2007), pp. 281–299. ISSN: 0022-1120, 1469-7645. DOI: [10.1017/S0022112007006611](https://doi.org/10.1017/S0022112007006611).
- [25] J L Lumley. “Drag Reduction by Additives”. In: *Annual Review of Fluid Mechanics* 1.1 (Jan. 1969), pp. 367–384. ISSN: 0066-4189, 1545-4479. DOI: [10.1146/annurev.fl.01.010169.002055](https://doi.org/10.1146/annurev.fl.01.010169.002055).
- [26] M Tabor and P. G. De Gennes. “A Cascade Theory of Drag Reduction”. In: *Europhysics Letters (EPL)* 2.7 (Oct. 1, 1986), pp. 519–522. ISSN: 0295-5075, 1286-4854. DOI: [10.1209/0295-5075/2/7/005](https://doi.org/10.1209/0295-5075/2/7/005).
- [27] Mohamed AbdElKader et al. “Development of Drag-reduced Turbulent boundary layers on smooth walls with different polymer concentrations”. In: 12th International Symposium on Turbulence and Shear Flow Phenomena (TSFP12). July 19, 2022.
- [28] I. Zadrazil et al. “Shear layers in the turbulent pipe flow of drag reducing polymer solutions”. In: *Chemical Engineering Science* 72 (Apr. 2012), pp. 142–154. ISSN: 00092509. DOI: [10.1016/j.ces.2011.12.044](https://doi.org/10.1016/j.ces.2011.12.044).
- [29] Sadek Shaban et al. “Investigation of near-wall turbulence in relation to polymer rheology”. In: *Physics of Fluids* 30.12 (Dec. 2018), p. 125111. ISSN: 1070-6631, 1089-7666. DOI: [10.1063/1.5062156](https://doi.org/10.1063/1.5062156).
- [30] Bayode E. Owolabi, David J. C. Dennis, and Robert J. Poole. “Turbulent drag reduction by polymer additives in parallel-shear flows”. In: *Journal of Fluid Mechanics* 827 (Sept. 25, 2017), R4. ISSN: 0022-1120, 1469-7645. DOI: [10.1017/jfm.2017.544](https://doi.org/10.1017/jfm.2017.544).
- [31] S. A. Vanapalli, S. L. Ceccio, and M. J. Solomon. “Universal scaling for polymer chain scission in turbulence”. In: *Proceedings of the National Academy of Sciences* 103.45 (Nov. 7, 2006), pp. 16660–16665. ISSN: 0027-8424, 1091-6490. DOI: [10.1073/pnas.0607933103](https://doi.org/10.1073/pnas.0607933103).
- [32] Edson J. Soares. “Review of mechanical degradation and de-aggregation of drag reducing polymers in turbulent flows”. In: *Journal of Non-Newtonian Fluid Mechanics* 276 (Feb. 2020), p. 104225. ISSN: 03770257. DOI: [10.1016/j.jnnfm.2019.104225](https://doi.org/10.1016/j.jnnfm.2019.104225).
- [33] R. W. Paterson and F. H. Abernathy. “Turbulent flow drag reduction and degradation with dilute polymer solutions”. In: *Journal of Fluid Mechanics* 43.4 (1970), pp. 689–710. DOI: [10.1017/S0022112070002677](https://doi.org/10.1017/S0022112070002677).
- [34] Lukas Brandfellner et al. “Quantitative description of polymer drag reduction: Effect of polyacrylamide molecular weight distributions”. In: *Journal of Non-Newtonian Fluid Mechanics* 325 (Mar. 2024), p. 105185. ISSN: 03770257. DOI: [10.1016/j.jnnfm.2024.105185](https://doi.org/10.1016/j.jnnfm.2024.105185).

- [35] Yves Ducharme and James D. Wuest. “Use of hydrogen bonds to control molecular aggregation. Extensive, self-complementary arrays of donors and acceptors”. In: *The Journal of Organic Chemistry* 53.24 (Nov. 1988), pp. 5787–5789. ISSN: 0022-3263, 1520-6904. DOI: [10.1021/jo000259a037](https://doi.org/10.1021/jo000259a037).
- [36] Shengyi Dong et al. “Supramolecular Polymers Constructed from Macrocyclic-Based Host–Guest Molecular Recognition Motifs”. In: *Accounts of Chemical Research* 47.7 (July 15, 2014), pp. 1982–1994. ISSN: 0001-4842, 1520-4898. DOI: [10.1021/ar5000456](https://doi.org/10.1021/ar5000456).
- [37] Jean-Marie Lehn. “Perspectives in Supramolecular Chemistry—From Molecular Recognition towards Molecular Information Processing and Self-Organization”. In: *Angewandte Chemie International Edition in English* 29.11 (Nov. 1990), pp. 1304–1319. ISSN: 0570-0833. DOI: [10.1002/anie.199013041](https://doi.org/10.1002/anie.199013041).
- [38] Liulin Yang et al. “Supramolecular Polymers: Historical Development, Preparation, Characterization, and Functions”. In: *Chemical Reviews* 115.15 (Aug. 12, 2015), pp. 7196–7239. ISSN: 0009-2665, 1520-6890. DOI: [10.1021/cr500633b](https://doi.org/10.1021/cr500633b).
- [39] Takuzo Aida and E.W. Meijer. “Supramolecular Polymers – we’ve Come Full Circle”. In: *Israel Journal of Chemistry* 60.1 (Jan. 2020), pp. 33–47. ISSN: 0021-2148, 1869-5868. DOI: [10.1002/ijch.201900165](https://doi.org/10.1002/ijch.201900165).
- [40] Philippe Cordier et al. “Self-healing and thermoreversible rubber from supramolecular assembly”. In: *Nature* 451.7181 (Feb. 2008), pp. 977–980. ISSN: 0028-0836, 1476-4687. DOI: [10.1038/nature06669](https://doi.org/10.1038/nature06669).
- [41] Hojin Kim. “New Long End-Associative Polymers for Mist Control in I. Aqueous Solutions and II. Hydrocarbon Solvents”. Medium: PDF Version Number: Final. PhD thesis. California Institute of Technology, Aug. 26, 2022. DOI: [10.7907/R SX9-QT39](https://doi.org/10.7907/R SX9-QT39).
- [42] Jelena Dinic, Leidy Nallely Jimenez, and Vivek Sharma. “Pinch-off dynamics and dripping-onto-substrate (DoS) rheometry of complex fluids”. In: *Lab on a Chip* 17.3 (2017), pp. 460–473. ISSN: 1473-0197, 1473-0189. DOI: [10.1039/C6LC01155A](https://doi.org/10.1039/C6LC01155A).
- [43] Robert Learsch. “Droplet control in aqueous and hydrocarbon fluids: Long, end-associative polymers dictate fluid behavior under elongational flows”. PhD thesis. Caltech, Oct. 20, 2022.

*Chapter 2***AQUEOUS TERPYRIDINE-ENDED POLYACRYLAMIDE
INSTABILITY CHARACTERIZATION AND MITIGATION****2.1 Introduction****2.1.1 Competing (in)stability requirements for flow additives**

Long-chain linear polymers are useful agricultural, aviation, and industrial flow-control additives (at a concentration typically $< 0.1\%$ by weight) due to their ability to increase a fluid's extensional viscosity (over 10-fold) while modestly increasing shear viscosity (less than double) [1]. They can be effective in applications such as droplet control, mist suppression, and drag reduction, but are limited by the vulnerability of such long polymers to flow-induced degradation. Agricultural applications impose contradictory requirements, as additives must resist mechanical and chemical degradation long enough to maintain effectiveness throughout their usage, but eventually, they must breakdown in a way that ensures environmental safety and sustainably. Linearly associative, terpyridine-ended polyacrylamide (TPAM) has been proposed primarily to combat the ubiquitous challenge of mechanical chain scission under high elongational stresses due to pumps, filters, contractions, and turbulence. However, the competing requirements of chemical stability until applied to crops and environmental breakdown has not yet been examined. The suitability, structure, and potential degradation pathways are discussed in Sections 2.1.2, 2.1.3, and 2.1.4, respectively. Then, the equilibration and stability of TPAM megasupramolecules is examined through systemic experimentation, both chemical and rheological. This leads to methods to extend TPAM's shelf life by several weeks—limiting air exposure, avoiding an excess of metal ions relative to ligands, and storing samples in refrigerated conditions (4°C)—while retaining structures that ensure degradation in

soil.

2.1.2 Suitability of TPAM for environmental application

The fundamental components of megasupramolecular TPAM—polyacrylamide, terpyridine ligands, and metal ions—along with our selection of a trithiocarbonate moiety in the backbone and esters for linking terpyridine to polyacrylamide, are considered environmentally sound chemical choices. The long-standing use of polyacrylamide (PAM) in irrigation and waste water treatment has established that it can be broken down and utilized by microorganisms found in the environment [2, 3]. It has been proposed that terpyridine can be used in waste water treatment as well and have potentially therapeutic biological impacts [4, 5]. Metal ions such as Ni(II), Fe(II), or Co(II) are commonly found in the environment and are essential to biological functions, but caution should still be taken when applying them in engineered systems, as adverse effects may occur when exposed to high concentrations [6]. Namely, The Environmental Protection Agency recommends a range of safe nickel levels for different circumstances, 72 ppm in soil and 0.2 ppm in waste water, while the World Health Organization recommends a far stricter 0.05 ppm limit for agricultural settings [7]. When exploring the efficacy of our TPAM in agricultural and aqueous applications, we limit our concentration levels such that nickel usage is below the strictest conditions (< 0.05 ppm). For decades, ester's biodegradability has been widely accepted, which has recently been revisited and experimentally validated [8, 9]. The environmental effects of trithiocarbonate are less studied and understood, but existing literature is promising. One study shows polymers with trithiocarbonatate end groups are nontoxic even at relatively high concentrations (1 mM) [10]. Another study shows trithiocarbonate could be used in waste water treatment to remove toxic chemicals in the environment [11].

The Kornfield group has designed TPAM so that it can degrade safely, but we must

also characterize the necessary storage conditions to maintain their efficacy until their application is complete.

2.1.3 TPAM chemical synthesis and structure

A complete description of TPAM synthesis is detailed in Dr. Hojin Kim's Thesis Chapter 2, "Water-soluble long linear supramolecular polymers based on metal-ligand coordination with terpyridine functionalized polyacrylamide" [12]. Dr. Kim built on the work of Cameron and coworkers, who to our knowledge, were the first to synthesize bis-terpyridine-ended polyacrylamide via two-step RAFT polymerization [13]. Cameron's unimers spanned $M_n = 455\text{-}570$ kg/mol with a polydispersity index ($\text{PDI} = M_w/M_n$) of 1.53-2.55, reaching megasupramolecular weights of 2000 kDa. Dr. Kim optimized their methods developing a one-step RAFT polymerization technique, narrowing the PDI to < 1.1 , and expanding the range of unimers to 92-3000 kDa. Building upon previous work on long, end-associative, hydrocarbon-soluble polymers in the Kornfield group, Dr. Kim hypothesized that longer chains would suppress the formation of rings and enhance the end-associative polymers' efficacy at low concentrations in engineering applications. He also noted that the unimer chains should be short enough to resist mechanical scission, so most of his TPAM characterization was performed on 800 kDa polymers. He demonstrated the successful formation of megasupramolecular coordination polymers (> 2000 kg/mol) at low concentrations (< 0.2 wt %) and that these TPAMs could recover their ultralong molecular weight after shearing through a pump.

In this chapter, we build on Dr. Kim's work by examining the chemical stability of our TPAM. In later chapters, we explore ways to vary TPAM's megasupramolecular topology and test its ability to reduce drag and resist chain scission.

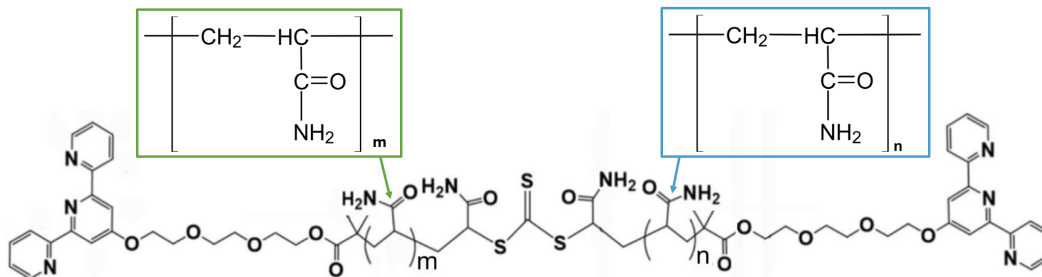


Figure 2.1: Chemical structure of terpyridine-ended polyacrylamide (TPAM). The trithiocarbonate is near the center ($m \approx n$), with PAM on either side, connected to terpyridine via ester linkages.

2.1.4 Potential degradation pathways

In this chapter, using measurements of the molecular weight distribution following selected degradation conditions, we discriminate among the following degradation pathways.

Metal ions and oxygen: Potential untimely degradation pathways can occur with metal ions acting as catalysts, particularly in the presence of oxygen. The resulting formation of free radicals can degrade the polymer into fragments [14]. In addition, certain divalent metal ions can oxidize into trivalent cations [15], which would prohibit the formation of the bis-terpy complex linkages connecting the TPAMs. In either case, the TPAMs would no longer be able to connect with each other and form long chains. To limit the potential for oxidative effects, we focus our study primarily on a more stable divalent metal ion, Ni(II) [16].

Trithiocarbonate in backbone: It has been posited that one of the greatest weaknesses of the TPAM structure is the trithiocarbonate at the center of the backbone (Figure 2.1) [12, 13]. The amide (PAM side groups) can generate free ammonia via hydrolysis with hydroxide (OH^-) when the solution pH is greater than 7 [17, 12]. Ammonia can degrade the trithiocarbonate, the central linkage of the backbone, via aminolysis. Dr. Kim mitigated this possibility by maintaining a pH below 7 during synthesis [12]. Others have speculated that these reactions were deteriorating their

system without any direct evidence for or against this claim [13].

Ester hydrolysis: Esters are suitable for environmental applications because they are relatively easy to breakdown via hydrolysis. However, their breakdown must be prevented prior to use. Hydrolysis can occur in a neutral solution at very slow rates, but as soon as a solution becomes acidic or basic, H⁺ or OH⁻ ions may catalyze hydrolysis and significantly speed up ester cleavage, which would create a "dead end" when a chain end has lost its terpyridine group.

2.1.5 Preliminary study reveals TPAM λ_E decay over time

A substantial temporal decay of TPAM's λ_E was identified by Dr. Rob Learsch during his preliminary investigation into TPAM extensional behavior (Figure 2.3). This decay is an issue for two distinct reasons. From a scientific research standpoint, we need reasonably stable solutions to reliably study the megasupramolecular topology and performance. From a practical flow additive standpoint, TPAM's λ_E decay indicates that the TPAM solutions and protocols must be improved to provide adequate shelf-life. In practice, agrochemicals such as pesticides have a typical shelf life of around two years, but they may also come with strict storage requirements such as limiting exposure to air or requiring refrigeration. In the current chapter, we characterize and mitigate TPAM's λ_E decay to provide scientifically sound guidance on storage requirements to meet industry expectations for shelf stability. In doing so, we also enable further scientific exploration on the tunability of TPAM's extensional behavior and potential in agricultural and drag reduction applications.

2.1.6 Anticipation of a rise in λ_E on shorter timescales

We hypothesize that, in a dilute solution ($c < c^*$), the megasupramolecules formed by mixing TPAM with metal ions would not reach their highest molecular weight (M_w) or λ_E instantaneously. When a Ni(II) complexes a single terpyridine, there is a strong driving force for it to add a second terpyridine. This is due to the

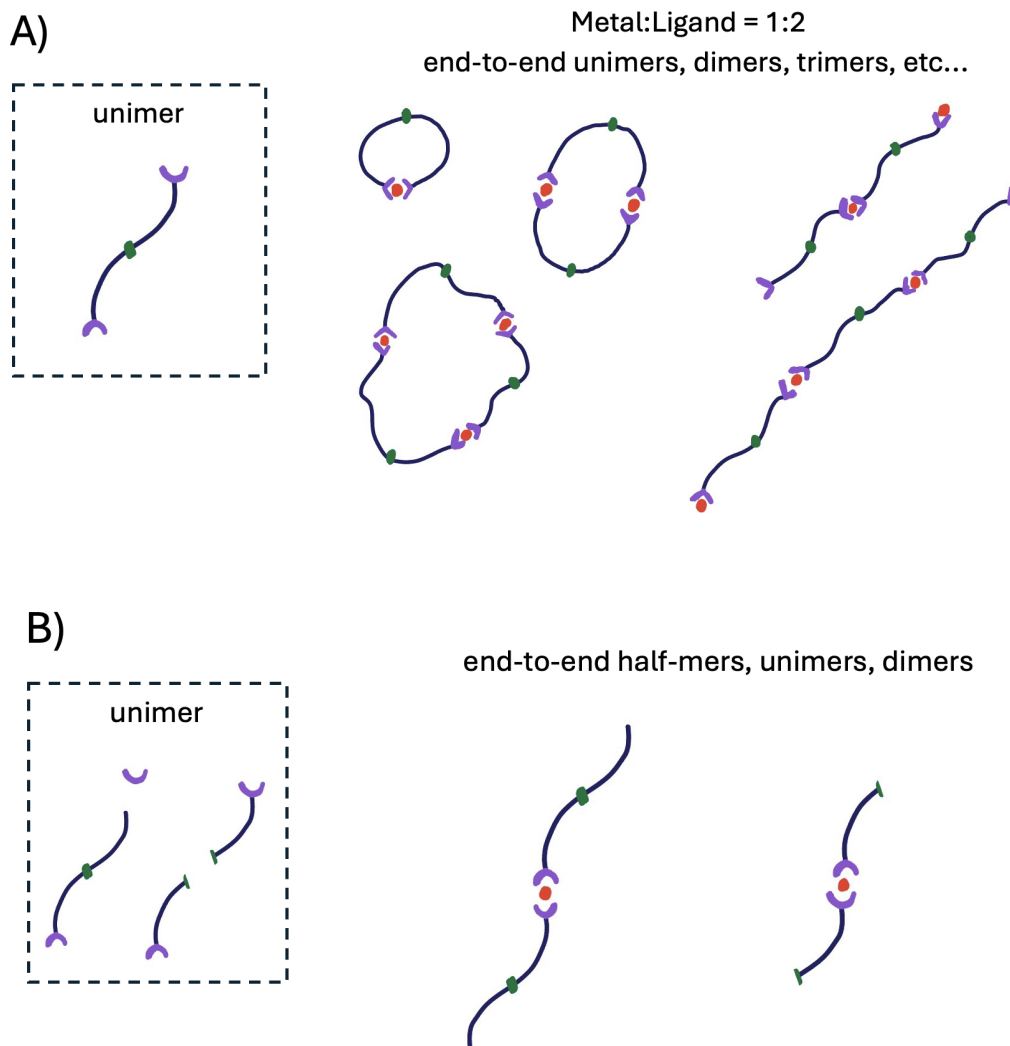


Figure 2.2: Sketch of (A) fully intact unimers and a few illustrative end-to-end supramolecules, and (B) putative structures of degraded unimers and their stunted end-to-end supramolecules. Terpyridines are represented by purple crescents; metal ions by red dots; flexible polyacrylamide by black curves; and trithiocarbonates by green dots. (A) Degradation of molecules at the ester linkage that attaches terpyridine to the chain ends or at the trithiocarbonate are shown as left/right pairs of sketches for both unimers and supramolecules. Note that an actual solution would likely consist of a mixture of both fully intact unimers and degraded unimers.

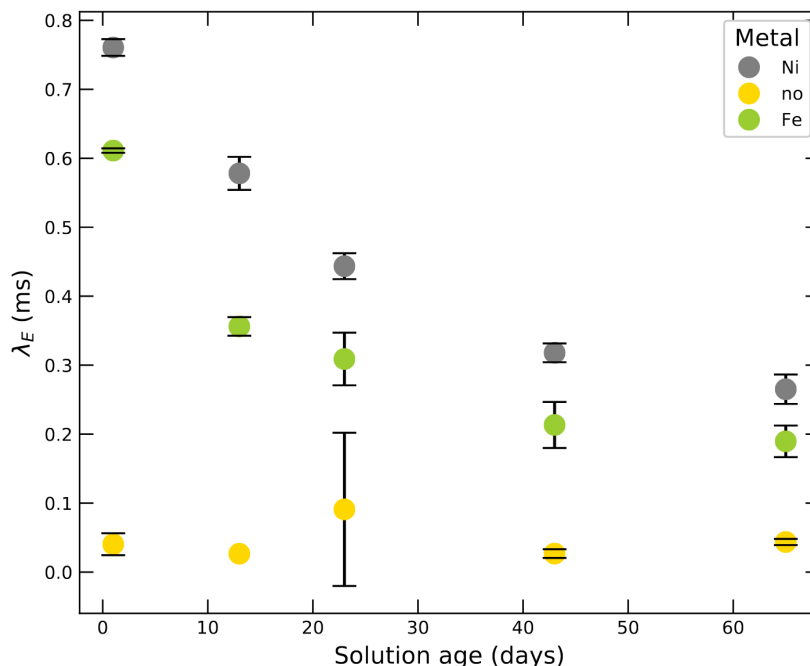


Figure 2.3: Preliminary evidence of TPAM's λ_E decay on a timescale of several days, originally published by Learsch in his thesis Chapter 5 "Elongational properties of end associative polyacrylamide solutions" [18]. His solutions contained 0.8 MDa TPAM unimers dissolved at 0.04 wt% in Bio Pure water comparing the addition of NiCl_2 (grey) and FeCl_2 (green) at a metal:ligand ratio = 2:1 to no metal (yellow).

fact a bis-terpy complex has lower free energy than a mono-terpy complex with Ni(II) (described in more detail in Chapter 3). In a dilute solution, the nearest terpyridine is the one at the opposite end of the unimer. Therefore, unimer rings are kinetically favored. Over time, as the TPAM unimers begin to make contact with other unimers, they can form dimers, trimers, and beyond (Figure 2.4). These larger megasupramolecular structures would elicit a higher λ_E compared to a unimer ring. This evolution from kinetically favored structures (on a timescale of minutes to hours) to entropically favored structures (on a timescale of hours to days) would result in a short term rise in λ_E before the decay is observed, but this short-term rise has not been directly studied before the results presented in Section 2.2.

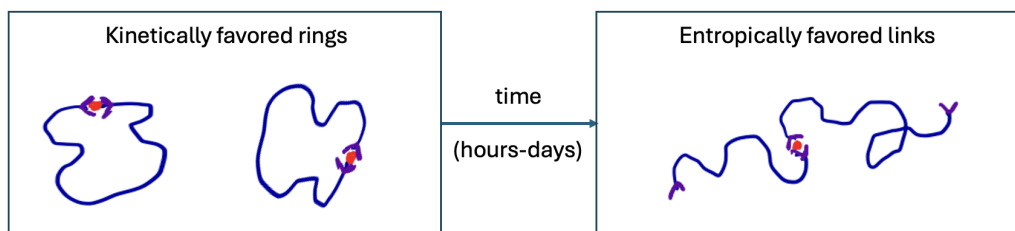


Figure 2.4: Schematic illustrations of the initial bias in chain configurations that results when metal is added to a dilute solution of unimers ($c < c^*_{unimer}$). The left figure illustrates that once a metal forms a complex with one terpyridine, the second terpyridine it encounters is the one at the opposite end of the same chain to which it is attached. Over time, they exchange partners and form an equilibrium distribution of supramolecules that contains linear and cyclic multimers which have greater conformational entropy than a unimer ring (see the right figure, which illustrates a di-mer link, one of the potential linear conformations within a distribution).

2.1.7 Scope of current work

This chapter addresses TPAM's λ_E initial rise and eventual decay by characterizing potential chemical degradation pathways and mitigating their effects, providing the foundation for exploring TPAM topology and understanding its impact on flow behavior (Chapters 3, 4, and 5).

2.2 Initial rise in λ_E

Prior experiments testing for possible degradation examined λ_E of TPAM solutions with time intervals of weeks starting with a "time zero" within the first 24 hours after the addition of metal ions 2.3) [18]. In the present experiments, times as short as a few hours are included, leading to the discovery that λ_E initially *increases* (Figure 2.5), as anticipated by our reasoning in Figure 2.4. Some of the variables examined in this chapter in relation to degradation also interplay with the equilibration kinetics, rate, and maximum of the λ_E rise. For example, a higher temperature (40°C) causes a quicker rise in λ_E , relative to room temperature (22°C), which is faster than in a refrigerator (4°C). We will see later in this chapter how varying temperature also affects the λ_E decrease.

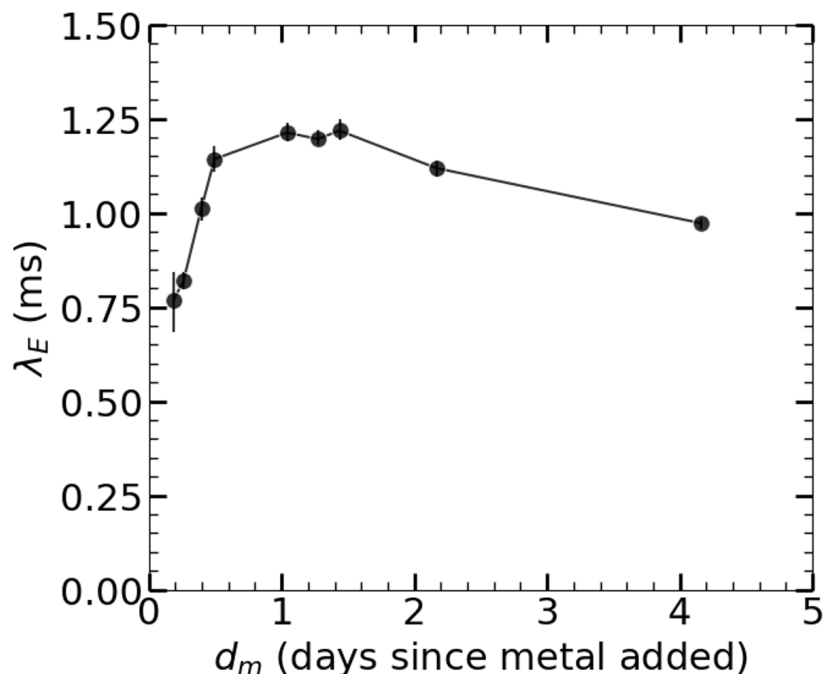


Figure 2.5: First observation of a short-term rise in λ_E with a maximum around 1 day since metal added, defined d_m . Error bars are shown for $n \geq 3$ DoSER runs on the same TPAM solution sample.

$M_{uni} = 0.84$ MDa; Solvent = unbuffered MilliQ; $c = 0.04$ wt%; M:L = 0.5; Dilute \rightarrow Metal; $T_{store} = 22^\circ\text{C}$; Vial container.

2.3 Trithiocarbonate breakage through aminolysis

To characterize degradation pathways, I explored the hypothesis of Lewis et al. (2019) that trithiocarbonate aminolysis is responsible [13]. Given the critical role of ammonia, I test the plausibility in the present TPAM solutions by adding ammonia directly to the solution, rather than waiting for side groups hydrolysis of unknown kinetics leading to an unknown concentration of ammonia. The amount of ammonia added can be compared to the number of trithiocarbonates present and to the number of NH_2 available from the side groups.

A solution of 0.04wt% 0.8 MDa TPAM contains $0.5\mu\text{M}$ unimers. I first add $20\mu\text{M}$ of ammonia, or 40 times the number of TPAM, and thus 40 times the number of trithiocarbonates in solution. Considering there are around 10^4 monomers that makeup one unimer of TPAM and one NH_2 per side group, this amount of NH_3

corresponds to approximately 0.4% of the side groups. The unimer molecular weight is monitored with a GPC after 5 hours, 1 day, and 12.5 days in the presence of $20\mu\text{M}$ ammonia (Figure 2.6). There is no change in the backbone structure. Note that the pH of this solution remained weakly acidic (measured at pH 6), whereas without ammonia the pH is also around this level (pH 5.6 to 6.8 is typical for un-buffered MilliQ water exposed to carbon dioxide in air).

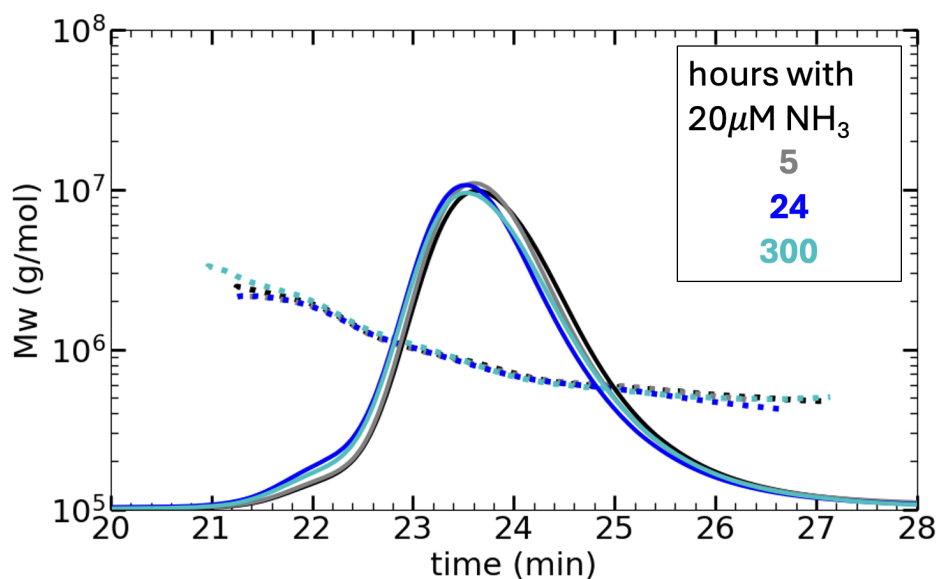


Figure 2.6: Evolution of GPC traces for $0.5\mu\text{M}$ TPAM mixed with $20\mu\text{M}$ ammonia. No change in M_w or degradation of the trithiocarbonate is observed over 12 days. The unimer ($M_n = 0.84\text{ Mg/mol}$) with no ammonia is shown in black. No change in M_w or degradation of the trithiocarbonate is observed over 12 days. The solution's pH measured 6, indicating no significant increase relative to the weakly acidic MilliQ water pH.

Next, I inundate the system with ammonia, adding around 100 mM. This is equivalent to 200,000 ammonia for every trithiocarbonate in solution, which is also equivalent to 2000 times the number of possible ammonia created if all the side groups were converted to free amines and then ammonia. GPC results (Figure 2.7) indicate that within 1 hour, trithiocarbonates begin to break, and within 12 hours, the majority have broken leaving the polymers in solution with a M_w near 0.4 kDa (Figure 2.8). The solutions pH measured 11, indicating a significant increase to the weakly acidic

MilliQ water pH.

The amount of ammonia used to initiate this degradation far exceeds what is chemically plausible in the real system, but the goal here was to see how fast the trithiocarbonate breaks in this hypothetical case, and crucially, obtain the molecular weight distribution for this case so that it can be compared to more subtle degradation cases in future sections.

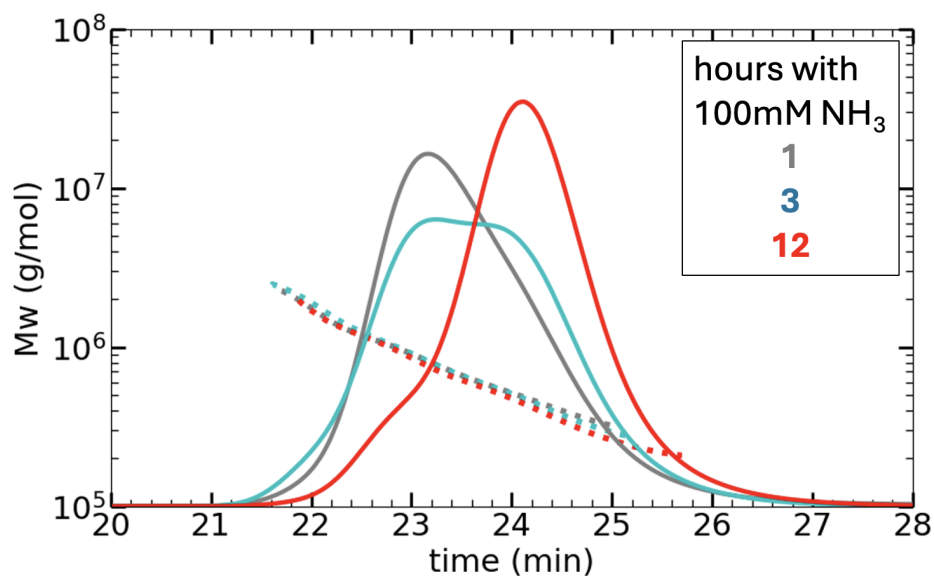


Figure 2.7: Evolution of GPC traces for $0.5 \mu\text{M}$ TPAM mixed with 100mM ammonia at pH 11. Within 12 hours, the trithiocarbonates have broken.

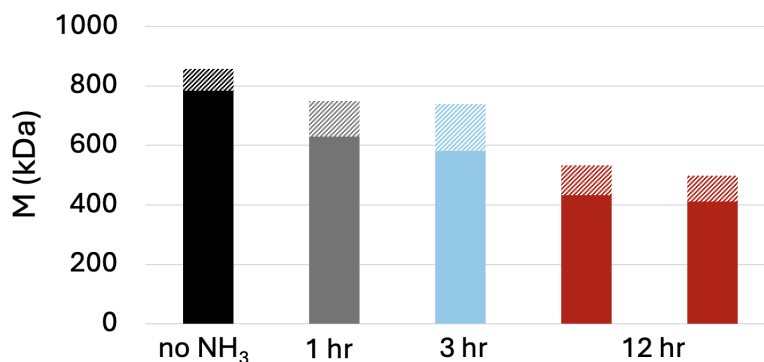


Figure 2.8: Evolution of M_n (solid bars) and M_w (hatched bars) for $0.5 \mu\text{M}$ TPAM mixed with 100mM ammonia, corresponding to the GPC traces in Figure 2.7.

2.4 λ_E decay correlates to the presence of metal ions and exposure to air

Literature suggests two other possible degradation pathways for TPAM: hydrolysis of the ester due to water and PAM backbone breakage due to metal ion-generated free radicals. The former has been suspected in prior TPAM research [13], although not directly investigated until the present work. Metal ion-induced degradation has been studied for polyacrylamide (PAM) [14], but to the best of our knowledge is not connected to TPAM specifically. The terpyridine end-groups of TPAM may alter metal ion-induced degradation, as the presence of ligands is known to modify metal ion catalysis [19].

2.4.1 Experimental protocol for distinguishing hydrolytic and ion-induced degradation

To differentiate between the effects of water alone versus the effects of metal ions on TPAM degradation, we developed a protocol that independently varies the time TPAM has been dissolved in water from the time it has been exposed to metal ions. First, the solid polymer is dissolved at 1 wt% (10,000 wppm) in two different solvents: 1) an acetic acid pH 5.6 buffer that is understood to exacerbate both ester hydrolysis and metal-mediated radical reactions, and 2) MilliQ water (with uncontrolled pH that is typically slightly below neutral pH 7 due to ambient CO₂ mixing with water). The solid TPAM is gently dissolved on a Wrist Action Shaker for three days until no particulates are observed in the solution. The TPAM solution is further diluted to 0.04 wt% (400 wppm) with the same solvent used to make the solution and rolled at 10 rpm overnight to ensure homogeneous mixing.

Nickel(II) Chloride (0.5 μ M, i.e., 1 Ni(II) ion per 2 terpyridine) is added to the TPAM solution on separate days to distinguish between the degradation in water alone vs when metal ions are present, as illustrated in Figures 2.9 and 2.10.

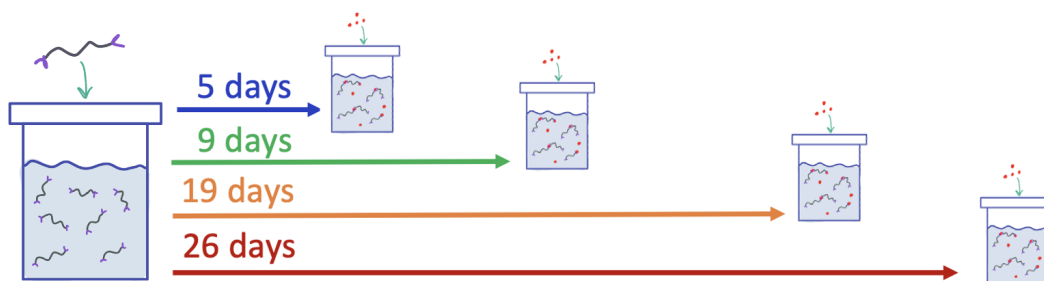


Figure 2.9: Acetic acid buffer solvent protocol illustrating when metal is added to the polymer solution relative to the day the polymer was dissolved. All solutions were dissolved on $d_p = 0$, and metal was added to the solutions on $d_p = 5, 9, 19,$ and 26 .

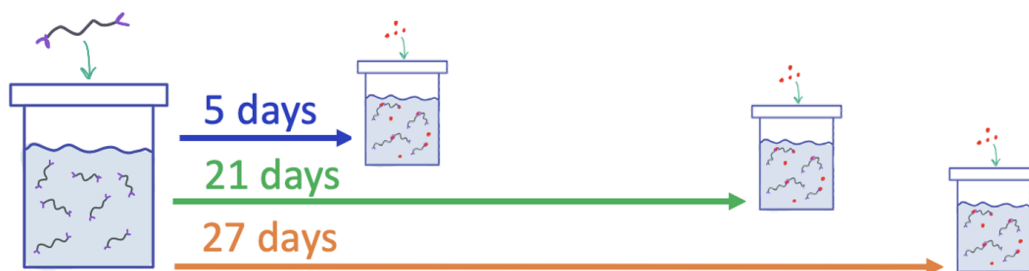


Figure 2.10: MilliQ (un-buffered) solvent protocol illustrating when metal is added to the polymer solution relative to the day the polymer was dissolved. All solutions were dissolved on $d_p = 0$, and metal was added to the solutions on $d_p = 5, 21,$ and 27 .

2.4.2 Results suggest a distinction between hydrolytic and ion-induced degradation and hint at the effect of air

For both the acetic acid buffer and MilliQ (unbuffered) solvents, results are offset when shown relative to the days since the polymer was dissolved (d_p), and overlap when plotted on the days since metal added (d_m) reference frame (Figures 2.11 and 2.12). This suggests that the presence of the metal ions, rather than merely the time in aqueous solution, correlates with the temporal decay of λ_E . However, for the acetic acid buffer, a drop off in the maximum λ_E occurs without metal present in the starting solution between days 9 and 19. This could be explained by the fact that ester hydrolysis speeds up under more acidic conditions. Without the acidic buffer

present in the solvent, there is no notable difference in the maximum achievable λ_E after being dissolved in un-buffered MilliQ water alone at the timescales observed. We emphasize though that the time metal was added also corresponded to increased air exposure. This effect is looked at more closely in the following section.

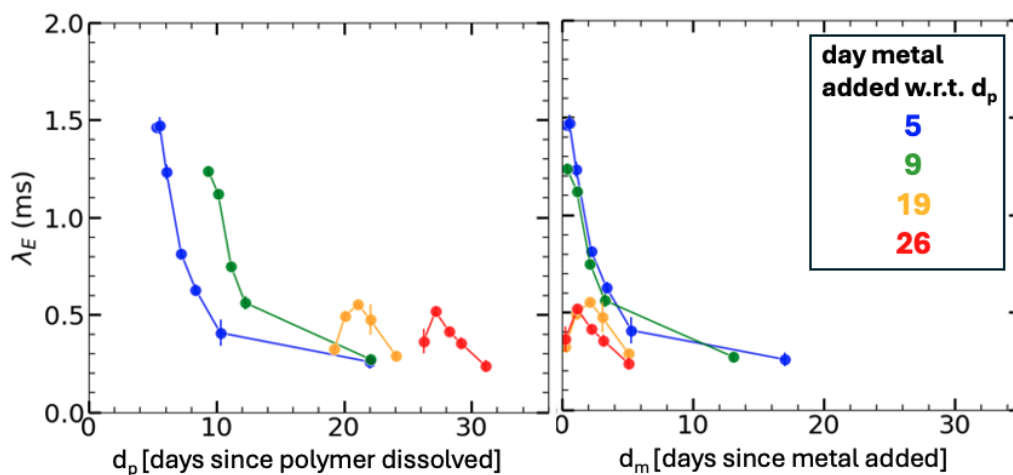


Figure 2.11: Comparison between λ_E decay relative to the day the polymer was dissolved in an acetic acid buffer vs the day the metal was added to solution. Error bars are shown for $n \geq 3$ DoSER runs on the same sample. $M_{uni} = 0.84$ MDa; Solvent = acetic acid buffer (pH 5.6); $c = 0.04$ wt%; M:L = 0.5; Dilute \rightarrow Metal; $T_{store} = 22^\circ\text{C}$; syringe container.

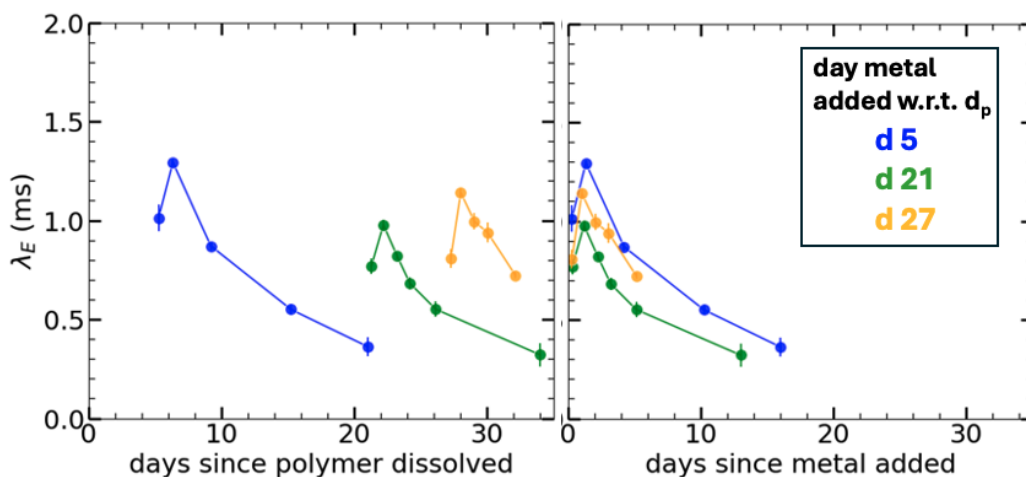


Figure 2.12: Comparison between λ_E decay relative to the day the polymer was dissolved in MilliQ water vs the day the metal was added to solution. $M_{uni} = 0.84$ MDa; Solvent = unbuffered MilliQ; $c = 0.04$ wt%; M:L = 0.5; Dilute \rightarrow Metal; $T_{store} = 22^\circ\text{C}$; syringe container.

2.5 Limiting exposure to air decreases the rate of decay of λ_E

To enable more conservative use of the TPAM solutions and greater efficiency of the experiments, I began storing solutions in the syringes used during DoSER. Varying the sample storage protocol by storing some solutions in a syringe with others stored in a plastic vial (2.13) led to a serendipitous clue on what factors exacerbate or hinder the decay of λ_E . For all solutions, I ran DoSER on each sample at $d_m = 0.25$ (6 hours after adding metal) and placed them back on the roller, mixing at 10 rpm for the first 24 hours within a vial. For the syringe case, I tested DoSER on $d_m = 1$, stored the solution in the syringe with a Luer Lock cap, and ran DoSER daily for four days. For the vial case, I tested DoSER on $d_m = 1$ and kept the solution in the vial unopened for at least four days.

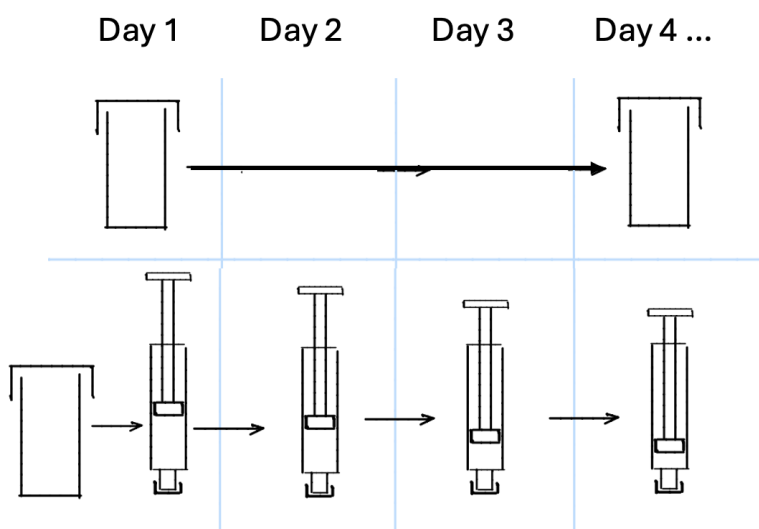


Figure 2.13: Illustration of the difference storage condition protocol related to the experiments shown in Figure 2.14. The top sketch represents a solution in a vial tested on days 1 and 4, left unopened in between tests. The bottom sketch is a solution stored in a syringe on day 1 and tested daily until day 4.

The TPAM solutions λ_E decayed faster when stored and regularly sampled in a syringe versus when stored and unopened in a vial (Figure 2.14). For the syringe case, λ_E drops by 40% within the first four days. For the vial case, λ_E is unchanged after four days. We suspect that in the syringe case, the repeated exposure to air for

sampling as well as the less tightly sealed container created a greater opportunity for oxygen to react with the system.

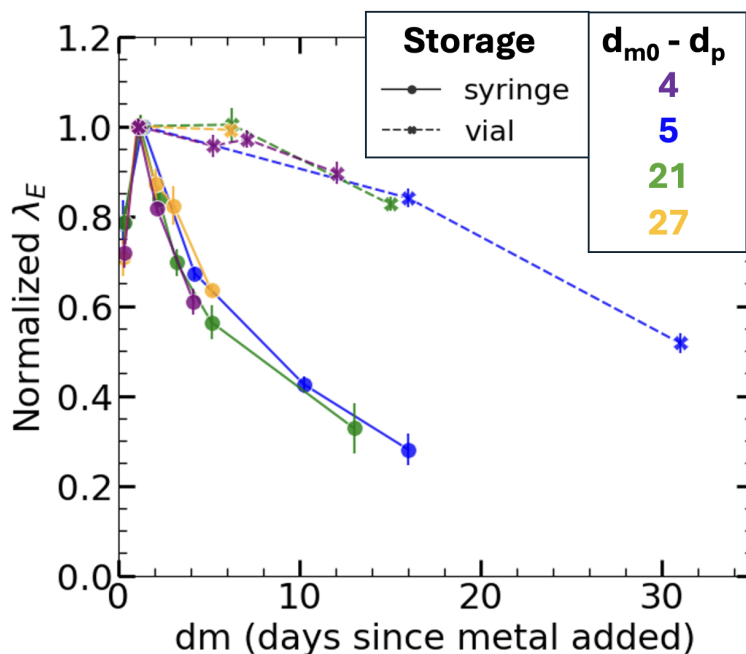


Figure 2.14: Comparison between λ_E decay when stored in a 20 mL plastic vial versus a 5 mL Luer lock syringe. Results are normalized based on the λ_E at $d_m = 1$ to highlight the repeatability of the different storage condition's influence on λ_E decay rates. Error bars are shown for $n \geq 3$ DoSER runs on the same sample. $M_{uni} = 0.84$ MDa; Solvent = unbuffered MilliQ; $c = 0.04$ wt%; M:L = 0.5; Dilute \rightarrow Metal; $T_{store} = 22^\circ\text{C}$.

At this point, we have differentiated between hydrolytic degradation due to water and metal-ion induced catalyzed decay, but we have also identified a clear influence of air exposure. To get a better sense of approximately where TPAM's weak point is along its molecule, we can turn to GPC to assess molecular weight distributions of minimally degraded, partially degraded, and heavily degraded TPAM. The GPC traces indicate that as the TPAM solutions degrade, the unimer backbones remain intact (Figure 2.15)¹. We see this by observing that the lower molecular weight

¹The GPC distributions were taken on syringe-filtered TPAM solutions. We learned later on in the study (Chapter 4) that the syringe filtration affects the distribution of the megasupramolecules. The main conclusion of this figure still remains (convergence towards unimer) as the unimer species are unaffected by filtration. Moving forward, TPAM solutions were not filtered before GPC unless otherwise specified.

peaks for all three cases are within the peak for the "no metal" unimer case, and their corresponding molecular weights overlap with the unimer's as well. None of them elute at a later time, which would indicate smaller molecules forming in the solutions, as we saw in Figure 2.7 through imposing aminolysis. This is further proof that the TPAM backbones are not degrading at the trithiocarbonate in the center, and also suggests that the metal ions are not causing a chain reaction of radical formation that break the PAM at random points along the backbone. Instead, what this points to is a decreased ability to associate and form longer chains through the ligand-metal-ligand complexes. The GPC is unable to resolve the size of smaller molecules that may provide deeper insight on the mechanism. For instance, if we could clearly identify the presence or absence of free floating 244 g/mol terpy, we could ascertain whether or not the ester links are breaking. However, we can still proceed with our effort to mitigate chemical degradation, which simultaneously serves as a clue towards the underlying mechanism.

2.6 Temperature dependence of λ_E decay

If the mechanism causing TPAM λ_E decay is a chemical reaction as we suspect, we hypothesize that we may be able to mitigate it and stabilize the TPAM by storing the solutions at colder temperatures (refrigerated at 4°C). On the contrary, we may speed it up by storing the solutions at warmer temperatures (incubated at 40°C). In this section, we first explore Arrhenius theory and activation energy as a tool for understanding the influence of temperature on the suspected degradation mechanisms. Then, we develop an experimental protocol to assess temperature effects on λ_E , and discuss how the results provide evidence towards a degradation mechanism and a solution for mitigation.

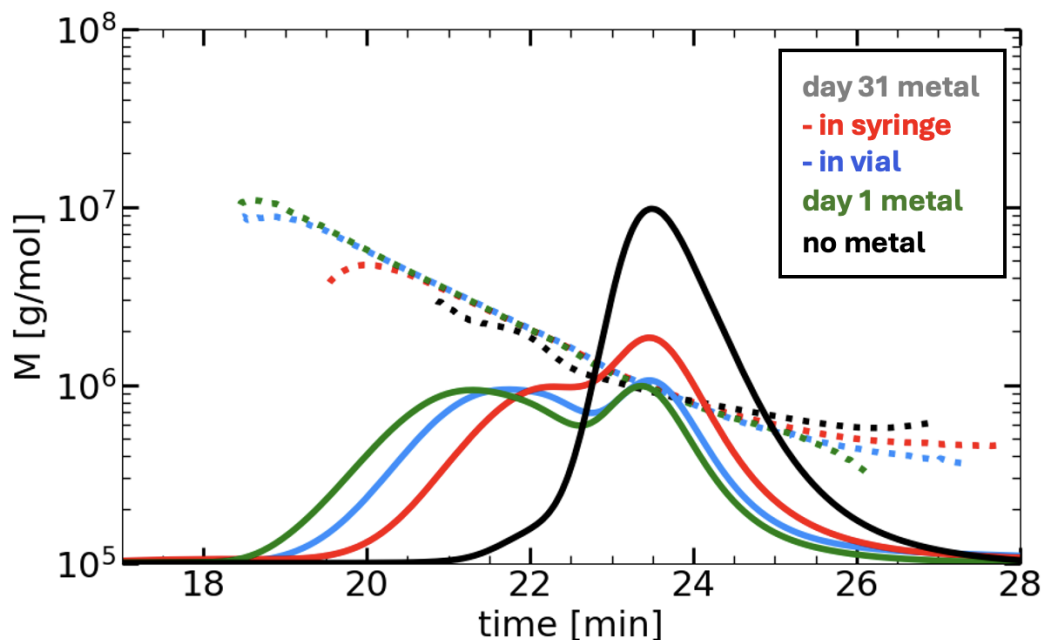


Figure 2.15: Molecular weight distributions for TPAM solutions stored in vial versus syringe, indicating an evolution towards the unimer peak. Shown here are: no metal (black), 1 day after metal added exhibiting minimal degradation (green), 31 days after metal added and stored in vial exhibiting intermediate degradation (blue), and 31 days after metal added and stored in syringe exhibiting significantly further degradation (red). $M_{uni} = 0.84$ MDa; Solvent = unbuffered MilliQ; $c = 0.04$ wt%; M:L = 0.5; Dilute \rightarrow Metal; $T_{store} = 22^\circ\text{C}$.

2.6.1 Activation energy can provide a clue towards a mechanism

Arrhenius theory can be used to investigate the plausible degradation mechanisms contributing to TPAM's λ_E decay. Different chemical reactions have different temperature dependencies. The activation energy, denoted E_A , is the minimum energy barrier that must be overcome for reactants to transform into products in a chemical reaction. The Arrhenius equation relates the rate constant k of a reaction to temperature T , as described in Equation 2.1, where R is the gas constant and A is the pre-exponential factor.

$$k = Ae^{\frac{-E_A}{RT}} \quad (2.1)$$

The first-order rate constant can be calculated based on the half-life, $t_{1/2}$, as shown in Equation 2.2.

$$k_1 = \frac{\ln(2)}{t_{1/2}} \quad (2.2)$$

Measurements of the half-life at different temperatures can be used alongside the Arrhenius equation to help determine the activation energy. By analyzing the activation energy and how the half-life changes with temperature, one can gain insights into the reaction mechanism. For instance, [20] identifies that acid-catalyzed hydrolysis of proyl formate in water gives an E_A of 63.5 ± 0.7 kJ mol⁻¹. They used 20mM HCl to induce the hydrolysis, which corresponds to pH 1.7. This is significantly stronger than our solutions (pH 5.6-6.8 for unbuffered MilliQ or pH 5.6 for the acetic acid buffer) but it can still be used as a benchmark for comparison to see if we are within a reasonable range for this to be a possible explanation of TPAM's degradation mechanism.

2.6.2 Experimental protocol to assess temperature effects on λ_E decay rate

The 0.8 MDa TPAM is first diluted to 0.04 wt% in un-buffered MilliQ solvent, and NiCl₂ added such that the metal:ligand ratio = 2:1. The solutions are rolled at 10 rpm at room temperature for 24 hours. λ_E is measured using DoSER one day after the metal was added ($d_m = 1$). After this first measurement, one sample is stored in an incubator at 40°C and another is stored in a refrigerator at 4°C and measured at regular intervals. This procedure is repeated with a different starting solution to assess the repeatability of the results under each storage conditions. TPAM λ_E decay (or lack thereof) that occurs at each of these conditions with metal ions present in solution are shared in Section 2.6.3. Additionally, similar to Section 2.4.1 where we look at the effects of water alone versus the presence of metal ions, TPAM starting solutions are stored in the incubator at 40°C with ions added later, and these results

are shared in Section 2.6.3.

2.6.3 Temperature effects provide evidence towards a mechanism and a solution for mitigation

TPAM exhibits different decay rates at various temperatures, indicating that the rate of the underlying reaction changes with temperature (Figure 2.16). At 22°C (room temperature), the decay rate is moderate, and proceeds as expected in the preceding sections. Increasing the storage temperature to 40°C, the decay rate increases, showing that the reaction at this higher temperature can occur much faster. Conversely, and fortunately for our priority of stabilizing the solution on a shelf, decreasing the storage temperature to 4°C slows down the decay rate significantly. This trend aligns with the principles of the Arrhenius equation, where higher temperatures typically lead to increased reaction rates due to more reactant molecules having the required activation energy.

It should be noted that the decay rates for λ_E stored at 40°C and 22°C show repeatable trends, while the decay rate for 4°C exhibits diverging behavior for the replicate runs. We speculate that this is due to air exposure occurring within the first round of solutions (marked with "x" symbols). Special care was taken to reduce the amount of times vials were exposed to air and left open during the sampling process for the second round of replicates (marked with "o" symbols), which completely stabilized the solutions over 41 days they were tracked. This result alone indicates that there are likely confounding factors contributing to a complex degradation mechanism influencing TPAM's λ_E decay. Considering this, a first order rate constant based on λ_E decay over time may be a highly simplistic approximation, but keeping this in mind, we proceed with the analysis.

TPAM stored at 22°C exhibits half lives of 25 and 33 days for each replicate, and the solutions stored at 40°C exhibit half lives of 5 and 6 days. We consider only one

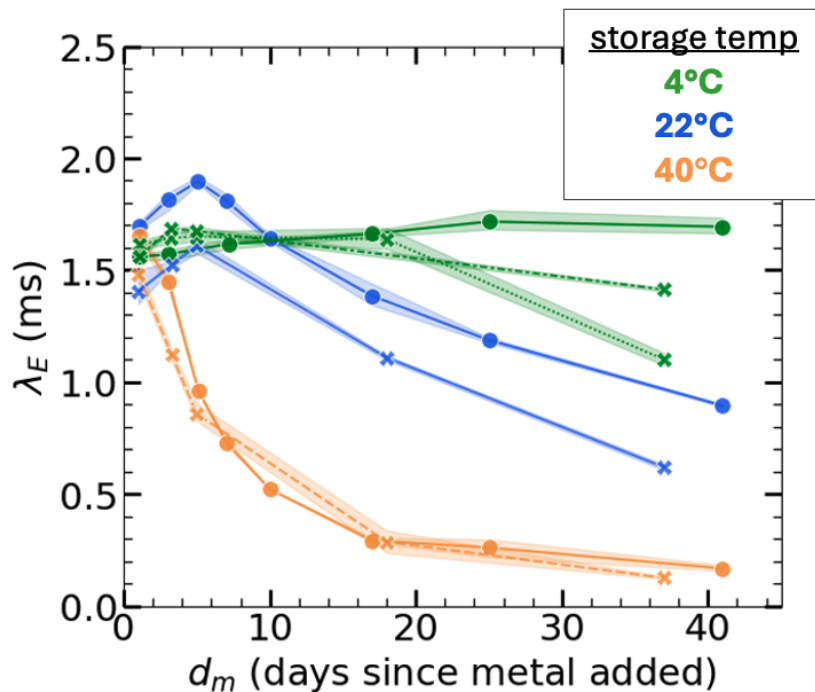


Figure 2.16: λ_E evolution over multiple weeks with samples stored at $T_{store} = 22^\circ\text{C}$, 40°C , and 4°C . Solutions were mixed with metal for 24 hours at room temperature, λ_E at $d_m = 1$ was observed, and the solution was stored at their respective T_{store} and λ_E was monitored after storage. Error bands are shown for $n \geq 3$ DoSER runs on the same sample. $M_{uni} = 0.84$ MDa; Solvent = unbuffered MilliQ; $c = 0.04$ wt%; M:L = 0.5; Dilute \rightarrow Metal; x and o symbols represent samples made with different starting solutions.

of the replicates for the 4°C data point, as the more stable replicate has not begun to decay and a half life cannot yet be estimated, and the least stable replicate was likely affected by confounding factors. We extrapolate the 4°C half life to be 144 days, acknowledging the significant uncertainty associated with this extrapolation, while still enabling us to calculate an approximate activation energy (E_A). Using the Arrhenius analysis described in Section 2.6.1, we can plot k_1 vs $1/T$ to find the slope (Figure 2.17).

Implementing Equation 2.1, we calculate $E_A = 66 \pm 12$ kJ/(mol K). This bounds the activation energy provided by [20] for acid-catalyzed hydrolytic degradation of esters, which determines $E_A = 63.5 \pm 0.7$ kJ/(mol K) with 20 mM HCl (pH

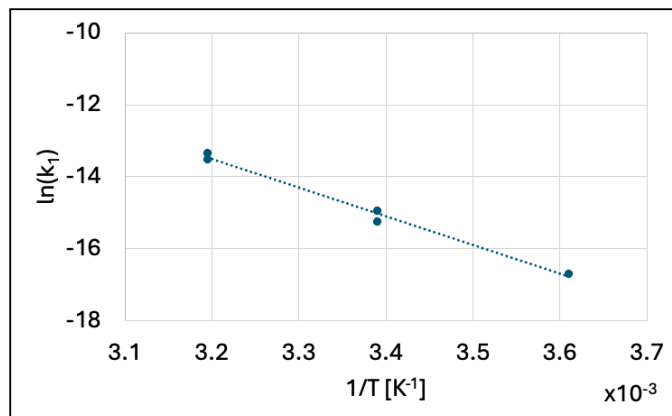


Figure 2.17: Arrhenius plot used to approximate the activation energy of TPAM's chemical degradation mechanism(s). The slope is -7900 with a 95% confidence interval of ± 1400 , corresponding to an activation energy $E_A = 66 \pm 12$ kJ/(mol K) (Equation 2.1).

1.7). However, their reaction took place in a highly acidic solution, whereas ours is only weakly acidic (un-buffered, but measured to be no lower than pH 5.6 due to carboxylic acid formation from air exposure). This provides further evidence that the metal ions could be acting as catalysts for this reaction, which is plausible due to the fact that divalent metal ions can act as catalysts in certain chemical reactions and are often considered Lewis acids. There is also the evident role of oxygen, which can be mitigated, but not eliminated unless in an anaerobic environment (note that oxygen scavenging was attempted as shown in the Supplementary Section 2.8.1). It was also confirmed that microbial degradation is negligible by assessing the colony forming units for all three temperatures at $d_m = 30$; no microbial activity was found (plating performed by Raj Mukkamala).

TPAM degradation with and without the presence of Ni(II) ions at 40°C provides further evidence towards metal ion-catalyzed decay

To assess the TPAM degradation due to dissolution in water alone versus the presence of metal ions, a protocol similar to the one described in Section 2.4.1 was implemented. We create a starting solution of 0.04 wt% 0.84 MDa TPAM in unbuffered, MilliQ water (pH 5.6-6.8). For one sample, we mix 1 Ni(II) for every 2

terpys for one day, measure λ_E using DoSER, then store the sample in the incubator at 40°C to assess the decay in the presence of the metal ions. In parallel, we stored an aliquot of the same starting solution in an incubator at 40° with no metal present. We see the same decay with metal present at 40°C that was previously shown in Figure 2.16, but now we compare it to the λ_E of a TPAM starting solution that was aged in an incubator for 6 days prior to adding Ni(II) (Figure 2.18).

The TPAM starting solution that was aged in the incubator has a λ_E lower than the initial sample on $d_m = 1$, but significantly higher than the initial sample with respect to the day since the polymers were dissolved (d_p). The similarity in the topology between both TPAM solutions as soon as metal is added is highlighted by the similarity of their molecular weight distributions taken on $d_m = 1$. We can also compare the aged TPAM's molecular weight distribution to that of the TPAM mixed with Ni(II) 6 days prior; both traces were taken within the same amount of time the TPAM had been dissolved, but the solution that contained Ni(II) for 6 days has shorter megasupramolecules and more unimers than that which had metal for only 1 day, even after the latter's starting solution had been stored in the incubator (40°C). To add another layer of complexity, the aged TPAM shows a slight initial rise in λ_E after $d_m = 1$, while the initial solution exhibits λ_E decay immediately following $d_m = 1$. This continues to suggest multiple degradation pathways, or at least multiple catalysts, may be at play. It also re-confirms that the decay corresponds to the presence of metal ions, especially considering care was taken to reduce exposure to oxygen once the metal ions were added by storing them tightly sealed in a vial (i.e. not in a Luer lock syringe).

Neutral pH reveals lower λ_E with similar temperature trends

It is reasonable to suspect that pH might be influential to the formation of megasupramolecules. This has been discussed from a standpoint of degradation, but we can also consider its effect on the metal ion ligation dynamics. Frausto (1983) shows

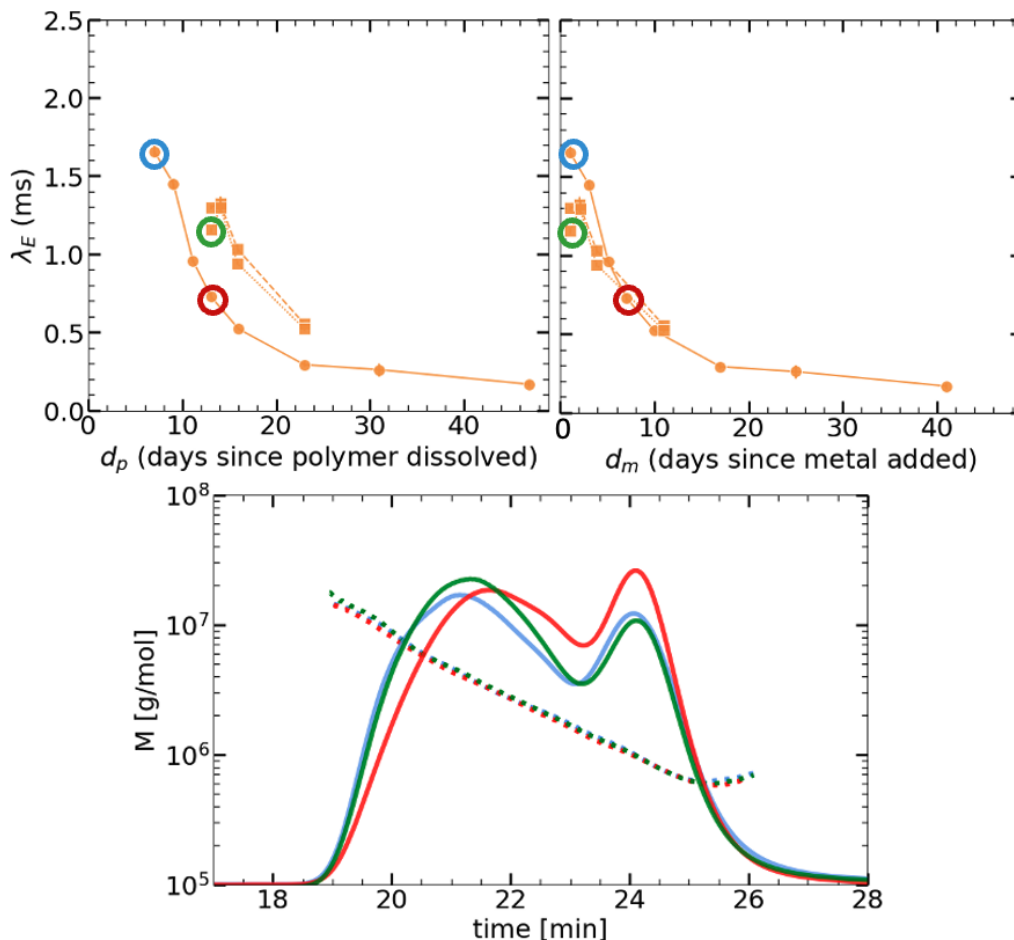


Figure 2.18: λ_E evolution over time stored at 40°C with and without metal ions present.

○: solutions were mixed with metal for 24 hours at room temperature, λ_E at $d_m = 1$ was observed, and the solution was stored at 40°C.

□: the starting solution was stored at 40°C for 6 days with no metal present, then NiCl_2 was added and λ_E subsequently monitored.

$M_{uni} = 0.84$ MDa; Solvent = unbuffered MilliQ; $c = 0.04$ wt%; M:L = 0.5; Dilute → Metal; Vial storage.

Bottom: GPC results for $d_m = 1$ and $d_m = 14$ for the initial solution, and $d_m = 1$ for the followup solution are shown, with distributions corresponding to the colored circles on the λ_E plots above.

that shifting towards a more neutral pH 7 weakens the effect of metal chelation [21], while Lohmeijer et al. (2003) shows there is no pH dependency on Ni(II) chelation as it pertains to terpyridine supramolecules specifically [22]. We probe this by testing the use of two biological Good's buffers in our solvents: HEPES and MOPS. We chose these buffers based on their reported compatibility (i.e. limited interfer-

ence) with metal ions. We ran initial tests with these buffers at pH 7 as reported in Supplementary Section 2.8.2. We tested them again with the temperature protocol as described in the preceding Section 2.6.3, using 15 mM of each buffer at pH 7. HEPES and MOPS demonstrated similar performance, and HEPES was used for the following experiments.

In all cases, λ_E was substantially lower than in a MilliQ solvent. This could be due to the neutral pH hindering the metal ion coordination with the terpyridine. Also plausible, the biological buffers could be directly deterring metal ion coordination with terpyridine by complexing the metals themselves. Interestingly, the neutral pH exhibits shorter λ_E half lives at the various temperatures, as shown in Figure 2.19.

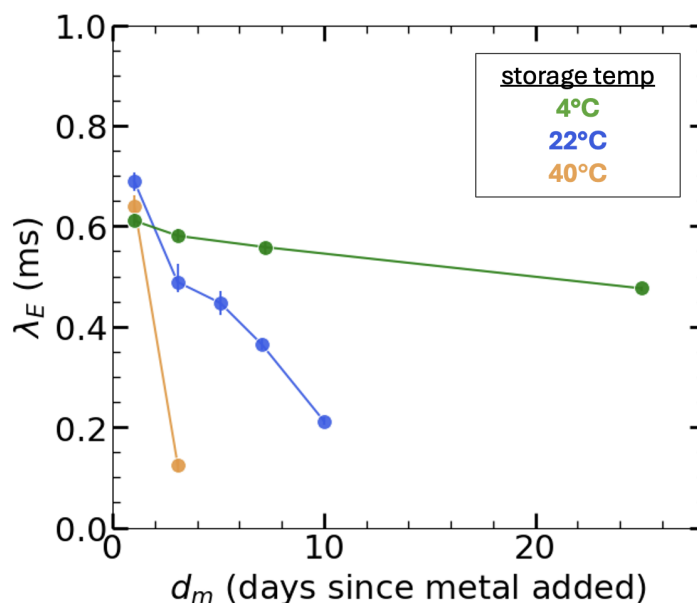


Figure 2.19: λ_E evolution over multiple weeks with samples stored at $T_{store} = 22^\circ\text{C}$, 40°C , and 4°C in HEPES solvent. Solutions were mixed with metal for 24 hours at room temperature, λ_E at $d_m = 1$ was observed, and the solution was stored at 22°C , 40°C , and 4°C with λ_E measured on subsequent days after the various temperature storage. $M_{uni} = 0.84$ MDa; Solvent = HEPES buffer (15 mM, pH 7); $c = 0.04$ wt%; M:L = 0.5; Dilute \rightarrow Metal; Vial storage.

2.6.4 Short-term rise in λ_E also varies with temperature

Considering the significant role temperature plays in the decay rate of λ_E , we suspected it may also influence the short-term rise in λ_E as was first identified in Section 2.2. Storing the solutions at 22°C, 40°C, and 4°C immediately after adding NiCl₂ and measuring λ_E at regular short intervals reveals a clear effect (Figure 2.20). Before the rapid long-term decay already observed in 40°C solutions, a higher temperature actually causes a steeper incline and higher initial λ_E . There is also a delayed rise in λ_E for solutions stored at 4°C. Notably, there is a significant difference in the 22°C replicates; we suspect this difference is primarily driven to differences in air exposure (the lower λ_E TPAM sample has an additional timepoint early on during which the solution was opened for sampling). The variation in sample replicates due to the sensitivity of sample preparation and handling, and how we address it when comparing solutions, is addressed in Appendix A "Quantifying uncertainty and sample reproducibility".

2.7 Conclusions and Future Work

Our findings show that there is a crossover between the rising of λ_E and the eventual decay. As λ_E decays, we posit that the unimers are losing their ability to form associations at their end groups. The observation of the initial, short-term increase in λ_E , highlights the importance of accounting for the time required for the relaxation time to peak in subsequent investigations. The observation of this short-term rise to equilibration was not only essential for instilling confidence that any decay beyond this rise is indeed degradation, but also it is an important insight to bring to the next phase of our investigation. In the next chapter, we look at the crossover region as the time in which the corresponding λ_E and M_w provide the most information about the physics underlying the equilibrated TPAM solutions.

The degree to which we have characterized and mitigated TPAM decay is sufficient

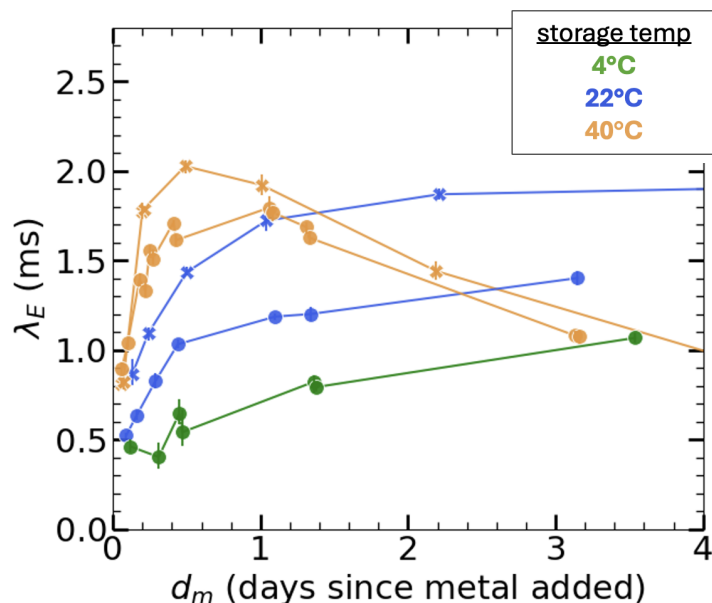


Figure 2.20: Comparison of λ_E short-term rise at different T_{store} : 4°C (refrigerator), 22°C (room temperature) and 40°C (incubator). The solutions were all stored at their respective temperatures immediately after metal was added. The vials were not rolled in storage. Replicates for both 22°C and 40°C are shown from two different starting solutions (one set as a \circ , replicate set as an \times).

$M_{uni} = 0.84$ MDa; Solvent = unbuffered MilliQ; $c = 0.04$ wt%; M:L = 0.5; Dilute \rightarrow Metal; Vial storage.

for continuing our studies on the tunability of TPAM structure and behavior. Our findings demonstrate that while metal ions are essential for the formation of mega-supramolecules, they are also likely playing a role in their eventual degradation. Additional, controllable factors that contribute to decay include air exposure and storage temperature. By limiting exposure to air and storing samples at 4°C, we show that samples, even in the presence of metal ions, can maintain a stable λ_E . We look next in Chapter 3 at the effect of varying metal-to-ligand ratio from two perspectives. First, we provide an insufficient amount of metal to satisfy all the bis-complexes that can form with the terpyridine to assess the effect excess terpys have on the rise and decay of λ_E . In contrast, we also provide an excess amount of metal ions relative to the number of terpys to follow up on the evidence of this chapter that metal ions may be playing a catalytic role in the degradation chemistry.

In terms of industrial practicality, we believe TPAM to be a viable option for an agricultural additive, so long as reasonable steps are taken for stable storage. First, we would suggest that the TPAM and metal solutions are kept separate by their producers before distributing them to their users. From that point, they should be sealed and stored in the fridge until their application and used within 30 days. Prior to this study, with no mitigation precautions taken over 30 days, the λ_E decayed by over 50% [18]. Of course, 30 days is not as long as an ideal 1-2 year shelf life, so we would recommend continuing a long term study with the aforementioned precautions over a desired amount of time as discerned by the producers and end users.

In terms of future work beyond the scope of the current thesis, we aim to identify a more precise mechanism. GPC results indicate that while TPAM's λ_E decays, the polymer backbone remains intact. This points to a decrease in the formation of longer chains due to a growing inability to form links through ligand-metal complexes. We conclude that backbone breakage, either at the central trithiocarbonate due to aminolysis or at random points due to the Fenton reaction, is unlikely. We are actively exploring more diverse and practical methods to identifying the degradation products to elucidate the mechanisms, namely with mass spectrometry experts at Caltech Dr. Mona Shahgholi (formerly) and Dr. Nathan Delleska (currently). A procedure for providing samples to mass spectrometry has already been developed and tested and is provided in the Supplementary Information (Figure 2.25). In the meantime, we can continue our exploratory studies on TPAM with the confidence that the solutions with and without metal remain stable under refrigerated conditions.

2.8 Supplementary Figures

2.8.1 Testing MEHQ as an oxygen scavenger

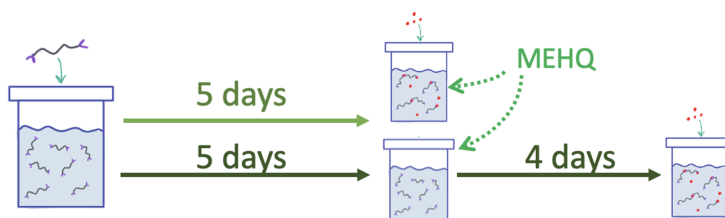


Figure 2.21: Protocol for mixing TPAM solutions with MEHQ alone vs with MEHQ and metal, implemented in attempt to assess whether or not an oxygen scavenger can mitigate decay induced by air exposure.

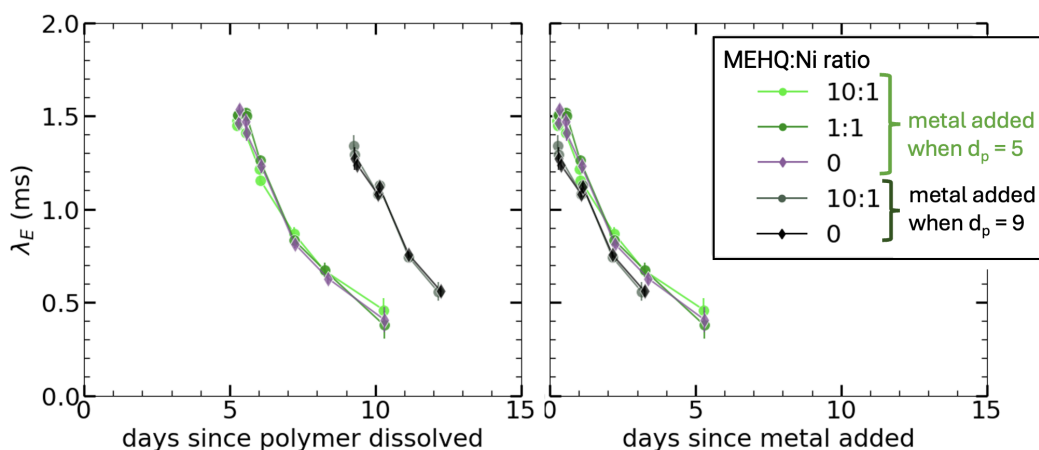
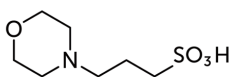


Figure 2.22: DoSER results for TPAM solutions with MEHQ oxygen scavenger, with no apparent harmful or helpful effect at the concentrations considered here.

2.8.2 Initial tests with pH 7 buffer solvents

MOPS, pH 7, 25 mM
 • pKa @ 25C = 7.2



HEPES, pH 7, 10 mM
 • pKa @ 25C = 7.5

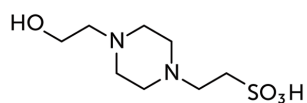


Figure 2.23: The structure and concentration of neutral pH buffers, MOPS and HEPES, used in the present study.

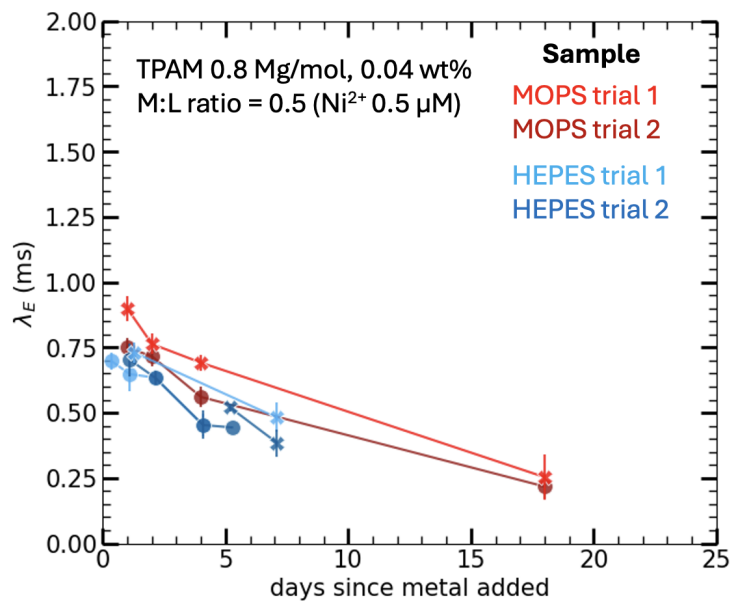


Figure 2.24: DoSER results for TPAM solutions with MOPS and HEPES buffers. Both buffers limit the maximum λ_E .

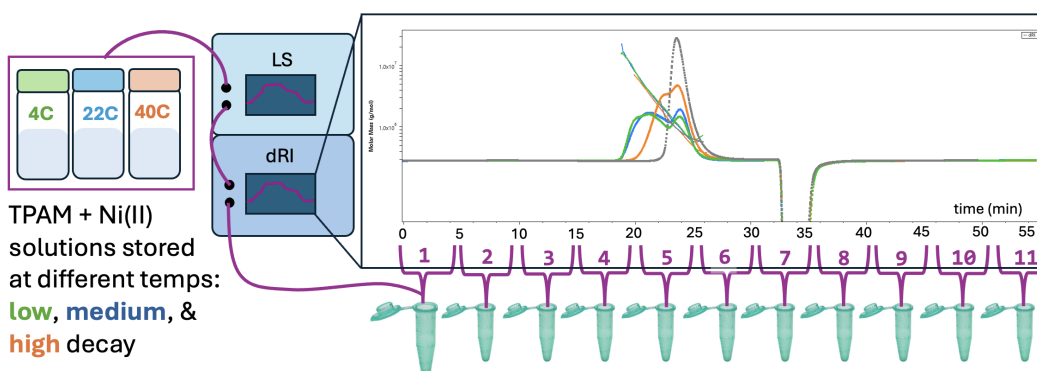


Figure 2.25: Protocol to collect aliquots from the GPC waste line which elutes different sized molecules over time, with the smaller molecules (<6 kDa) eluting at the later timepoints even beyond the resolvable M_w curve. Aliquots were collected, their concentration increased in an evaporator, and ran in mass spectrometry. Results indicated interesting underlying degradation products, however the procedure is to be repeated on a higher resolution mass spec for more definitive results.

References

- [1] Jelena Dinic, Carina D. V. Martínez Narváez, and Vivek Sharma. “Rheology of Unentangled Polymer Solutions Depends on Three Macromolecular Properties: Flexibility, Extensibility, and Segmental Dissymmetry”. In: *Macromolecular Engineering*. Ed. by Nikos Hadjichristidis et al. 1st ed. Wiley, Mar. 4, 2022, pp. 1–36. ISBN: 978-3-527-34455-0 978-3-527-81556-2. DOI: [10.1002/9783527815562.mme0067](https://doi.org/10.1002/9783527815562.mme0067).

- [2] Rishi Shanker, Cherla Ramakrishna, and Prahlad K. Seth. “Microbial degradation of acrylamide monomer”. In: *Archives of Microbiology* 154.2 (July 1990), pp. 192–198. ISSN: 0302-8933, 1432-072X. DOI: [10.1007/BF00423332](https://doi.org/10.1007/BF00423332).
- [3] Antti Nyssölä and Jonni Ahlgren. “Microbial degradation of polyacrylamide and the deamination product polyacrylate”. In: *International Biodeterioration & Biodegradation* 139 (Apr. 2019), pp. 24–33. ISSN: 09648305. DOI: [10.1016/j.ibiod.2019.02.005](https://doi.org/10.1016/j.ibiod.2019.02.005).
- [4] Ehsan Ullah Mughal et al. “Complexes of terpyridine scaffold as efficient photocatalysts for the degradation of methylene blue pollutant in wastewater effluents”. In: *Inorganica Chimica Acta* 546 (Feb. 2023), p. 121329. ISSN: 00201693. DOI: [10.1016/j.ica.2022.121329](https://doi.org/10.1016/j.ica.2022.121329).
- [5] Ramakrishnan Abhijnakrishna et al. “Advances in the Biological Studies of Metal-Terpyridine Complexes: An Overview From 2012 to 2022”. In: *Coordination Chemistry Reviews* 496 (Dec. 2023), p. 215380. ISSN: 00108545. DOI: [10.1016/j.ccr.2023.215380](https://doi.org/10.1016/j.ccr.2023.215380).
- [6] Wasefa Begum et al. “A comprehensive review on the sources, essentiality and toxicological profile of nickel”. In: *RSC Advances* 12.15 (2022), pp. 9139–9153. ISSN: 2046-2069. DOI: [10.1039/D2RA00378C](https://doi.org/10.1039/D2RA00378C).
- [7] Geoffrey K. Kinuthia et al. “Levels of heavy metals in wastewater and soil samples from open drainage channels in Nairobi, Kenya: community health implication”. In: *Scientific Reports* 10.1 (May 21, 2020), p. 8434. ISSN: 2045-2322. DOI: [10.1038/s41598-020-65359-5](https://doi.org/10.1038/s41598-020-65359-5).
- [8] Donald Mackay and Robert S. Boethling, eds. *Handbook of Property Estimation Methods for Chemicals*. CRC Press, Mar. 29, 2000. ISBN: 978-1-4200-2628-3. DOI: [10.1201/9781420026283](https://doi.org/10.1201/9781420026283).
- [9] Christoph Rücker et al. “Biodegradation tests of mercaptocarboxylic acids, their esters, related divalent sulfur compounds and mercaptans”. In: *Environmental Science and Pollution Research* 25.19 (July 2018), pp. 18393–18411. ISSN: 0944-1344, 1614-7499. DOI: [10.1007/s11356-018-1812-x](https://doi.org/10.1007/s11356-018-1812-x).
- [10] Dakrong Pissuwan et al. “In Vitro Cytotoxicity of RAFT Polymers”. In: *Biomacromolecules* 11.2 (Feb. 8, 2010), pp. 412–420. ISSN: 1525-7797, 1526-4602. DOI: [10.1021/bm901129x](https://doi.org/10.1021/bm901129x).
- [11] Maciej Thomas et al. “Removal of Heavy Metal Ions from Wastewaters: An Application of Sodium Trithiocarbonate and Wastewater Toxicity Assessment”. In: *Materials* 14.3 (Jan. 31, 2021), p. 655. ISSN: 1996-1944. DOI: [10.3390/ma14030655](https://doi.org/10.3390/ma14030655).
- [12] Hojin Kim. “New Long End-Associative Polymers for Mist Control in I. Aqueous Solutions and II. Hydrocarbon Solvents”. Medium: PDF Version Number: Final. PhD thesis. California Institute of Technology, Aug. 26, 2022. DOI: [10.7907/RSX9-QT39](https://doi.org/10.7907/RSX9-QT39).

- [13] Reece W. Lewis et al. “Ultra-high molecular weight linear coordination polymers with terpyridine ligands”. In: *Chemical Science* 10.24 (2019), pp. 6174–6183. ISSN: 2041-6520, 2041-6539. DOI: [10.1039/C9SC01115C](https://doi.org/10.1039/C9SC01115C).
- [14] Boya Xiong et al. “Chemical Degradation of Polyacrylamide during Hydraulic Fracturing”. In: *Environmental Science & Technology* 52.1 (Jan. 2, 2018), pp. 327–336. ISSN: 0013-936X, 1520-5851. DOI: [10.1021/acs.est.7b00792](https://doi.org/10.1021/acs.est.7b00792).
- [15] Werner Stumm and G. Lee. “Oxygenation of Ferrous Iron”. In: *Industrial Engineering Chemistry* 53 (Feb. 1961). DOI: [10.1021/ie50614a030](https://doi.org/10.1021/ie50614a030).
- [16] P.Y. Hou. “Oxidation of Metals and Alloys”. In: *Shreir’s Corrosion* 1 (Dec. 2010), pp. 195–239. DOI: [10.1016/B978-044452787-5.00013-5](https://doi.org/10.1016/B978-044452787-5.00013-5).
- [17] David Thomas et al. “Hydrolytic Susceptibility of Dithioester Chain Transfer Agents and Implications in Aqueous RAFT Polymerizations†”. In: *Macromolecules* 37 (Feb. 2004). DOI: [10.1021/ma035572t](https://doi.org/10.1021/ma035572t).
- [18] Robert Learsch. “Droplet control in aqueous and hydrocarbon fluids: Long, end-associative polymers dictate fluid behavior under elongational flows”. PhD thesis. Caltech, Oct. 20, 2022.
- [19] Harry Gray (Personal communication). Dec. 12, 2023.
- [20] Gunnar Aksnes and Fred Olav Libnau. “Temperature Dependence of Ester Hydrolysis in Water”. In: (1991).
- [21] J. J. R. Frausto Da Silva. “The chelate effect redefined”. In: *Journal of Chemical Education* 60.5 (May 1983), p. 390. ISSN: 0021-9584, 1938-1328. DOI: [10.1021/ed060p390](https://doi.org/10.1021/ed060p390).
- [22] Bas G. G. Lohmeijer and Ulrich S. Schubert. “Water-Soluble Building Blocks for Terpyridine-Containing Supramolecular Polymers: Synthesis, Complexation, and pH Stability Studies of Poly(ethylene oxide) Moieties”. In: *Macromolecular Chemistry and Physics* 204.8 (May 2003), pp. 1072–1078. ISSN: 1022-1352, 1521-3935. DOI: [10.1002/macp.200390078](https://doi.org/10.1002/macp.200390078).

*Chapter 3***EXPLORING TPAM MEGASUPRAMOLECULAR WEIGHT DISTRIBUTION AND RELAXATION TIME BY VARYING METAL-LIGAND RATIOS AND BUILDING BLOCK SIZE****3.1 Introduction****3.1.1 Background on exploring tunability of metallo-supramolecule networks**

Metal-ligand coordination is extensively used in supramolecular assemblies because of their relatively strong and easily variable binding energies. Metal-ligand binding energies are generally stronger (100-300 kJ/mol) and thus more stable than hydrogen bonds (4-120 kJ/mol), but still weaker than a C-C bond = 347 kJ/mol) [1, 2]. This makes metal-ligand coordination an optimal choice when both stability and self-healing are priorities. The binding energies can also be varied simply by changing the type and charge of the metal ion in solution, rather than the polymer itself, making it possible to explore a variety of properties with relative ease (i.e. not having to synthesize different polymers to create different structures).

The first report on soluble, metal-ligand coordination polymers came just a few years after the conceptualization of supramolecules. In 1996, Knapp et al. from the Polymer Institute at Karlsruhe University developed supramolecules that were comprised of metal monomers with ligands at both ends, but no polymer spacers within the repeat monomers [3]. Each metal could coordinate with three ligands to form a tri-functional junction. Thus, self-assembly likely formed a dense network. This was a launching point for further studies into soluble, metal-ligand supramolecules, with the first linear, "high molecular mass" molecules consisting of polyethylene oxide (PEO) with terpyridine end groups and divalent metal ion end-to-end complexes [4]. Schmatloch et al. (2003) from Eindhoven University

of Technology studied these terpy-ended PEO "unimers" with a variety of metals, including the series iron, cobalt, nickel, and copper. The distinct metal ions resulted in a range of relative viscosities, and ultimately achieved a maximum estimated molecular weight of 80,000 g/mol for Fe(II) at 20 mg/mL. (For comparison with the present work, their longest supramolecule had M_w an order of magnitude less than the current work's TPAM unimer alone, and orders of magnitude greater in concentration than our solutions.) From this point, researchers began to focus explicitly on control of rheological properties by tuning the metal-ligand coordination polymers' chemistry, notably the earliest works coming from Stephen Craig's group at Duke University. Yount et al. (2005) demonstrated a connection between the metal-ligand association strength and the relative viscosity created by a side-group functionalized poly(4-vinylpyridine) in 100 mg/mL concentrated solution [5]. Loveless et al. (2005) further illuminated the extent of which these associative polymers can be controlled by varying combinations of metal ions, specifically using Pd(II) and Pt(II) [6]. From here, it became apparent that variations in polymer shape and size, ligand-metal binding energies, and their relative concentrations can be used to influence and even control the supramolecular structure, solution properties, and ultimately, material behavior.

While the earlier work looked specifically at end-to-end bis-complexes for linear molecules [3, 4], the majority of recent work has shifted focus to tunable, self-healing, metallo-supramolecular hydrogels. In the review by Brassinne et al. (2013), they explain 3D network gels can be formed either through varying the topology of the building block unimers (i.e. using cross-linked, branched, star-shaped polymers) or by varying the type of ligand and metal ion to allow three or more ligands to form a complex [7]. Existing research on exploring metallo-supramolecular hydrogels indicates the potential for dynamic, tunable bulk rheological properties by varying the unimer structures and the types and relative amounts of metal ions and ligands [8,

9, 10, 11, 12, 13, 14]. Mozhendi et al. (2016) in a collaboration between UC Irvine and MIT found that for polymers cross-linked with dangling ligands, the availability of excess ligands played a crucial role in the hydrogel's behavior under shear and tension [10]. Simply by increasing the relative amount of ligands to metal ions, they could control the material's structure and dynamic response. This provides inspiration for varying these same properties for linear, end-associative metallo-supramolecules to see if a similar tuning effect can be achieved within complex fluid solutions.

3.1.2 Topological landscape of TPAM megasupramolecules

"Supramolecules" are formed through the self-assembly of smaller molecules, often referred to as "building blocks" or "unimers". The term "megasupramolecules" was introduced to describe supramolecules over 1,000,000 g/mol formed by pair-wise end-association of flexible linear polymers. Initial research on megasupramolecules focused on linear supramolecules and closed rings [15]. By understanding the topology of these megasupramolecular structures (that is, the way the molecular components interact and connect with each other) we can tune chemical structures to satisfy the necessary bulk rheological properties and solution behaviors. More specifically, for instance, we can increase the degree that the unimers associate and the size of the linear species that form, which increases the relaxation time, resulting in a higher extensional viscosity and more tunable options for various applications. In addition to this practical knowledge required for engineering settings, by investigating the implications of topological changes, we can provide fundamental theoretical insights into the dynamics driving these complex fluid systems.

In this study, we focus on end-associative metal-ligand megasupramolecules that form through the coordination of divalent metal ions with terpyridine ligands installed at both ends of water-soluble polymer chains (denoted TPAM: T for ter-

pyridine, PAM for polyacrylamide). For our bis-terpy complexes, forming from our bi-functional TPAMs, the only species hypothesized to exist in our solutions are "rings" (when the two ends of a molecule connect to itself to form a loop) or "linears" (when the two ends are free, either due to no metal being present on the end or only one without a second terpy). These megasupramolecular species exist in dynamic equilibrium, and their distributions can vary (Figure 3.1).

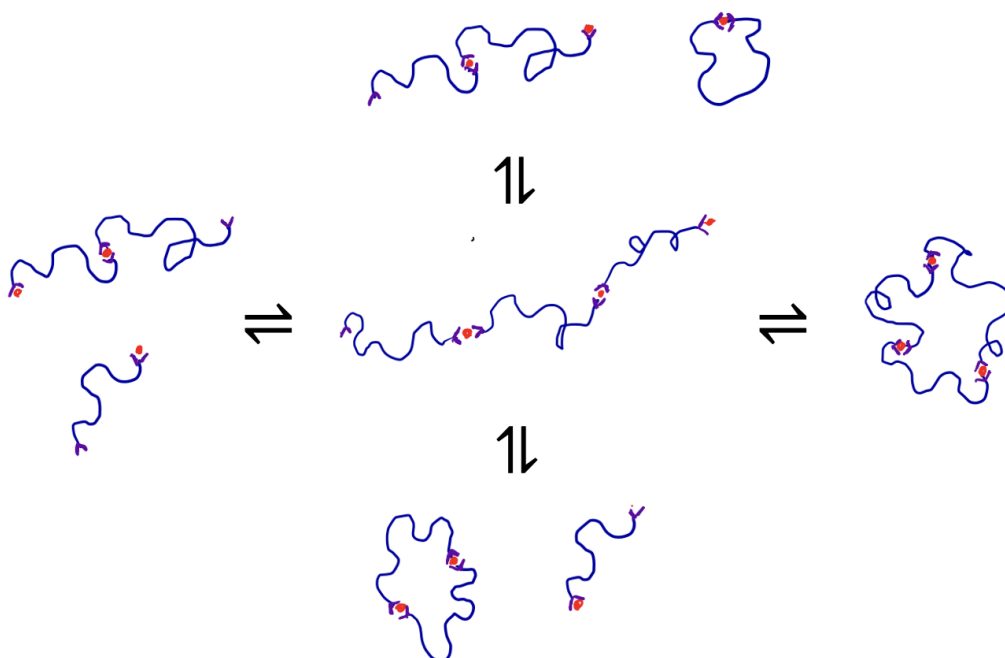


Figure 3.1: Schematic of the dynamic equilibrium of megasupramolecular species that can exist given the same amount of unimer and metal ions.

Differences in distributions can arise for kinetic reasons (as discussed in Chapter 2), but they also depend on the variety of factors that alter the equilibrium of metal-ligand coordination sites. These factors include, for example, the association strengths of the metal-ligand coordination, their relative concentrations, the lengths of the unimers, the unimer concentration, and polymer-solvent interactions. We experimentally explore variations caused by metal-to-ligand ratio and unimer molecular weight, which as we will show provides access to a range of

megasupramolecular formations and viscoelastic fluid properties. We supplement these takeaways by addressing what a model for end-associative polymers suggests may be achievable by varying the same parameters as well as others that were not experimentally addressed for the present investigation.

Looking ahead to Chapter 4, we will present evidence that more complex topologies, along with an expanded range of properties, may form with a change in solution mixing protocol (adding metal to the TPAM solution at high concentration before the final dilution, $c/c^* \approx 0.14$). In the current chapter, we lay the groundwork for this discovery by characterizing the behavior and range of fluid properties that result from implementing our standard mixing protocol (adding metal to the TPAM solution after it has reached its final diluted concentration). We start with an in-depth discussion on the anticipated consequences of varying certain chemical conditions, from both theoretical and empirical perspectives.

3.1.2.1 Metal-to-ligand ratio: What are the consequences of insufficient or excess metal?

We can begin thinking about metal-to-ligand ratios (denoted M:L) by considering the extensively studied topic of stability constants as they relate to the theoretical equilibrium distribution of the terpy-ion complexes and their components [16]. We refer to a terpy ligand with no metal or one metal as an "end cap" (since it is where a chain would cease to connect with another TPAM) and a metal with two ligands as a "link" (since this is where two TPAMs connect). This approach was taken by Lewis et al. (2019) to assess the end group fidelity (how many ends actually have end groups attached) and predict the maximum theoretical molecular weights [17]. We will use this approach to conceptualize the topological possibilities and limitations at different ratios, and ultimately, to inform an expanded model that considers the thermodynamics of a more complete polymer system.

Our known inputs include the concentration of terpy ligands $[L_0]$, metal ions $[M_0]$ and the equilibrium constants K_1 and K_2 . From one metal and ligand, a metal-ligand end cap can form $[ML]$, and with another ligand, a ligand-metal-ligand linkage can form $[LML]$. These inputs and products are illustrated in Figure 3.2 and described by metal-ligand equilibrium relations (Equations 3.1 and 3.2) and conservation of ligand and metal (Equations 3.3 and 3.4).

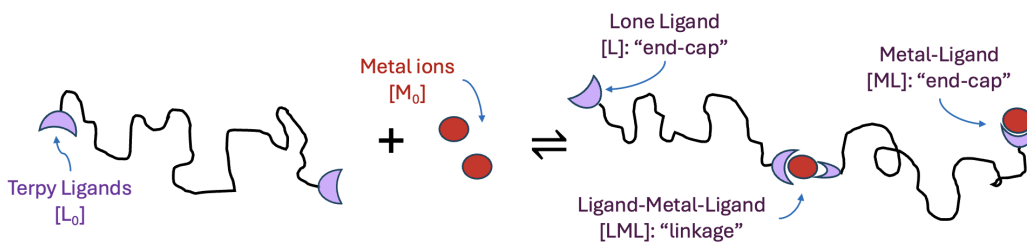


Figure 3.2: An illustration of megasupramolecule formation from TPAM unimers. For specified concentrations of terpy end groups ($[L_0]$) and metal ions ($[M_0]$), megasupramolecules form via ligand-metal-ligand linkages ($[LML]$). Linear species are terminated by "end-caps" ($[L]$ and/or $[ML]$). The concentration of linkages, end-caps, and excess free metal ions are governed by metal-ligand equilibrium relations (Equations 3.1 and 3.2) and conservation of ligand and metal (Equations 3.3 and 3.4). The distribution of species includes linear (shown) and cyclic (not shown) supramolecules with integer multiples of unimers.

$$[ML] = K_1 [M] [L] \quad (3.1)$$

$$[LML] = K_2 [ML] [L] \quad (3.2)$$

$$[L_0] = [L] + [ML] + 2[LML] \quad (3.3)$$

$$[M_0] = [M] + [ML] + [LML] \quad (3.4)$$

For a specific system of ligands, metal, pH, and temperature (which dictates K_1 and K_2), this system of equations can be used to theoretically determine how varying the M:L ratio ($[M_0]/[L_0]$) affects the equilibrium concentration of linkages and end-caps. It can also be used to anticipate how the choice of metal, ligands, pH, and temperature affect the concentration of linkages and end-caps. Equilibrium

constants for various metal-ligand complexes have been experimentally determined and are commonly referenced in literature [16]. We will focus on the set of $\log(K_1) = 10.7$ and $\log(K_2) = 11.1$ that corresponds to our primary ion of interest, divalent nickel (i.e. Ni(II) or Ni²⁺). Ni(II) is especially useful here because of its higher K_2 (increased tendency to form linkages) as well as its resistance to oxidation (which would inhibit the bis-complex formation) [18]. Note that previous studies have indicated that the Ni(II)-terpy complex is unaffected by changes in pH [19].

By specifying our system's stability constants, we solve Equations 3.1 through 3.4 and assess the possible variation in the respective equilibrium amounts of free metals, ligands, and metal-ligand complexes based on changing the M:L ratio alone (Figure 3.3). When there are no metal ions in the solution (M:L = 0), we see exclusively free ligands. As the ratio increases, according to theory, we see only free ligands and ligand-metal-ligand linkages until all ligands are satisfied by a metal (i.e. M:L = 0.5, or one metal for every two terpys, the stoichiometric equivalent). After this point, we see a slower, monotonic decrease in the amount of ligand-metal-ligand linkages, with a rise in metal-ligand end-caps and free metals in solution.

If our goal is to maximize the amount of ligand-metal-ligand linkages, which drives the formation of the supramolecules, then we should aim for the stoichiometrically equivalent M:L = 0.5. However, this simplified model does not account for the formation of linear versus cyclical supramolecular species. If our actual aim is to explore ways to increase TPAM's megasupramolecular weight and expand their rheological capabilities (i.e. λ_E and self-healing), we must consider how the ratio of linkages and end-caps, as well as the variety of other physio-chemical properties (i.e. concentration, unimer M_n , bond strength), could influence the topology more broadly.

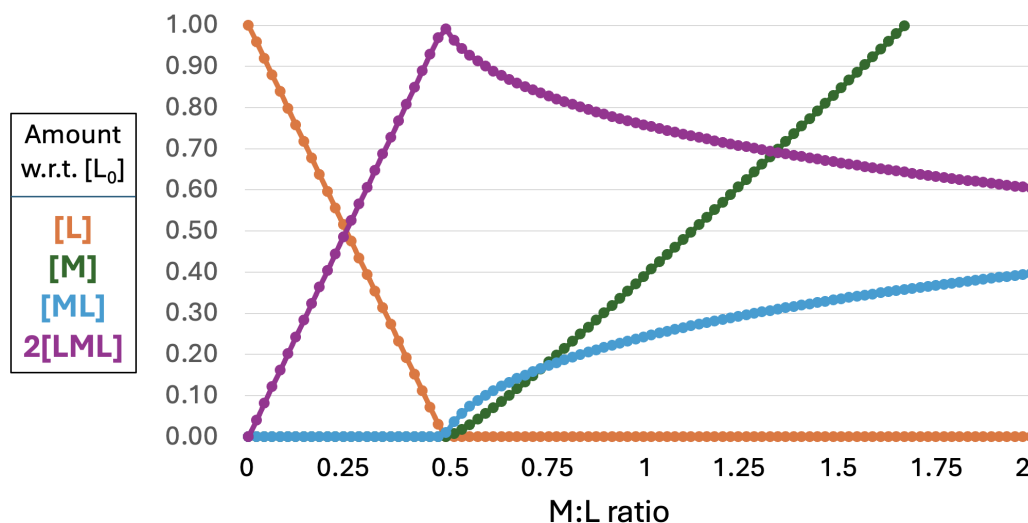


Figure 3.3: By varying the M:L ratio (x-axis), we can create different respective amounts of free metals, ligands, and metal-ligand complexes (y-axis, normalized by the initial free ligand concentration L_0). The plot presented here is calculated for terpyridine and Ni(II) using the system of equilibrium and conservation equations given by Eqns 3.1 through 3.4).

3.1.2.2 Modeling insight on effect of unimer M_w and beyond

To the best of our knowledge, the first attempt at an end-associative megasupramolecular thermomechanical equilibrium model was presented in Dr. Ameri David's thesis under the guidance of Prof. Julia Kornfield at Caltech [20]. David's model considered a donor-acceptor association scheme, rather than a "self-associating" metal-ligand scheme, like ours. The major difference between the two scenarios is that our terpyridine-ended polymers can self-associate and therefore can form unimer rings, whereas donor-acceptor associations can only form di-mer rings or any even combination (i.e. there are two different unimer types, one with donor ends and another with acceptor, and the same type cannot connect).

In brief summary, David's model builds on the fundamental concepts of entropy and free energy as they pertain to polymeric solutions. The system of equations he creates to solve for the relative concentrations of linear and cyclical species of their various supramolecular sizes comes from the fundamental principles of chemical

potential equilibrium and conservation of mass. He calculates the entropic cost of a loop closure by finding the probability density function (PDF) of loop closure based on Gaussian linear chains of M_K Kuhn monomers of length b , considering the small distance chain ends have to be to form a loop (x/b) and the excluded volume of monomers for real chains (g_T). He assumes that all polymer chains are dilute enough to ignore polymer-polymer interactions and that all chain segments larger than g_T are fully swollen. From here (we adapt the final equation to represent a self-associating system of one type of unimer), he finds the entropic cost of closing a loop (Equation 3.5) by solving for the Gaussian PDF for the loops ($G_{cyc,g}$) (Equation 3.6), where n_g represents the number of unimers in that group g .

$$\Delta S_{loop} = -k \ln(G_{cyc}) \quad (3.5)$$

$$G_{cyc,g} = \left(\frac{6}{\pi g_T^3} \right)^{1/2} \left(\frac{x}{b} \right)^3 \left(\frac{n_g M_K}{g_T} \right)^{1.66} \quad (3.6)$$

This reveals a couple key dependencies, namely, ΔS_{loop} depends on M and n_g . Meaning, cyclical species are disfavored in the supramolecules built from a larger number of unimers (n_g), and that cyclical species can be mitigated with higher M_K unimers (which, for the same polymer backbone, translates to a higher M_w). However, the latter comes at the cost of increased susceptibility to irreversible mechanical scission if the unimers become too long. Having control of the rheological properties through associative polymers hinges on finding a balance between using long unimers without making them so long that they will irreversibly break. Ameri explored the effect of forcibly adding end-caps into a solution at the start and showed that increasing the number of end-caps decreases the amount of rings, but it also decreases the overall megasupramolecular molecular weight (M_w). In our case for TPAM megasupramolecules, the number of end-caps can be tuned by varying M:L. The effect of this balance between a higher number of end-caps, resulting in fewer

rings and lower M_w , is explored in this thesis by experimentally varying the M:L ratio. This M:L ratio can serve as an experimental comparison to David's ring and linear species equilibrium model, as his system was not directly comparable to experiments due to limitations of the associative hydrogen bond timescale incompatibility with GPC [15]. We have adapted his model for our case of self-associative unimers in order to work towards such a comparison.

3.1.3 Empirical insight on λ_E , M_w , and c

Much of the long-standing existing literature, both experimental and well-established theoretical models, focuses on relaxation times as it relates to shear conditions. In this flow regime, Rouse and Zimm theories can be used to predict the dynamics of complex polymeric fluids [21]. Rouse theory treats the polymers as a "bead-and-spring" and ignores hydrodynamic interactions between the individual polymers, while Zimm theory considers hydrodynamic interactions and is thus more useful for higher concentrations and/or higher molecular weights. However, neither model is able to fully capture the dynamics of extensional flows [22, 23]. Under extensional flows, the polymer chains elongate, which increases their degree of overlap and changes the relevant inter-chain and chain-solvent molecular forces [24]. This ultimately elicits an extensional relaxation time (λ_E) that can be many orders of magnitude longer than its shear counterpart (λ_S) for non-Newtonian fluids [25, 22].

Researchers are still actively investigating the connection between rheological behavior and macromolecular properties, such as molecular weight distribution, concentration, and the polymer backbone [22]. Significant progress has been made in large part thanks to the development of Dripping onto Substrate Extensional Rheometry (DoSER) in 2015 [26] (detailed in Chapter 1 and implemented throughout the present work). The researchers responsible for this advancement have used this novel experimental tool to connect their data to theory, postulating that Rouse-

Zimm theory for semi-dilute chains can be used to describe the scaling relations of dilute stretched chains in extension [27, 22]. This result suggests a power-law exponent scaling such that $\lambda_E \sim c^m$, where m can be related to the solvent quality. This power-law exponent has been measured on a variety of polymers and solvents in previous studies, resulting in insightful observations. However, there has been no cohesive, quantitatively predictive outcome, suggesting a greater understanding and consideration of the underlying extensional dynamics is needed. Soetrisno et al. (2023) explores this further, connecting λ_E 's concentration regimes to molecular weight distribution [23]. While they don't endeavour to provide a scaling relationship between M_w and λ_E , their study on different polyacrylamides (PAM), ranging from a "uniform small polymer" (194 kDa, PDI = 1.24), "uniform large polymer" (1.97 MDa, PDI = 21), and "disperse long polymer" (1 MDa, PDI = 29), emphasizes the importance of molecular weight distribution on extensional behavior. Their results highlight the significance of long, polymer chains on PAM's λ_E and suggest that a weight-averaged intrinsic viscosity is better suited for predicting the extensional behavior of polymer solutions.

In an attempt to provide a quantitative scaling description between extensional behavior, polymer length, and concentration, Dr. Rob Learsch (from the Kornfield group at Caltech) performed DoSER on a range of molecular weights and concentrations with PAM (Figure 3.4) [28]. From this sweep, he determined a scaling relationship that indicates a power-law dependence between the molecular weight and λ_E that is more significant than the contribution of concentration (at the concentrations considered) (Equation 3.1.3). This observation is supported by Soetrisno's more qualitative description that came out within the following year.

$$\lambda_E = M_w^{3.6} c^{0.77} \quad (3.7)$$

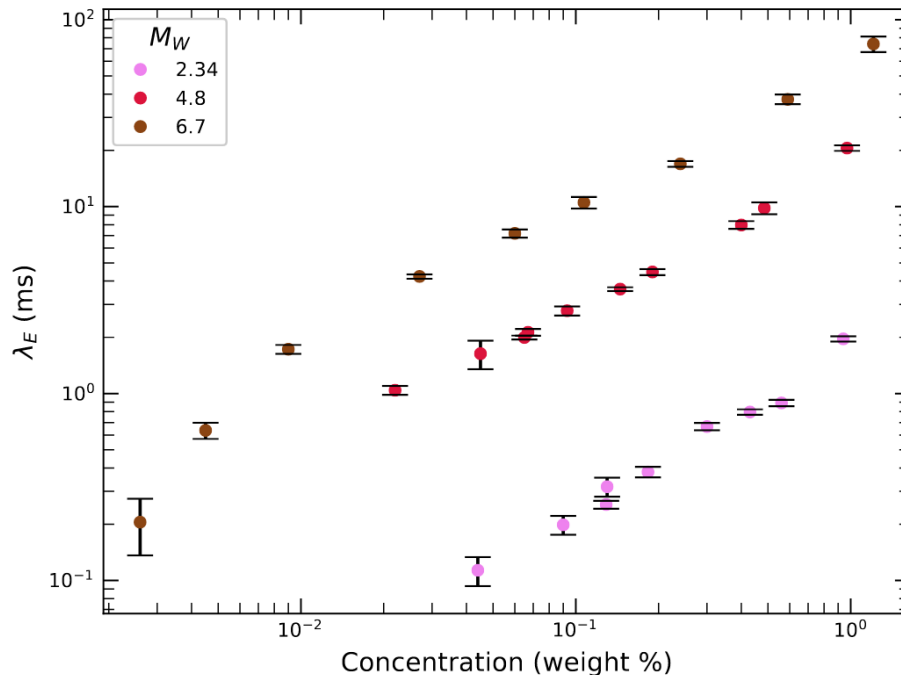


Figure 3.4: Figure from Learsch [28] used with permission. It shows the relaxation time λ_E for covalent PAM with varying weight average molecular weight (M_w) and concentration.

Considering the relative lack of experimental insight relating molecular weight distributions to extensional behavior specifically, we naturally build this into the present study on TPAM. Through assessing TPAM's readily adjustable megasupramolecular weight distribution and resulting λ_E , we provide further experimental data on their relationship and inspiration for future modeling endeavours.

3.1.4 Scope of current chapter

End-associative TPAM's M_w distributions and λ_E in aqueous solution are tuned by varying the metal-ligand ratios (M:L) and unimer molecular weights. We gain insight on these varied molecular effects by comparing the observations of extensional flow behavior (measured with DoSER) with the molecular weight distributions (measured with GPC). We assess how these changes influence TPAM's megasupramolecular size, equilibration and decay dynamics, and λ_E .

3.2 Metal-ligand ratio affects TPAM's associative M_w distribution and λ_E

3.2.1 Experimental protocol for M:L ratio sweep

We start our exploration into M_w distributions and tuning λ_E by building on Chapter 2 and using the same unimer size (840 kDa) with NiCl_2 . In this section, we observe the effects of varying the M:L ratio. Solutions are made first by dissolving 1 wt% of TPAM in unbuffered (weakly acidic) MilliQ water (400 mg TPAM in 40 g of water). The solid polymer is dissolved for 3 days on a Wrist Action Shaker. After the polymer is dissolved, it is further diluted to 0.04 wt% with fresh MilliQ water. The diluted solution is rolled at 10 rpm overnight, then is split into 10 mL aliquots and stored in plastic vials. Ni(II) ions are added by pipetting varying amounts of stock 0.5 mM NiCl_2 solution into the 0.04 wt% TPAM solutions. The precise time the metal is added is recorded so that subsequent experiments can be related to the days that have passed since the metal was added (denoted as " d_m ").

3.2.2 Varying M:L illuminates a gradual increase in TPAM's megasupramolecular M_w

We use GPC to understand how the TPAM supramolecular weight distributions are affected by M:L, and in turn, relate that to λ_E in the following sections. GPC was run when λ_E stabilized, assuming at this point the solution's topological distribution was at or near equilibrium. There are clear differences in the M_w averages and distributions (Figure 3.5 and Table 3.1), and the key observations and implications will be discussed. It is important to emphasize the dotted lines, corresponding to the molecular weight (y-axis) at the given elution time (x-axis), all overlap for these GPC runs. This indicates that species of the same pervaded volume all had approximately the same molecular weight (and conformations), while the difference is highlighted by the solid lines, corresponding to the respective amounts of each molecular weight in the varied solutions.

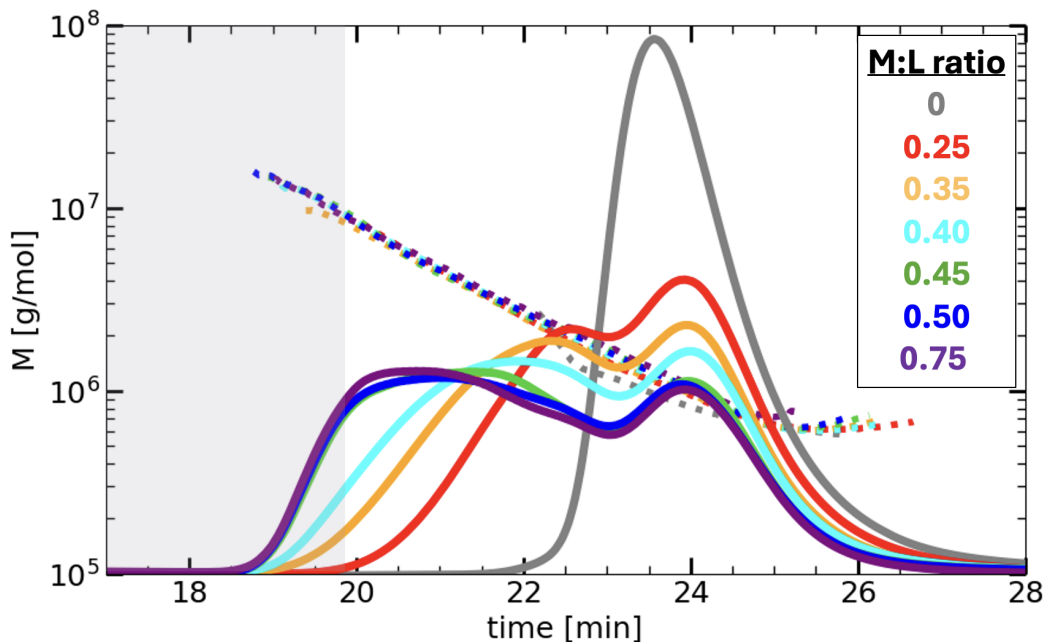


Figure 3.5: M_w distributions collected with GPC for TPAM with NiCl_2 added such that the M:L ratio = 0.25, 0.35, 0.4, 0.45, 0.5, and 0.75. GPC was run on $d_m = 1, 2, 1, 2, 3,$ and $2,$ respectively (near the maximum λ_E values shown in Figure 3.6). The dotted lines correspond to the y-axis M [g/mol], which shows the molecular weight eluting at the given time on the x-axis. The solid lines represent the relative concentrations of molecules eluting at that time at the corresponding molecular weight. The grey box represents the upper limit of the GPC detection (10^7 MDa). $M_{uni} = 0.84$ MDa; Solvent = unbuffered MilliQ; $c = 0.04$ wt%; Dilute \rightarrow Metal; Vial storage.

We see that with more metal ions present in the system, the TPAM unimer that is centered around a single peak at 840,000 Da gradually shifts to form new, larger peaks (Figure 3.5). TPAM mixed with the lowest (and least stoichiometrically sufficient) M:L = 0.25 reveals a second peak centered just below 2 MDa, indicating primarily di-mers and unimers are present in this solution. Given that the free energy of the system decreases when there are two terpys per metal (a linkage) rather than one terpy per metal (an end-cap), this TPAM solution likely contains rings along with linears. As the M:L ratio increases to 0.35 and 0.4, so does the size and concentration of TPAM megasupramolecules. Adding more metals allows for more ligand-metal-ligand linkages to form, and we see a decrease in unimer concentration to accompany

that effect. By M:L = 0.4, the TPAM megasupramolecular distribution's second peak is centered around 3.5 MDa, indicating a significant amount of 4-mers present, and even larger molecules as the tail extends to 10 MDa.

Once we approach and surpass the "ideal" metal ion amount (one ion for every two terpys, known as the stoichiometric equivalent), the TPAM solutions exhibit a substantial increase in the amount of high M_w species and an increase in their overall size for M:L = 0.45, 0.5, and 0.75. However, at this point the difference between these ratios is less clear, for a very important reason—we have surpassed the upper limit of the GPC M_w detection—10 MDa! It's actually quite astounding that we are pushing this upper limit, as it indicates that we have a substantial amount of megasupramolecules comprised of 12 unimers *and beyond*.

Before the GPC limit is reached, we can make some observations about the TPAM solutions with varying M:L near and beyond the stoichiometric equivalent (M:L = 0.5). The M:L = 0.45 solution appears to peak at a slightly later time than M:L = 0.5, indicating slightly smaller species on average, while M:L = 0.75 peaks a little sooner, indicating slightly larger species on average. These three solutions appear to have nearly the same amount of unimers relative to the lower M:L ratios (0.25 - 0.35), but looking closely, there is a very slight decrease in unimer as the M:L ratio increases. This begs the question if there are more significant changes in the megasupramolecular region happening that are obscured by the GPC limit. Once we reach M:L = 0.5, we expect that all the terpyridine have formed bis-complexes with Ni(II), but beyond this point, we have a much more complicated mixture of metal-ligand "end-caps", metal-ligand-metal "linkages", and free metal ions (Figure 3.2). This change in the number of end-caps and linkages can cause a reshuffling of the distributions of ring and linear species as well as their respective sizes. To uncover how much larger these molecules are, and their relative distributions, we would need a new GPC column with a greater M_w limit. These columns exist,

however, the necessary systems are costly and may be explored in the future. There are also possibly better systems for exploring this size range, which we are actively pursuing, as mentioned in the Future Work section of Chapter 4.

The most exciting aspect of the present result is that we have undoubtedly created megasupramolecular species, with a substantial amount of molecules surpassing the 10 MDa limit of our GPC. We have illuminated how their M_w distributions can be tunable simply by varying the amount of metal added to dilute solutions. However, it is unclear from GPC alone if, and by how much, this enables tunable extensional rheological behaviors, so we now turn to the DoSER method to assess the evolution of λ_E after metal is added to the TPAM solutions. Specifically, we are still left wondering if the variation in traces for M:L = 0.25, 0.35, and 0.4 causes an equally variable change in λ_E . Also, crucially, we can use DoSER to provide some insight on what is hidden by GPC the limit and see if M:L = 0.5 and beyond are altering the molecular weight distribution enough to affect the rheological behavior of TPAM.

M:L	Total		Megasupramolecular		
	M_w	PDI	M_w	PDI	c [wt%]
0.25	1.67	1.4	2.60	1.2	0.019
0.35	2.23	1.6	3.18	1.3	0.025
0.40	2.83	1.8	3.97	1.4	0.027
0.45	3.61	2.0	4.91	1.4	0.028
0.50	3.69	2.0	5.09	1.4	0.028
0.75	3.92	1.9	5.23	1.4	0.028

Table 3.1: Summary of molecular weight distributions for a solution of 0.04 wt% 0.84 MDa unimers in un-buffered MilliQ water at various M:L ratios. The "Total" M_w and PDI are for the total GPC trace including the unimer peaks (the total c = 0.04 wt%). The "Megasupramolecular" M_w , PDI , and c are calculated just for the megasupramolecule peak, excluding the unimer peak. All molecular weights have a measurement uncertainty of < 2%.

3.2.3 Increasing M:L ratio increases λ_E , until it doesn't

The TPAM solutions, made with 0.84 MDa unimers at a range of exhibit a range of values and behavior as the M:L ratio is varied from "insufficient" ions (M:L = 0.25, 0.35, 0.4) to "excessive" (0.75, and 1.5) with respect to the stoichiometric ratio of M:L = 0.5 (Figure 3.6). Before an in-depth analysis of the present results, it is important to highlight how we quantify error and sample uncertainty in Appendix A. We identified that, for samples made from the same starting solution dissolved in unbuffered MilliQ water with their first test on $d_m = 1$ (controlling air exposure), their λ_E values could vary by 13%. We place error bands on the results to indicate that the absolute values of λ_E could vary beyond the measurement error from DoSER on a single sample (shown in error bars where visible beyond the size of the symbol). However, over the course of our M:L ratio sweeps for multiple unimer sizes (discussed in later sections and shown in Figures 3.12 and 3.13) we found that the overall shapes of the λ_E evolution are reproducible. Therefore, the band ultimately represents how the set of points for each sample could shift up and down, relative to the measured λ_{ES} .

We first explore what happens when we mix TPAM mixed with an "insufficient" amount of ions at M:L = 0.25, 0.35, 0.4 (Figure 3.6 Left). This set of solutions reaches their maximum λ_E quickly and decays more slowly, with insignificant decay noted within the first week at room temperature. Their quicker equilibration can be explained by the fact that when a ligand-metal mono-complex encounters another ligand, there is no activation barrier to forming a ligand-metal-ligand bis-complex (also known as a linkage). This is particularly true for M:L = 0.25 and 0.35, where all of the metals have rapidly formed ligand-metals mono-complexes, and there are still many free ligands in solution. It's more likely for these ligand-metal mono-complexes to encounter another ligand, which has no activation barrier to forming a linkage. The lack of decay can be explained by the fact that the metals find their

terpys more quickly, therefore subduing their catalytic behavior that was identified in Chapter 2. Comparing TPAM's variation in λ_E with the molecular weight distributions for this lower range of M:L (Figure 3.5), we see that the M_w distribution appears to be much more varied than the rheological behavior. This suggests that the differences in λ_E are driven primarily by the larger megasupramolecules, and that the change in unimer peak is inconsequential. This result makes sense when compared to an existing studies on the effects of standard PAM's M_w distribution on λ_E [23, 28], which we will quantitatively explore in the next section.

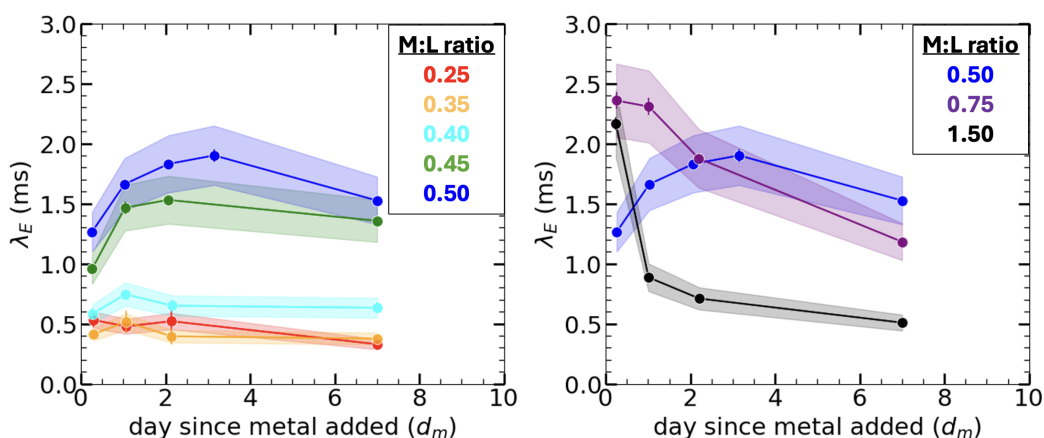


Figure 3.6: Evolution of λ_E for $M_{uni} = 0.84$ MDa unimers observed with respect to days since metal added (d_m) for M:L ratio = 0.25, 0.35, 0.4, 0.45, 0.5, 0.75, and 1.5. Error bars: $n_{drops} \geq 3$; Error bands: $13\% \pm$ uncertainty (see Appendix A). $M_{uni} = 0.84$ MDa; Solvent = unbuffered MilliQ; $c = 0.04$ wt%; Dilute \rightarrow Metal; $T_s = 22^\circ\text{C}$; Vial storage.

TPAM mixed with a more ideal stoichiometric equivalent ratio (M:L = 0.5) shows a large jump in λ_E , as well as a slower rise towards its maximum within the first 2-3 days. This rise in λ_E is expected, as there is 1 ion for every 2 terpys, maximizing metal-ligand linkages. We reason that as more TPAMs complex more metal ions, it takes more time for them to find the available but physically distant partners to form linkages at dilute concentrations. However, we also see that as more of these ions are available to catalyze the λ_E decay, and the peak is shorter-lived. We note that we have increased TPAM's λ_E measured in previous work that was prepared with

similar conditions (Learsch observed a maximum $\lambda_E \approx 0.8$ ms for 0.8 MDa TPAM with M:L = 0.5) [28]. This increase in measured λ_E compared to Learsch's may be due to our more regular measurements, which were centered around the time of the equilibration peak with respect to day since metal added. We speculate that the previous study is not representative of the true maximum λ_E for that system, but rather it is a point along the path towards equilibration. We were successful in acquiring the TPAM M_w distributions (Figure 3.5) on the day λ_E either reached or was near its peak (GPC was run on $d_m = 1$ for M:L = 0.25 and 0.4, $d_m = 2$ for M:L = 0.35 and 0.45, and $d_m = 3$ for M:L = 0.5). The M_w distributions further indicate that as the TPAM megasupramolecules become longer, so does the λ_E . When TPAM is mixed with M:L = 0.45 and beyond, the TPAM megasupramolecules begin to surpass the GPC upper limit (10 MDa), but the difference in the λ_E suggests that there likely is a difference in the distributions that currently eludes us due to measurement limitation.

Pushing the M:L ratio beyond its stoichiometric equivalent results in TPAM solutions reaching the highest observed λ_E for this set of solutions (noting that the lower bound of uncertainty does slightly overlap with that of M:L = 0.5) (Figure 3.6 Right). Adding an excess amount of ions at M:L = 0.75, $\lambda_E = 2.5$ ms is measured within one day of metal added ($d_m < 1$). Notably, this is the maximum λ_E value observed for all ratios tested on all days, but it quickly decays. The equilibrium solution may result in less cyclical species due to the excess metals which promotes more metal-ligand mono-complex end-caps, which could theoretically drive up λ_E by making it entropically more favorable for linear species to persist at a shorter amount of time. However, the excess free metal ions appears to catalyze degradation more readily and rapidly, and the λ_E starts to decay sooner than in the cases with no or negligible excess metal.

Adding even more excessive ions (M:L = 1.5) where there are more metal ions than

can be satisfied by the TPAM (even if every metal ion only had one terpy, instead of a pair), the fastest decay is observed. It's unclear whether the lower initial λ_E (with respect to M:L = 0.75) is due to excessive end-caps in solution (resulting in shorter linear chains) or the ion-driven degradation; it could very well be both forces working simultaneously at this point. It is clear, however, that the rapid decay in this TPAM solution's λ_E following the first data point is due to chemical degradation and not equilibration. When mixing in metal at $c < c^*$, like we do in the current section, the absence of degradation effects would result in an initial rise in λ_E and then a stable plateau. That is, it would be energetically unfavorable for TPAM to first form long associative chains just to spontaneously break them up into smaller chains on their path towards equilibrium. The fact that M:L = 1.5 results in such a rapid λ_E decay further corroborates our Chapter 2 conclusion that metal ions catalyze the underlying degradation mechanism. This evidence for exacerbated decay complicates making a reliable connection to the equilibrium model presented in Figure 3.3, however we reiterate that the lower initial λ_E could also be due to the greater number of end-caps and a smaller amount of linkages (with the relative amount of metal-ligand (ML) species and ligand-metal-ligands (LML) being around 65% and 35%, respectively) that are expected at this M:L ratio.

3.2.4 TPAM's λ_E is driven by the largest megasupramolecular species

It's been previously established for standard PAM that the M_w distribution, namely the longest polymers in solution, has a significant effect on the exhibited λ_E , and we can draw the same conclusion for our TPAM solutions [23, 28]. We can compare our observations between TPAM's λ_E , M_w , and concentration in varied M:L ratio solutions to existing empirical studies on standard PAM to confirm this observation [28]. In Chapter 3 of Learsch's Thesis (reproduced with permission here as Figure 3.4) he shows the change in λ_E with respect to concentration for PAM at 2.34, 4.8,

and 6.7 MDa (PDIs 1.67, 1.6, and 1.34, respectively) in his Figure 3.2. The M_w averages (Table 3.1) created with 0.84 MDa TPAM at M:L ratio = 0.35 and 0.45 align well with Learsch's solutions, making for a convenient comparison. If we consider TPAM's full M_w distribution for M:L ratio = 0.35, over the total elution time including the unimer peak (19 to 26 minutes), at our total concentration (0.04 wt%), we get $M_w = 2.23$ MDa with PDI = 1.6. According to Learsch's data, this would result in a λ_E around 0.1 ms. However, we observe a λ_E around 0.5 ms. If we look at TPAM's megasupramolecular weight distribution alone (i.e. exclude the unimer peak) for M:L = 0.45 (elution time of 19 to 23 minutes), we see an average $M_w = 4.91$ MDa (PDI = 1.4) at lower concentration of 0.028 wt% (approximated by GPC calculated mass). Comparing this to Learsch's data, he shows $\lambda_E \approx 1.5$ ms for PAM at a comparable M_w and concentration, which is very similar to the λ_E of our TPAM solution at M:L = 0.45. This emphasizes that the highest M_w TPAM species are truly the ones driving the λ_E , and we speculate that the unimer species have a negligible contribution.

3.3 Unimer M_n affects TPAM's associative M_w distribution and λ_E

3.3.1 Experimental protocol and initial observations

We repeat the protocol from the M:L ratio sweep (Section 3.2.1, but this time we consider two new TPAM unimers with different molecular weights— $M_n = 710$ kDa and 1.0 MDa—also synthesized by Kim [29]. These molecular weights differ only marginally from 840 kDa, but we expect to see significant variation in λ_E with these different unimers. For one, larger unimers make it less entropically favorable for unimer rings to form [20]. Also, there is a compounded effect when the unimers form upwards of 10-mer chains, and it is understood that the largest molecules in the solution are primarily responsible for influencing λ_E . We test this hypothesis in this section. Note that we consider the number-averaged molecular weight (M_n)

of the unimers to calculate the average number of TPAM molecules in solution. This allows us to determine the amount of terpyridine present and calculate a more accurate M:L ratio (i.e. the ratio of moles of metal to moles of ligand). We also highlight Appendix A, where we indicate the appropriate uncertainty bounds to be $\pm 16\%$ when making comparisons between samples that were made from different starting solutions (such as our starting solutions with different unimer M_n).

TPAM's λ_E evolution over days since metal added and the M_w distributions for the different molecular weights resulted in similar trends (Figure 3.7 for 710 kDa, Figure 3.7 for 1.0 MDa). Increasing M:L leads to an increase in megasupramolecular M_w (surpassing our detectable limit). It also generally leads to an increase in maximum observed λ_E , although we see significantly more overlap within the uncertainty bounds on the λ_E versus day since metal added profiles for the new 0.71 and 1.0 MDa solutions. We still observe minimal λ_E decay for the "insufficient" M:L ratio solutions (M:L = 0.35 and 0.35) and a higher λ_E decay rate for the "excess" M:L solutions (M:L = 0.75 and 1.5)

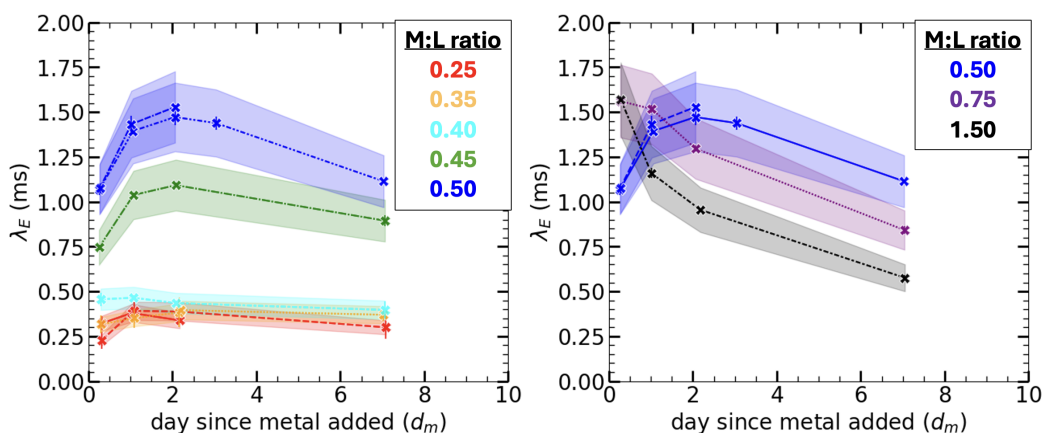


Figure 3.7: Evolution of λ_E for $M_{uni} = 0.71$ MDa unimers observed with respect to days since metal added (d_m) for M:L ratio = 0.25, 0.35, 0.4, 0.45, 0.5, 0.75, and 1.5. Error bars: $n_{drops} \geq 3$; Error bands: $13\% \pm$ uncertainty (see Appendix A). $M_{uni} = 0.71$ MDa; Solvent = unbuffered MilliQ; $c = 0.04$ wt%; Dilute \rightarrow Metal; $T_s = 22^\circ\text{C}$; Vial storage.

More interesting perhaps are the differences in TPAM's megasupramolecular weight

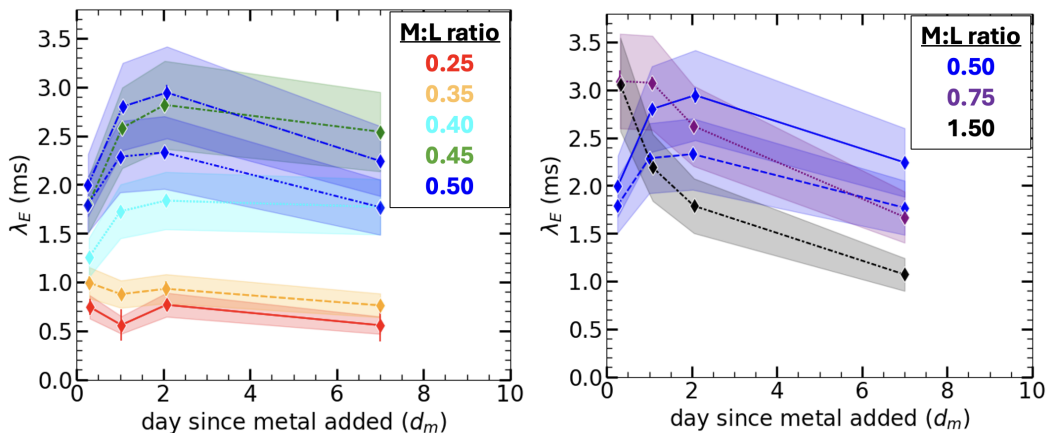


Figure 3.8: Evolution of λ_E for $M_{uni} = 1.0$ MDa unimers observed with respect to days since metal added (d_m) for M:L ratio = 0.25, 0.35, 0.4, 0.45, 0.5, 0.75, and 1.5. Error bars: $n_{drops} \geq 3$; Error bands: $13\% \pm$ uncertainty (see Appendix A).

$M_{uni} = 1.0$ MDa; Solvent = unbuffered MilliQ; $c = 0.04$ wt%; Dilute \rightarrow Metal; $T_s = 22^\circ\text{C}$; Vial storage.

averages and distributions caused by the varying unimer M_n and how that relates to our changing λ_E . In the following sections, we connect that to the different maximum observed λ_E 's and provide context by drawing a comparison to λ_E achieved in standard, non-associative PAM. We also relate the relative change in size and concentration of the high M_w TPAM species to the relative changes in λ_E and compare our observations to a previously proposed empirical model of the scaling relationships. Lastly, we aggregate the various unimer M_n data by representing them as their megasupramolecular weight averaged M_w versus λ_E , showing that the data does collapse on a log scale, providing further evidence for a power law contribution of high M_w species on λ_E .

3.3.2 TPAM unimer effects on M_w distribution

We assess the differences in molecular weight distribution by analyzing the megasupramolecules that form when one Ni(II) ion is added for every four terpys (M:L = 0.25) to a 0.04 wt% aqueous unimer solution. As discussed in previous sections, the GPC data is well below the upper limit for M:L = 0.25 for all three unimer lengths,

so this is the most reliable point of comparison. We see slightly less unimers as we go from 1.0, to 0.84, to 0.71 MDa, with a greater amount of the TPAMs linking to form longer megasupramolecules for the longer unimers (Figure 3.9). (Note the M_w distributions for 0.71, 0.84, and 1.0 MDa unimers' with no metal present is shown as a supplementary Figure 3.14). Table 3.2 provides a summary of the number average (M_n) and weight average (M_w) molecular weights for the higher molecular weight peaks, referred to as "Peak 2". Peak 2 occurs between approximately 19.5 and 22.5 minutes of elution time for the 1 MDa sample, and between 20 and 23 minutes for the 0.84 MDa and 0.71 MDa samples. It is important to note that these M_n and M_w values exclude the lower molecular weight peaks, designated as "Peak 1" (occurring between approximately 22.5 and 26 minutes for the 1 MDa sample, and 23 and 26.5 minutes for the 0.84 and 0.71 MDa samples). Additionally, the percent mass fraction for Peak 2 is provided, indicating the proportion of the total eluted molecules that fall within this peak relative to the entire sample mass. From this table, it is even more evident that both the M_n and M_w increase for Peak 2, but perhaps less predictably, so do the relative concentrations of megasupramolecules (wt%) that fall within that larger molecular weight peak.

Unimer M_n	M:L	M_n [MDa]	M_w [MDa]	Mass fraction (%)
0.71	0.25	1.87	2.16	43.5
0.84	0.25	2.20	2.60	45.7
1.00	0.25	2.71	3.20	51.2

Table 3.2: Summary of molecular weight and mass fraction data for M:L ratio = 0.25 for the various unimer M_n . The number and weight average molecular weights are given for the higher molecular weight peaks, or "Peak 2" (between approximately 19 and 22.5 minute elution time for 1 MDa, and 20 and 23 for 0.84 and 0.71). The percent mass fraction for Peak 2 is also shown, which quantifies the amount of eluted molecules within Peak 2 compared to the calculated mass for the total eluted sample.

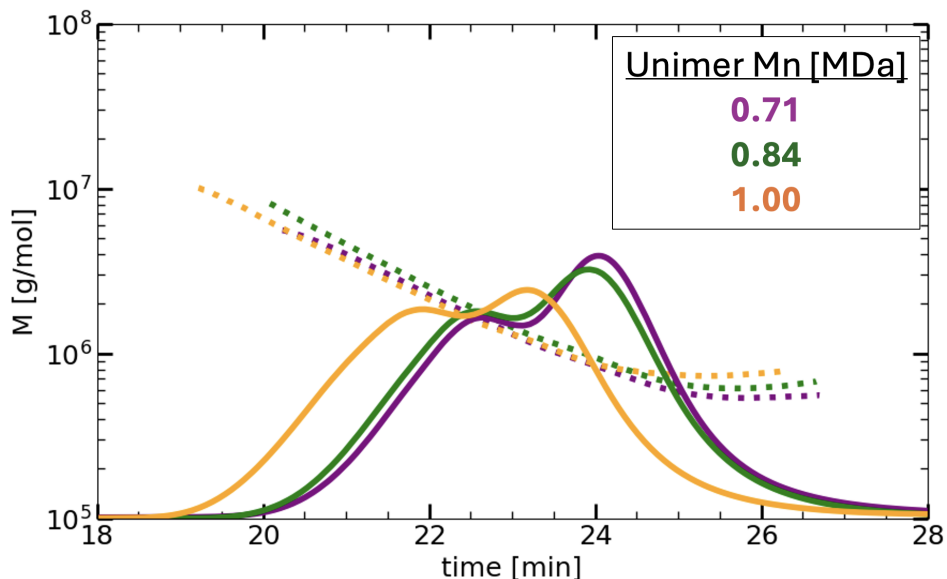


Figure 3.9: GPC traces for three different unimer lengths (0.71, 0.84, and 1.0 MDa) with one Ni(II) ion added for every four terpys ($M:L = 0.25$).

Solvent = unbuffered MilliQ; $c = 0.04$ wt%; Dilute \rightarrow Metal; $T_s = 22^\circ\text{C}$; Vial storage.

3.3.3 TPAM's achievable λ_E and comparison to standard PAM

We compare the difference in the change in TPAM's maximum λ_E s for TPAM unimers of 0.71, 0.84, and 1.0 MDa with NiCl_2 added ranging from $M:L = 0.25$, 0.35, 0.4, 0.45, 0.5, to 0.75 (Figure 3.10). Note that in the present analysis, TPAM's maximum λ_E values for each $M:L$ ratio for each unimer M_n are reported. We represent the data this way, rather than showing the λ_E for a specific day since metal was added due to the differing rates of equilibrium and decay rates for each $M:L$ ratio. Showing the maximum for each case is our best approximation to assessing the values at equilibrium for each unique case. $M:L = 1.5$ is not included in this comparison due to its evident early and especially quick λ_E decay for all unimer lengths.

This comparison provides some evidence towards our hypothesis that there is a correlation between the TPAM unimer M_n with its maximum λ_E , but the uncertainty bands on λ_E encourage us to exercise caution in our direct comparison. However, the similarity in curve shapes is intriguing in that we see a similar change in λ_E as

M:L is increased for each unimer. The results also raise the question if the M:L ratios for the 1.0 MDa TPAM are systematically slightly higher than what we aimed to achieve; this would push the 1.0 MDa vs M:L curve towards the right, creating more overlap with the 0.84 MDa unimer. We sought to account for this possibility by doing a tight sweep over the M:L ratios, to ensure that the general trend for each M_n was clearly observable, but we acknowledge that it has a greater influence when making comparisons between the different unimer M_n , especially around the highly sensitive stoichiometric equivalent region of M:L = 0.5. Due to the direct calculation of M:L ratio based on unimer M_n , even a 5% discrepancy in M_n could lead to the same uncertainty on M:L ratio. This would also explain the high jump from M:L = 0.35 to 0.4, which is not observed until M:L = 0.4 to 0.45 for the other two unimers.

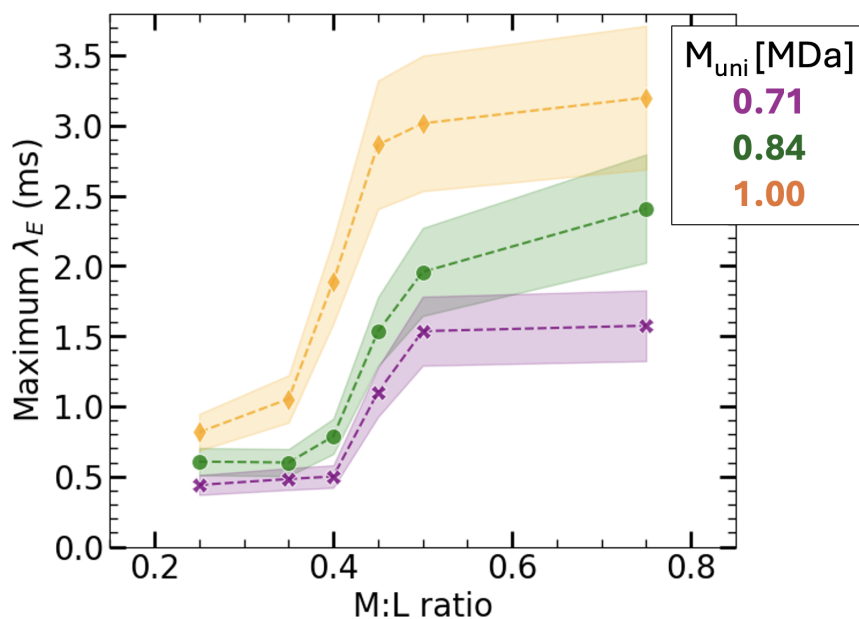


Figure 3.10: Maximum λ_E values observed for each M:L ratio for each unimer M_n . Error bars: $n_{drops} \geq 3$; Error bands: $16\% \pm$ uncertainty (see Appendix A). Solvent = unbuffered MilliQ; $c = 0.04$ wt%; Dilute \rightarrow Metal; $T_s = 22^\circ\text{C}$; Vial storage.

To gain an appreciation for TPAM's achievable λ_E , we can compare to existing empirical results on standard PAM. Soetrismo et al. (2023) reports on the effect

that different concentration regimes of various M_w PAM has on λ_E . To make a direct comparison between their results with the results shown in this Chapter, they specifically show that 1 MDa PAM at 820 wppm results in a λ_E of 3.1 ms [23]. With TPAM of the same unimer M_w , we are able to achieve the same $\lambda_E \approx 3$ ms with less than half the concentration (400 ppm) by adding 0.45 to 0.75 Ni(II) ions per ligand (M:L = 0.45 to 0.75, a wide range, even given potential uncertainties). This indicates that not only does TPAM have a better chance at resisting chain scission with its reversible associations, but it can also achieve similar extensional rheological properties with less polymer concentration.

3.3.4 Comparing current scaling observations to an existing empirical model

We can relate our measured λ_E to its respective M_w and concentration for the various unimer M_n , which allows us to make comparisons to Learsch's proposed scaling relation, $\lambda_E \sim M_w^{3.6} c^{0.77}$ (Equation 3.1.3) [28]. Intriguingly, the percent changes in the M_w of Peak 2 for 0.71 and 1.0 MDa compared to 0.84 MDa are -15% and +23% (Table 3.2), which is, respectively, exactly the same and slightly more than the difference in the unimer M_n 's (-15% for 0.71 MDa and +19% for 1.0 MDa). Considering Learsch's relation, this relative change in M_w would give an expected change of -47% and 104% for the resulting λ_E . These values are significantly higher than the difference measured in our λ_E for all three unimers at M:L = 0.25 on d_m when (GPC was taken) – 0.48 ms for 0.84 KDa, compared to 0.56 ms for 1.0 MDa (an 18% increase) and 0.38 ms for 0.71 MDa (a 20% decrease). However, Learsch's scaling relationship was only determined from a limited range of M_w (2.34, 4.8, and 6.7 MDa) and c (0.045 to 1 wt%, 0.02 to 1 wt%, and 0.0025 to 1 wt%, respectively, for each M_w) for covalent PAM. For our M:L = 0.25 solutions at Peak 2, the megasupramolecular M_w falls near or below $M_w = 2.34$, and the concentrations (wt%) fall below the values tested by Learsch

for this M_w . Considering this, Learsch's relation likely cannot be extended to our particular case. This justifies establishing a clear boundary on the applicability of Learsch's relation. It could also indicate some fundamental differences in the megasupramolecular TPAM solutions and standard covalent PAM. Now that we have built up a range of various M_w averages and respective λ_E 's, we can assess whether or not we can observe a trend in our own data.

3.4 TPAM megasupramolecular M_w and λ_E show an exponential power law relationship

We can bypass the specific dependencies of M:L ratio and M_n , and instead look directly at the effect of megasupramolecular M_w average on λ_E to see if the data collapses into one cohesive trend. We see that when M_w and λ_E are both plotted on a logarithmic scale, the data from all three unimer lengths and our various M:L ratios do generally collapse (Figure 3.11).

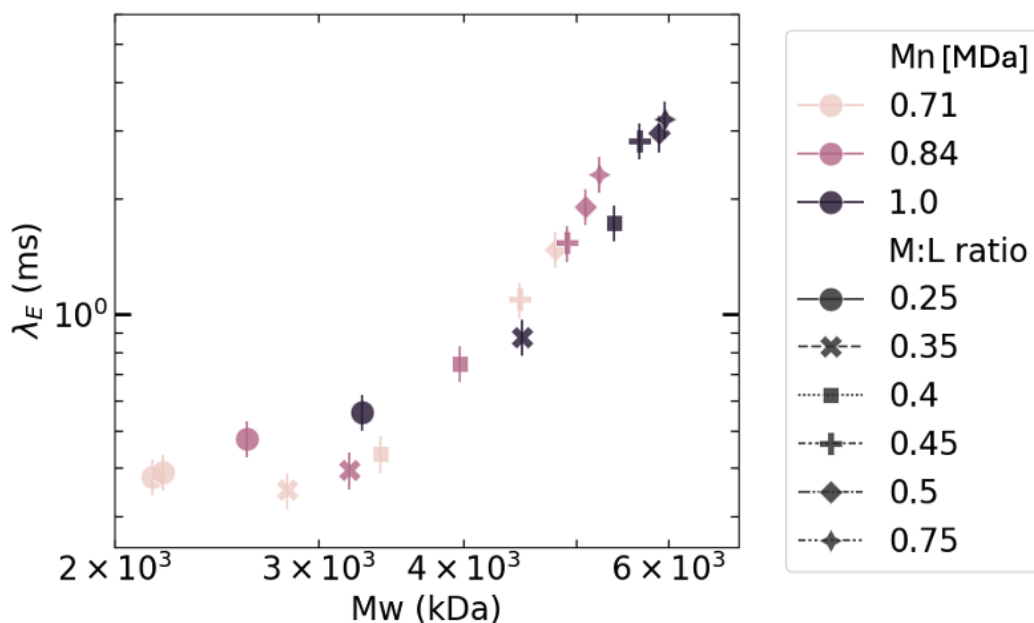


Figure 3.11: λ_E versus M_w for each unimer M_n over their sweep of M:L = 0.25, 0.35, 0.4, 0.45, 0.5, and 0.75.

The appearance of a linear trend here suggests a potential underlying exponential

power law, as suggested by previous studies with respect to c^*/c [23]. The legitimacy of fitting a power law to this data is currently under investigation, as we consider the influence of pervaded volume on c^*/c that might influence the apparent divergence that occurs < 4 MDa.

3.5 Conclusions and Future Work

In this chapter, we explored the impact of varying the metal-to-ligand (M:L) ratio on the associative molecular weight (M_w) distribution and relaxation time (λ_E) of TPAM solutions. We observed that increasing the M:L ratio led to the formation of larger TPAM megasupramolecules (Figure 3.5). At lower M:L ratios (M:L = 0.25), the distribution showed primarily unimers and dimers, while higher ratios (M:L \geq 0.35) resulted in the formation of multi-mers of significantly larger supramolecular structures. Notably, at M:L \geq 0.45, the M_w of the megasupramolecular species approached and even surpassed the detection limit of our GPC, indicating the formation of stable assemblies extending beyond 10 MDa.

The relaxation time (λ_E) of TPAM solutions increased with the M:L ratio, up to a point where an excessive amount of metal ions resulted in a quicker λ_E decay. This suggests that while higher M:L ratios facilitate the formation of larger and more complex structures earlier on, they also introduce factors that promote degradation which were identified in Chapter 2. By comparing our results with existing studies on standard PAM, we confirmed that the largest TPAM species primarily drive the λ_E . Our analysis demonstrated that the high M_w species in TPAM solutions have a significant impact on the relaxation time, and the unimer species' contribution is minimal. We extended our investigation to include TPAM unimers of different molecular weights ($M_n = 710$ kDa and 1.0 MDa). The results showed that unimer M_n influences both the M_w distribution and the λ_E . Larger unimers generally formed longer and more concentrated megasupramolecular structures, leading to higher λ_E

values overall, but note that at points, the significance of the difference falls within the range of solution variability (Appendix A). However, increasing unimer length may introduce a trade-off of a backbone more susceptible to permanent scission.

In summary, our study demonstrates that the associative molecular weight distribution and relaxation time of TPAM solutions can be tuned by varying the M:L ratio and the unimer molecular weight. The M_w can vary to include dimers all the way up to 12-mers and beyond, while the λ_E can span 0.25 to 3.5 ms, inclusive of our uncertainty bounds, for the conditions we explored. These findings provide valuable insights into the design and optimization of TPAM-based systems for applications requiring specific rheological properties. Future work should explore the use of advanced GPC columns with higher M_w detection limits or other analytical tools such as Flow Field Fractionation [30] to gain a more comprehensive understanding of these complex supramolecular systems. We have also adapted the end-associative polymer model framework by Ameri [20] in collaboration with Dr. Gianfranco Canales and are currently investigating how it could provide insight on the underlying megasupramolecular distribution of linear and ring species.

In the following chapter, we explore how different mixing protocols can influence the topology and extensional behavior of TPAM supramolecules to see if we can further expand their capabilities and potential for diverse applications.

3.6 Supplementary Figures

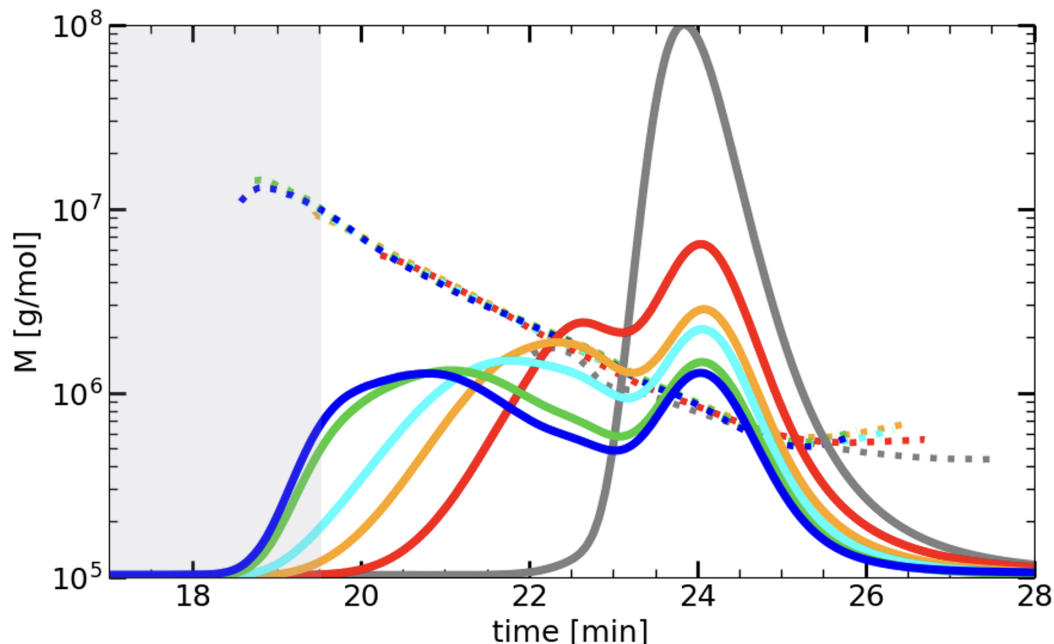


Figure 3.12: M_w distributions collected with GPC for 0.71 MDa TPAM with NiCl_2 added such that the M:L ratio = 0.25, 0.35, 0.4, 0.45, 0.5, and 0.75. GPC profiles for M:L = 0.25, 0.35, 0.4, 0.45, and 0.5, taken at day since metal added (d_m) = 1, 1, 1, 2, and 2, respectively. The dotted lines correspond to the y-axis M [g/mol], which shows the molecular weight eluting at the given time on the x-axis. The solid lines represent the relative concentrations of molecules eluting at that time at the corresponding molecular weight. The grey box represents the upper limit of the GPC detection (10^7 MDa).

Solvent = unbuffered MilliQ; $c = 0.04$ wt%; Dilute \rightarrow Metal; Vial storage.

References

- [1] Evelyne Van Ruymbeke. “Dynamics of metallo-supramolecular networks: the influence of their building blocks architecture”. JoR - RA - JNNFM seminar, Apr. 19, 2023.
- [2] Ana C. Mendes et al. “Self-assembly in nature: using the principles of nature to create complex nanobiomaterials”. In: *WIREs Nanomedicine and Nanobiotechnology* 5.6 (Nov. 2013), pp. 582–612. ISSN: 1939-5116, 1939-0041. DOI: [10.1002/wnan.1238](https://doi.org/10.1002/wnan.1238).
- [3] Ralf Knapp, Andreas Schott, and Matthias Rehahn. “A Novel Synthetic Strategy toward Soluble, Well-Defined Ruthenium(II) Coordination Polymers”. In: *Macromolecules* 29.1 (Jan. 1, 1996), pp. 478–480. ISSN: 0024-9297, 1520-5835. DOI: [10.1021/ma946520u](https://doi.org/10.1021/ma946520u).
- [4] Stefan Schmatloch et al. “Soluble High-Molecular-Mass Poly(ethylene oxide)s via Self-Organization”. In: *Macromolecules* 36.26 (Dec. 1, 2003), pp. 9943–9949. ISSN: 0024-9297, 1520-5835. DOI: [10.1021/ma0350359](https://doi.org/10.1021/ma0350359).

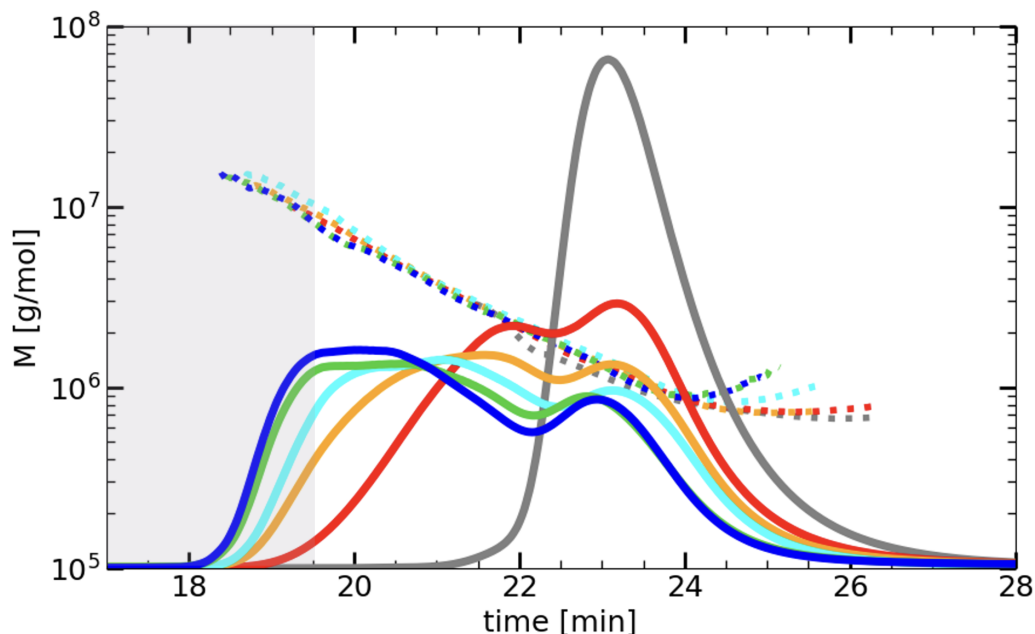


Figure 3.13: M_w distributions collected with GPC for 1.0 MDa TPAM with NiCl_2 added such that the M:L ratio = 0.25, 0.35, 0.4, 0.45, 0.5, and 0.75. GPC profiles for M:L = 0.25, 0.35, 0.4, 0.45, and 0.5, taken at day since metal added (d_m) = 1, 1, 1, 2, and 2, respectively. The dotted lines correspond to the y-axis M [g/mol], which shows the molecular weight eluting at the given time on the x-axis. The solid lines represent the relative concentrations of molecules eluting at that time at the corresponding molecular weight. The grey box represents the upper limit of the GPC detection (10^7 MDa).

Solvent = unbuffered MilliQ; $c = 0.04$ wt%; Dilute \rightarrow Metal; Vial storage.

- [5] Wayne C. Yount, David M. Loveless, and Stephen L. Craig. “Strong Means Slow: Dynamic Contributions to the Bulk Mechanical Properties of Supramolecular Networks”. In: *Angewandte Chemie International Edition* 44.18 (Apr. 29, 2005), pp. 2746–2748. ISSN: 1433-7851, 1521-3773. DOI: [10.1002/anie.200500026](https://doi.org/10.1002/anie.200500026).
- [6] David M. Loveless, Sung Lan Jeon, and Stephen L. Craig. “Rational Control of Viscoelastic Properties in Multicomponent Associative Polymer Networks”. In: *Macromolecules* 38.24 (Nov. 1, 2005), pp. 10171–10177. ISSN: 0024-9297, 1520-5835. DOI: [10.1021/ma0518611](https://doi.org/10.1021/ma0518611).
- [7] Jérémy Brassinne, Charles-André Fustin, and Jean-François Gohy. “Polymer Gels Constructed Through Metal–Ligand Coordination”. In: *Journal of Inorganic and Organometallic Polymers and Materials* 23.1 (Jan. 2013), pp. 24–40. ISSN: 1574-1443, 1574-1451. DOI: [10.1007/s10904-012-9757-x](https://doi.org/10.1007/s10904-012-9757-x).
- [8] Jérémy Brassinne, Jean-François Gohy, and Charles-André Fustin. “Orthogonal Control of the Dynamics of Supramolecular Gels from Heterotelechelic

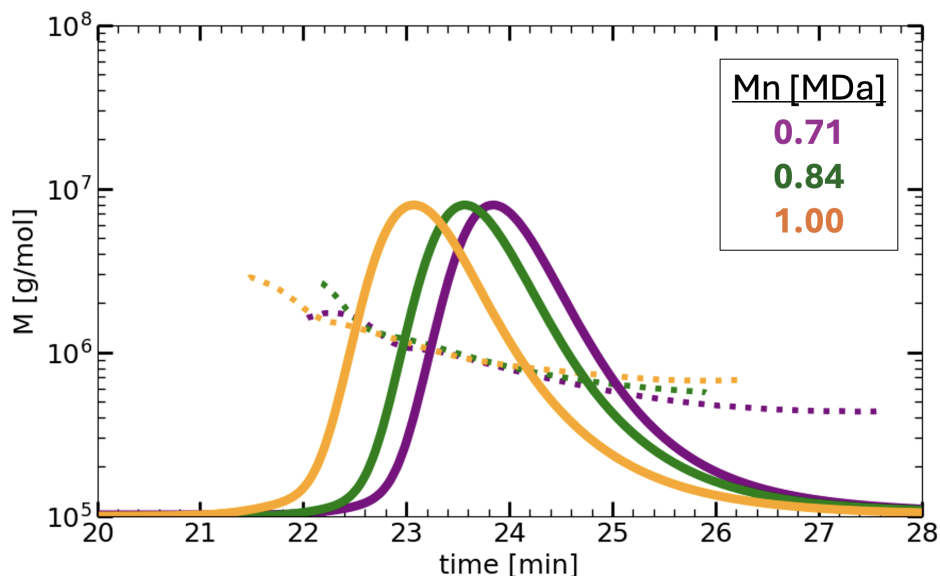


Figure 3.14: GPC traces for solutions of 0.04wt% aqueous TPAM for three different unimer lengths (0.71, 0.84, and 1.0 MDa).

- Associating Polymers”. In: *ACS Macro Letters* 5.12 (Dec. 20, 2016), pp. 1364–1368. ISSN: 2161-1653, 2161-1653. DOI: [10.1021/acsmacrolett.6b00831](https://doi.org/10.1021/acsmacrolett.6b00831).
- [9] Scott C. Grindy, Martin Lenz, and Niels Holten-Andersen. “Engineering Elasticity and Relaxation Time in Metal-Coordinate Cross-Linked Hydrogels”. In: *Macromolecules* 49.21 (Nov. 8, 2016), pp. 8306–8312. ISSN: 0024-9297, 1520-5835. DOI: [10.1021/acs.macromol.6b01523](https://doi.org/10.1021/acs.macromol.6b01523).
- [10] Davoud Mozhdehi et al. “Tuning Dynamic Mechanical Response in Metallopolymer Networks through Simultaneous Control of Structural and Temporal Properties of the Networks”. In: *Macromolecules* 49.17 (Sept. 13, 2016), pp. 6310–6321. ISSN: 0024-9297, 1520-5835. DOI: [10.1021/acs.macromol.6b01626](https://doi.org/10.1021/acs.macromol.6b01626).
- [11] Hui Yang et al. “Tunable Interpenetrating Polymer Network Hydrogels Based on Dynamic Covalent Bonds and Metal–Ligand Bonds”. In: *Macromolecules* 53.16 (Aug. 25, 2020), pp. 6956–6967. ISSN: 0024-9297, 1520-5835. DOI: [10.1021/acs.macromol.0c00494](https://doi.org/10.1021/acs.macromol.0c00494).
- [12] Mostafa Ahmadi and Sebastian Seiffert. “Coordination Geometry Preference Regulates the Structure and Dynamics of Metallo-Supramolecular Polymer Networks”. In: *Macromolecules* 54.3 (Feb. 9, 2021), pp. 1388–1400. ISSN: 0024-9297, 1520-5835. DOI: [10.1021/acs.macromol.0c02524](https://doi.org/10.1021/acs.macromol.0c02524).
- [13] Yanzhao Li et al. “Dynamics of entangled metallosupramolecular polymer networks combining stickers with different lifetimes”. In: *Journal of Rheology* 66.6 (Nov. 2022), pp. 1203–1220. ISSN: 0148-6055, 1520-8516. DOI: [10.1122/8.0000418](https://doi.org/10.1122/8.0000418).

- [14] Christina Pyromali et al. “Nonlinear shear rheology of single and double dynamics metal-ligand networks”. In: *Journal of Rheology* 66.6 (Nov. 2022), pp. 1223–1235. ISSN: 0148-6055, 1520-8516. DOI: [10.1122/8.0000429](https://doi.org/10.1122/8.0000429).
- [15] Ming-Hsin Wei et al. “Megasupramolecules for safer, cleaner fuel by end association of long telechelic polymers”. In: *Science* 350.6256 (Oct. 2, 2015), pp. 72–75. ISSN: 0036-8075, 1095-9203. DOI: [10.1126/science.aab0642](https://doi.org/10.1126/science.aab0642).
- [16] Robert M. Smith and Arthur E. Martell. *Critical Stability Constants*. Boston, MA: Springer US, 1989. ISBN: 978-1-4615-6766-0 978-1-4615-6764-6. DOI: [10.1007/978-1-4615-6764-6](https://doi.org/10.1007/978-1-4615-6764-6).
- [17] Reece W. Lewis et al. “Ultra-high molecular weight linear coordination polymers with terpyridine ligands”. In: *Chemical Science* 10.24 (2019), pp. 6174–6183. ISSN: 2041-6520, 2041-6539. DOI: [10.1039/C9SC01115C](https://doi.org/10.1039/C9SC01115C).
- [18] P.Y. Hou. “Oxidation of Metals and Alloys”. In: *Shreir’s Corrosion* 1 (Dec. 2010), pp. 195–239. DOI: [10.1016/B978-044452787-5.00013-5](https://doi.org/10.1016/B978-044452787-5.00013-5).
- [19] Bas G. G. Lohmeijer and Ulrich S. Schubert. “Water-Soluble Building Blocks for Terpyridine-Containing Supramolecular Polymers: Synthesis, Complexation, and pH Stability Studies of Poly(ethylene oxide) Moieties”. In: *Macromolecular Chemistry and Physics* 204.8 (May 2003), pp. 1072–1078. ISSN: 1022-1352, 1521-3935. DOI: [10.1002/macp.200390078](https://doi.org/10.1002/macp.200390078).
- [20] Ralph Leonard Ameri David. “Associative Polymers as Antimisting Agents and Other Functional Materials via Thiol-ene Coupling”. Medium: PDF Version Number: Final. PhD thesis. California Institute of Technology, 2008. DOI: [10.7907/9AHR-A213](https://doi.org/10.7907/9AHR-A213).
- [21] Michael Rubinstein and Ralph H. Colby. *Polymer physics*. Oxford ; New York: Oxford University Press, 2003. 440 pp. ISBN: 978-0-19-852059-7.
- [22] Jelena Dinic and Vivek Sharma. “Flexibility, Extensibility, and Ratio of Kuhn Length to Packing Length Govern the Pinching Dynamics, Coil-Stretch Transition, and Rheology of Polymer Solutions”. In: *Macromolecules* 53.12 (June 23, 2020), pp. 4821–4835. ISSN: 0024-9297, 1520-5835. DOI: [10.1021/acs.macromol.0c00076](https://doi.org/10.1021/acs.macromol.0c00076).
- [23] Diego D. Soetrisno et al. “Concentration Regimes for Extensional Relaxation Times of Unentangled Polymer Solutions”. In: *Macromolecules* 56.13 (July 11, 2023), pp. 4919–4928. ISSN: 0024-9297, 1520-5835. DOI: [10.1021/acs.macromol.3c00097](https://doi.org/10.1021/acs.macromol.3c00097).
- [24] R. Prabhakar et al. “Influence of stretching induced self-concentration and self-dilution on coil-stretch hysteresis and capillary thinning of unentangled polymer solutions”. In: *Journal of Rheology* 60.3 (May 2016), pp. 345–366. ISSN: 0148-6055. DOI: [10.1122/1.4942792](https://doi.org/10.1122/1.4942792). eprint: https://pubs.aip.org/sor/jor/article-pdf/60/3/345/15803657/345_1_online.pdf.

- [25] V. Tirtaatmadja, G. H. McKinley, and J. J. Cooper-White. “Drop formation and breakup of low viscosity elastic fluids: Effects of molecular weight and concentration”. In: *Physics of Fluids* 18.4 (Apr. 2006), p. 043101. ISSN: 1070-6631. DOI: [10.1063/1.2190469](https://doi.org/10.1063/1.2190469). eprint: https://pubs.aip.org/aip/pof/article-pdf/doi/10.1063/1.2190469/13662176/043101\1_online.pdf.
- [26] Jelena Dinic et al. “Extensional Relaxation Times of Dilute, Aqueous Polymer Solutions”. In: *ACS Macro Letters* 4.7 (July 21, 2015), pp. 804–808. ISSN: 2161-1653, 2161-1653. DOI: [10.1021/acsmacrolett.5b00393](https://doi.org/10.1021/acsmacrolett.5b00393).
- [27] Jelena Dinic, Leidy Nallely Jimenez, and Vivek Sharma. “Pinch-off dynamics and dripping-onto-substrate (DoS) rheometry of complex fluids”. In: *Lab on a Chip* 17.3 (2017), pp. 460–473. ISSN: 1473-0197, 1473-0189. DOI: [10.1039/C6LC01155A](https://doi.org/10.1039/C6LC01155A).
- [28] Robert Learsch. “Droplet control in aqueous and hydrocarbon fluids: Long, end-associative polymers dictate fluid behavior under elongational flows”. PhD thesis. Caltech, Oct. 20, 2022.
- [29] Hojin Kim. “New Long End-Associative Polymers for Mist Control in I. Aqueous Solutions and II. Hydrocarbon Solvents”. Medium: PDF Version Number: Final. PhD thesis. California Institute of Technology, Aug. 26, 2022. DOI: [10.7907/Rsx9-QT39](https://doi.org/10.7907/Rsx9-QT39).
- [30] J. Calvin Giddings. “Field-Flow Fractionation: Analysis of Macromolecular, Colloidal, and Particulate Materials”. In: *Science* 260.5113 (June 4, 1993), pp. 1456–1465. ISSN: 0036-8075, 1095-9203. DOI: [10.1126/science.8502990](https://doi.org/10.1126/science.8502990).

*Chapter 4***EXPANDING TPAM MEGASUPRAMOLECULE TOPOLOGY AND BEHAVIOR BY VARYING CONCENTRATION WHEN METAL IS ADDED****4.1 Introduction: Changing concentration when metal is added changes the topology and behavior**

The overarching goal of this chapter is to expand the range of useful fluid properties that can be achieved with TPAM and to gain insight on the distribution of megasupramolecules that deliver technologically valuable properties. We approach this by exploring the possibility that larger megasupramolecules can be produced from a given unimer by adding metal when unimer concentration is relatively high (compared to c^* and to the dilute concentration during use), yet low enough to be a tractable, pourable fluid instead of a gel. It is physically reasonable to expect that the topology and behavioral properties depend on the concentration at which metal is added to the solution before it is diluted to its target concentration. Lewis et al. (2019) touches upon the difference between adding metal at starting concentrations of 2 and 10 times the final dissolved concentration in their Supplementary Information Figure S11 [1]. They show a slight change in M_w (300 vs 350 kDa), but do not go into depth to describe the phenomena or connect it to $c < c^*$. There is seemingly a lack of work that explicitly investigates the effect of changing the concentration after the metal ions were added and the initial associations formed, with the exception of preliminary evidence of its significance presented in the theses of Hojin Kim and Rob Learsch [2, 3].

Kim showed that the size of the megasupramolecules increases with unimer concentration at the time metal is added (Fig 4.1, reproduced from [2]). Kim also showed

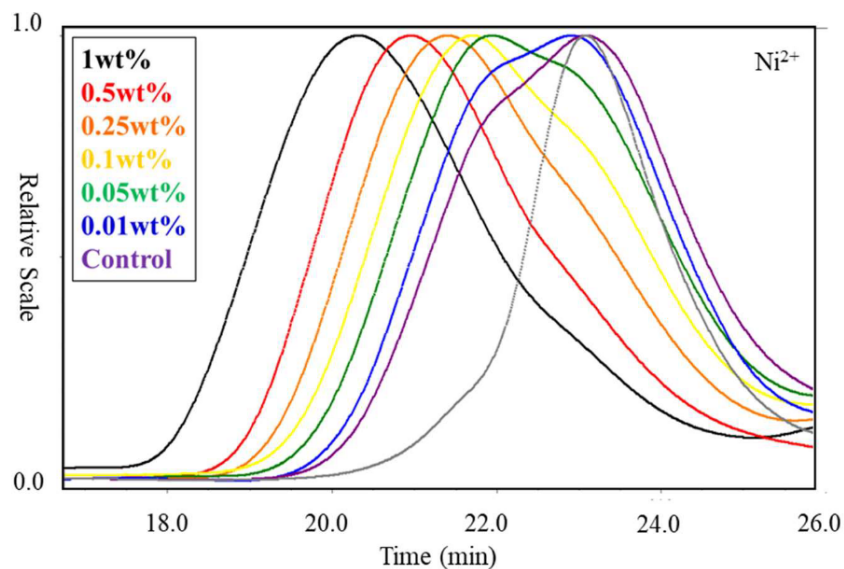


Figure 4.1: GPC traces for TPAM with metal added at different concentrations (ranging 0.01 to 1 wt%) before the final dissolution to 0.01 wt%, normalized to the maximum signal height. Unimer TPAM $M_n = 0.82$ MDa in un-buffered MilliQ water with Ni(II) added such that M:L = 0.5. Data was taken by Kim and presented as Figure 2.16 in his thesis, reproduced with permission [2].

that the megasupramolecular mass decreases drastically over time, from an initial 3.5 MDa immediately after metal was added and then dissolved, to 1 MDa 6 days later. At the time of Kim's study, it was thought that the highest molar mass species of supramolecules were represented in the GPC measurement and that the decrease in supramolecular molar mass over 6 days was due to end-group exchange. While the results remain compelling, a deeper understanding of TPAM chemical decay was lacking at the time, and the influence of filtration was not considered. TPAM chemical decay is characterized in Chapter 2, and we address the impact of filtration in later sections of this chapter. As we will reveal in the current chapter, these factors are highly influential in what we can observe and how we should approach explaining what we see.

Learsch briefly expands on the influence of adding metal to a higher concentration prior to dilution in the supplementary information section of Chapter 4 in his thesis, covering preliminary TPAM extensional rheology exploration [3]. For the entirety of

his study preceding this supplementary information, he added metal to the solution when it was already at its diluted target concentration. He eventually tests the case where one solution had metal added at its target concentration (0.01 wt%), and another was diluted only after metal was added at a higher concentration (0.1 wt%). He shows that the solution where metal was added to the higher concentration prior to dilution exhibits a higher λ_E (0.12 ms vs 0.03 ms) indicating a significant change in λ_E caused by changing the concentration when metal was added. Even though Learsch does not explicitly connect the λ_E data from this experiment to molecular structure with GPC, his suggestion that the increase in λ_E is due to "increased ease of association with higher concentrations of the terpyridine end groups" is reasonable. His assessment is supplemented by our observation of the finite amount of time it takes for one TPAM at dilute concentrations ($c < c^*$) to encounter another TPAM in order to form megasupramolecular chains, described in Chapters 2 and 3. We posit this would drastically change if the metal was added at semi-dilute conditions where $c > c^*$, because the terpyridine on one end of a TPAM would now be surrounded by the terpyridine end-groups from a multitude of other TPAM unimers (Figure 4.2).

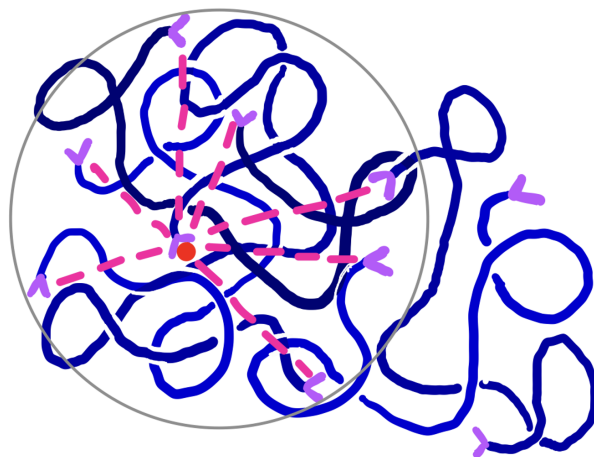


Figure 4.2: Sketch of TPAM at $c/c^* \approx 3.5$, which results in approximately 7 terpyridines present within the pervaded volume of one TPAM.

Given our interest in exploring the range of TPAM's behavioral and molecular

capabilities, it is necessary that we revisit the influence of adding metal to a higher concentration prior to dilution, with some additional key factors in mind. We must explicitly integrate the study of solution behavior (λ_E) with molecular changes (M_w distribution). We use conditions that delay chemical degradation and do not filter our solutions before running GPC (running samples through a 0.45% μm syringe filter is standard practice to avoid particulates clogging the GPC, but our samples are pure enough that this was not an issue). We consider parallel processes of ligand exchange and chemical degradation, remaining cognizant of ambiguity regarding the equilibration of megasupramolecules. We choose to use a starting concentration of 1 wt%, which is greater than c^* ($c/c^* \approx 3.5$), but still tractable in terms of pouring and mixing. Hereinafter, the protocol where we add metal to 1 wt% before dissolving to 0.04 wt% is denoted "Metal \rightarrow Dilute", whereas the previous protocol (in Chapters 2 and 3) where we add metal to the final 0.04 wt% solution is denoted "Dilute \rightarrow Metal". Hereafter, the difference in protocols is referred to as changing the "order of operations", because we are essentially just altering the order of preparation steps we take to prepare a solution with the same components.

We start by looking at the magnitude of λ_E with various M:L ratios achieved by the Metal \rightarrow Dilute protocol, and draw comparisons to the trends observed in the previous Dilute \rightarrow Metal protocol. Then, we compare the achievable λ_E for both protocols and connect that to changes in the megasupramolecular M_w distribution and topology. We reveal intriguing changes to the size and shape of the megasupramolecules created with the Metal \rightarrow Dilute protocol and use filtration fractionation to gain insight on their size, ultimately resulting in an ongoing collaboration with charge detection mass spectrometry for a more comprehensive look. We then evaluate the molecules' potential as a chain resistant, turbulent drag reducing agent.

4.1.1 Experimental protocol

We modified the original solution protocol (sketched in Figure 2.9) to investigate the effect of order of operations by adding metal to the higher concentration stock solution before the final dissolution to the target concentration (sketched in Figure 4.3). We started, as usual, by dissolving TPAM at 1 wt% ($c/c^* \approx 3.5$) in unbuffered MilliQ water and gently shaking it on a Wrist Action Shaker for 3 days until complete dissolution. Small volumes (on the order of $10 \mu\text{L}$) of a stock solution of 0.5 mM of NiCl_2 was pipetted to aliquots of these starting solutions and rolled for 2.5 to 3 hours at 10 rpm. After 2.5 to 3 hours of rolling, MilliQ water was added to reach a final target concentration of 0.04 wt% ($c/c^* \approx 0.14$).

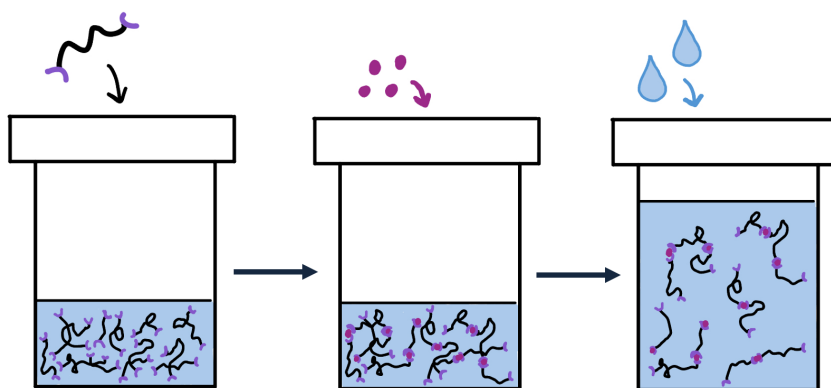


Figure 4.3: Sketch of the adapted Metal \rightarrow Dilute protocol to test effect of order of operations. First, TPAM was dissolved at 1 wt% in unbuffered MilliQ water. Then, aliquots of these solutions were mixed with NiCl_2 and rolled at 10 rpm for 2.5 to 3 hours. After rolling, MilliQ water was added to achieve a final concentration of 0.04 wt%.

4.2 Order of operations changes extensional behavior

4.2.1 DoSER curves immediately reveal a stark contrast in extensional behavior for different order of operations

A dramatic difference in protocols was first evident from the raw DoSER data, which shows the change in normalized filament diameter over time (Figure 4.4). We look closer at the different DoSER profiles that result from M:L ratio = 0.5 and 1.5

prepared with the different order of operations. First, the Metal \rightarrow Dilute protocol results in a much slower decrease in filament diameter and pinch-off for both M:L represented here. Also, from this perspective, the variation in extensional behavior that results from altering M:L in the Dilute \rightarrow Metal protocol appears to be minor compared to the substantially slower change in filament diameter seen for Metal \rightarrow Dilute. We take a closer look at the comparison between equilibrium, stability, and M:L ratio in the following sections.

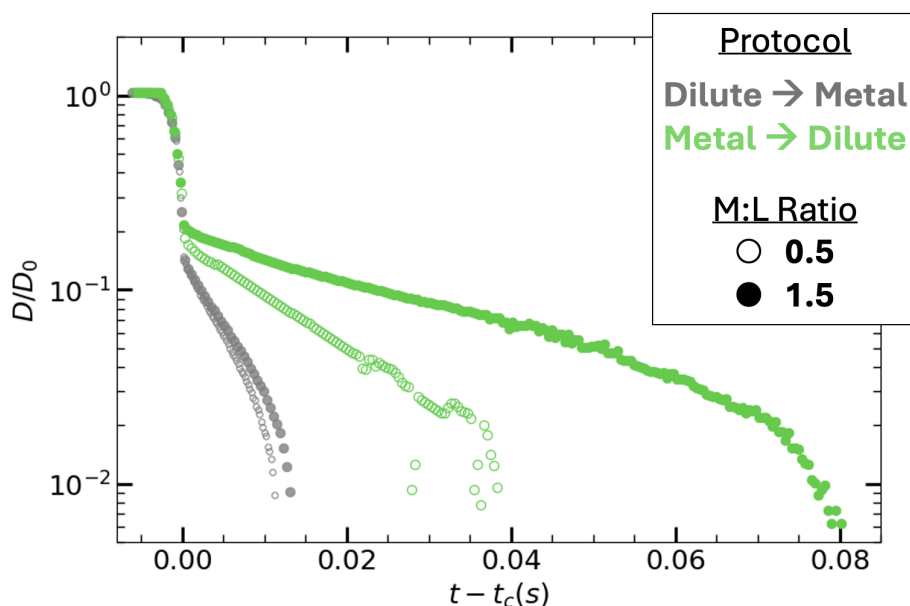


Figure 4.4: DoSER results for the filament diameter changing over time for solutions prepared with Metal \rightarrow Dilute protocol versus Dilute \rightarrow Metal protocol, and M:L = 0.5 and 1.5.

$M_{uni} = 0.84$ MDa; Solvent = unbuffered MilliQ; $c = 0.04$ wt%; $T_s = 22^\circ\text{C}$; Vial storage.

4.2.2 Order of operations affects maximum λ_E and the influence of M:L ratio

For the Metal \rightarrow Dilute protocol, we see an increase in λ_E with increasing M:L ratio, up to a point (Figure 4.5). This increase in λ_E at M:L ratios greater than the stoichiometric equivalent was also observed in the Dilute \rightarrow Metal protocol, except here, the λ_E values are significantly higher. For instance, for Dilute \rightarrow Metal protocol, 0.84 MDa TPAM unimers at 0.04 wt% with M:L = 0.5, we observed

relaxation times ranging from $\lambda_E = 1.5$ to 2 ms (Figure 3.6). When we switch to the Metal \rightarrow Dilute, the λ_E reaches upwards to 6 ms (three times higher than the previous protocol!). We also emphasize that the λ_E for this M:L = 0.5 is far more stable than M:L that exceeds the stoichiometric equivalent, even if higher M:L does result in an initially higher λ_E . This is indicated by the λ_E values all remaining around 5-6 ms over the range of $d_m = 0.25$ through 6, while the higher M:L ratio corresponded to faster drops in λ_E .

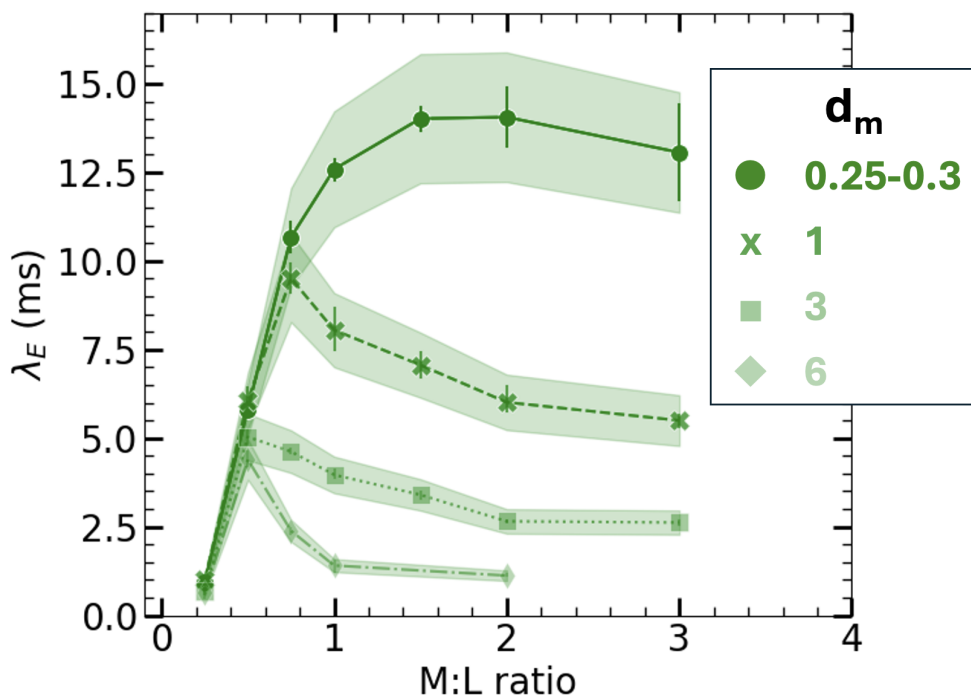


Figure 4.5: λ_E for Metal \rightarrow Dilute protocol for M:L ratio = 0.5, 0.75, 1, 1.5, 2, and 3 from $d_m = 0.25$ to 6. Error bars: $n_{drops} \geq 3$; Error bands: $13\% \pm$ uncertainty (see Appendix A).

$M_{umi} = 0.84$ MDa; Solvent = unbuffered MilliQ; $c = 0.04$ wt%; Metal \rightarrow Dilute; $T_s = 22^\circ\text{C}$; Vial storage.

Keeping in mind that the higher M:L ratios are not nearly as stable (for both protocols), we can still draw some comparisons with the maximum observed relaxation times for different M:L ratios. The differences in the M:L ratios are even greater for Metal \rightarrow Dilute than observed in Dilute \rightarrow Metal, as eluded to previously by the raw DoSER profiles. For the Dilute \rightarrow Metal protocol, M:L = 0.75 gives a

maximum λ_E at nearly 2.5 ms, about a 25% increase from M:L = 0.5 (Figure 3.6). For Metal \rightarrow Dilute, at this same M:L ratio = 0.75, λ_E reaches nearly 11 ms on $d_m = 0.25$, about a 50% increase from M:L = 0.5. Even further, the maximum λ_E we observed isn't reached until M:L = 1.5, which gives $\lambda_E = 14$ ms for the Metal \rightarrow Dilute protocol! It is important to emphasize that these maximum λ_E values we observed were taken just 6-7 hours after the metal was added, and after a full day, they decayed significantly. Also, for M:L > 2, the maximum observed λ_E begins to decrease, either due to the increased presence of metal and/or excessive end-capping. Possible explanations for a decrease in λ_E are elaborated on in the following section.

4.2.3 Order of operations affects λ_E equilibration and decay

The supramolecular equilibration distribution at a given concentration and temperature is independent of path. If the distribution of megasupramolecules formed in the Metal \rightarrow Dilute protocol equilibrated in 4 days, as it does in the Dilute \rightarrow Metal, the λ_E would fall to 2 ms by $d_m = 4$. It is remarkable that it does not, and indicates their entirely different paths towards equilibration. For the Dilute \rightarrow Metal protocol, TPAM at M:L = 0.5 takes a few days to reach its maximum observed λ_E , whereas the Metal \rightarrow Dilute protocol does not reveal the same equilibration period (Figure 4.6). Instead, it is reasonable to assume that the TPAM megasupramolecules reach an equilibrium distribution in the high concentration (1 wt%, $c/c^* > 3.4$) within a few hours, closer to a timescale driven by the metal-ligand coordination, and then the path towards the $c = 0.04$ wt% distribution is very different. We have essentially created a condition in which the population is now rich in species with relaxation times higher than those of the high molecular weight tail of the equilibrium distribution of megasupramolecules (at 0.04 wt% at 22°C), whereas in the case of Dilute \rightarrow Metal, we created an initial condition in which the population is rich in species

with relaxation times faster than those of the high molecular weight tail of the equilibrium distribution. What is interesting is that the Metal \rightarrow Dilute species do not equilibrate in the same amount of time as Dilute \rightarrow Metal, suggesting a "quasi-stable" state of higher M_w species. After dilution, we can assume that any change in λ_E over the day since metal is added (which is, in the current chapter, also the day it was diluted to its final concentration) is driven either by a re-equilibration of the megasupramolecules at the new concentration and/or by the chemical degradation effects (outlined in Chapter 2 and expanded on in Chapter 3).

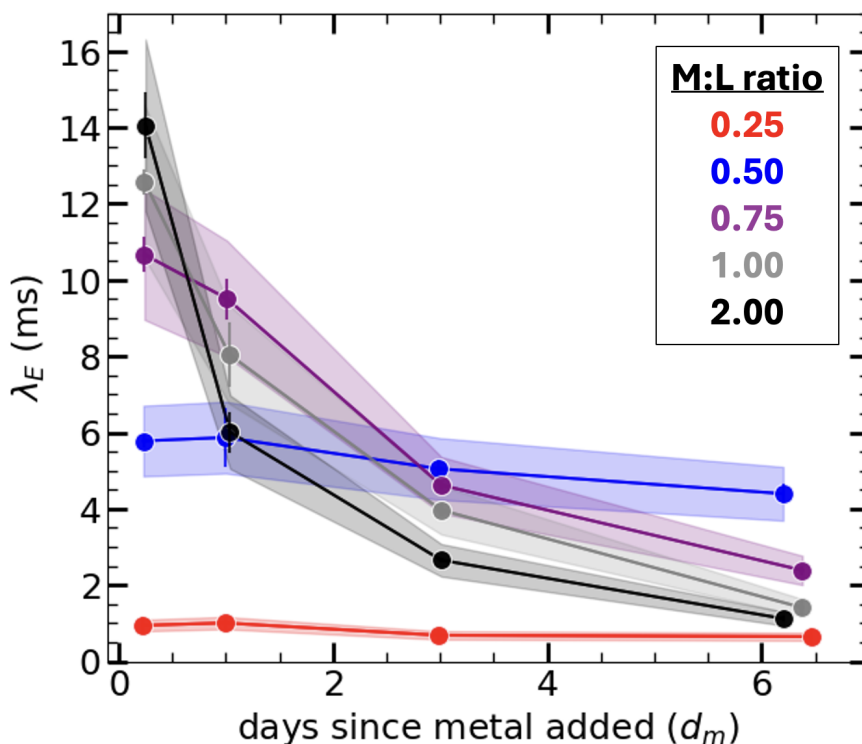


Figure 4.6: λ_E evolution over days since metal added for solutions prepared with Metal \rightarrow Dilute protocol with Ni(II) added such that M:L = 0.25, 0.5, 0.75, 1, and 2. Error bars: $n_{drops} \geq 3$; Error bands: 13% \pm uncertainty (see Appendix A).

$M_{uni} = 0.84$ MDa; Solvent = unbuffered MilliQ; $c = 0.04$ wt%; Metal \rightarrow Dilute; $T_s = 22^\circ\text{C}$; Vial storage.

Between the two protocols, we observe a similar λ_E stability trend with respect to the M:L ratios. For Metal \rightarrow Dilute, the lowest M:L = 0.25 results in a relatively constant λ_E around 1 ms for 6 days after metal was added. The stoichiometric

equivalent (M:L = 0.5) results in an increase in λ_E , as we saw with the previous protocol, that is relatively stable throughout the 6 days it is observed. As we increase M:L ratio, the initial (and maximum observed) λ_E at $d_m \approx 0.25$ also increases, but we again see that the higher M:L ratios exacerbate the λ_E decay. Considering the similarity in what we saw for the original Dilute \rightarrow Metal protocol where the λ_E decay was entirely driven by chemical degradation (a decreased ability to form metal-ligand links), it is reasonable to speculate that this decay is driven by the same factor. However, it is interesting that λ_E continues to increase as M:L is increased between M:L = 0.25 and 2. This could be explained by an increased number of linear chains (as opposed to cyclical ring chains) caused by the end-capping species (Figure 3.2).

We tested the change in λ_E at different storage temperatures and note that, qualitatively similar to Dilute \rightarrow Metal, higher temperature exacerbates decay while 4°C mitigates it (SI Figure 4.18). However, we also note that the rates of decay of the Metal \rightarrow Dilute protocol appear to be slightly faster overall than the rate of decay of Dilute \rightarrow Metal protocol: the approximate half lives for the 40°C is 1 and 1.5 days for different replicates, for 22°C is about 10 days, and for 4°C is extrapolated to be 120 days. This results in an activation energy E_A of 92 ± 11 kJ/(mol K), which is higher than that for the Dilute \rightarrow Metal protocol even given the 95% confidence intervals for our approximation. Considering the higher activation combined with faster decay rates, we posit that the overall decay process is likely more complex than that of Dilute \rightarrow Metal and may involve multiple steps or reactions (rather than a single reaction with a high energy barrier). This may be a combination of both a decrease in λ_E on its path towards equilibration in addition to degradation effects.

We might expect at some point for these two solutions, mixed in different orders but comprised of the same amounts of materials, to converge to the same properties at their final target concentration, but the presence of degradation effects precludes the

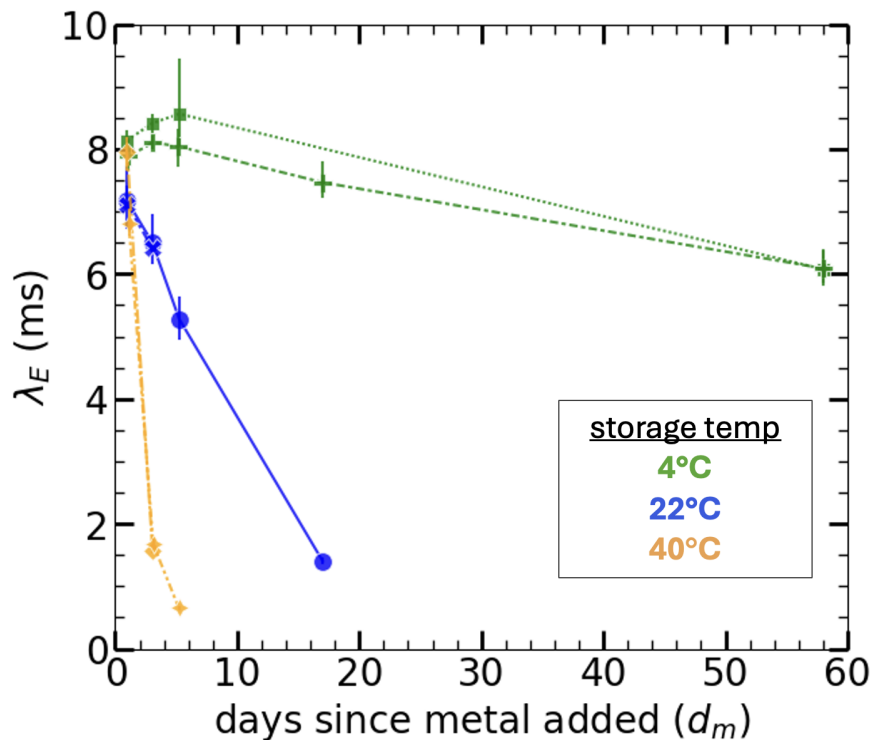


Figure 4.7: λ_E evolution over days since metal added at different storage temperatures (40°C, 22°C, and 4°C) for Metal \rightarrow Dilute protocol. Error bars: $n_{drops} \geq 3$. $M_{uni} = 0.84$ MDa; Solvent = unbuffered MilliQ; $c = 0.04$ wt%; M:L = 0.5; Metal \rightarrow Dilute; Vial storage.

potential for making that observation (Figure 4.8). Considering how much higher the λ_E for Metal \rightarrow Dilute protocol is compared to its counter part, one might actually expect to see a more rapid decay towards the shorter λ_E following dilution. Instead, we observe unexpectedly "quasi-stable" supramolecules that we suspect are exchanging ions within their own grouping of associated unimers, backed up by the previous general observation that the effective lifetime of reversible bonds are prolonged in higher concentrations of associative polymers [4]. While the overall solution concentration might be dilute ($c < c^*$), the megasupramolecules that form in the Metal \rightarrow Dilute polymer could be conglomerates of associated TPAM that create what is essentially a high concentration area that can continue exchanging metals between terpy linkages within the same conglomerate.

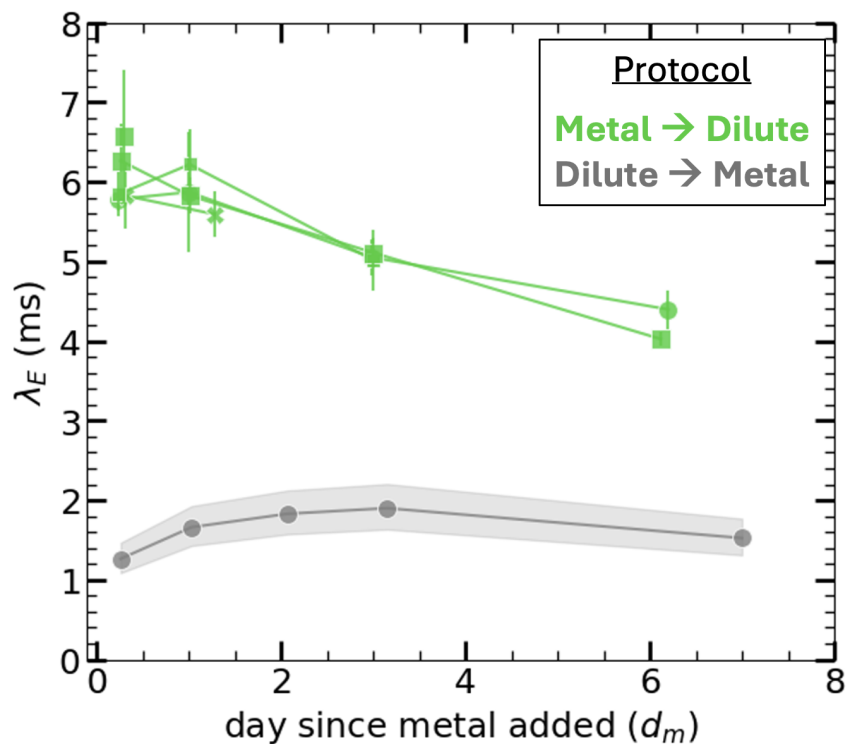


Figure 4.8: λ_E evolution over time for solutions prepared at Metal \rightarrow Dilute versus Dilute \rightarrow Metal. Dilute \rightarrow Metal points are also presented in Figure 3.6, and Metal \rightarrow Dilute points include the blue line shown in Figure 4.6. Error bars: $n_{drops} \geq 3$; Error bands: $16\% \pm$ uncertainty (see Appendix A). $M_{uni} = 0.84$ MDa; Solvent = unbuffered MilliQ; $c = 0.04$ wt%; M:L = 0.5; Vial storage.

We emphasize that despite the complications that arise due to decay at various M:L ratios, we have achieved around a 5x increase in λ_E , using all the same materials in the same amounts, just changing the order of which the materials are mixed together. This transformation of the extensional behavior is interesting and exciting alone, but it leaves us wondering what is occurring topologically to cause such a dramatic increase. We investigate the topological possibilities in the following sections.

4.3 Adding Ni(II) to TPAM before dilution reveals a topological wonder

4.3.1 GPC traces suggest key differences in topology by varying order of operations

All of the GPC traces up to this point have shown a repeatable molecular weight vs elution time curve (dotted lines in Figure 3.5, for example). This indicates that in all of the prior Dilute \rightarrow Metal solutions, molecules with the same molecular weight on average shared the same pervaded volume, even when the molecular weight distributions differed. This completely changes under the Metal \rightarrow Dilute protocol, which shows a clear rise in the molecular weight vs elution time curves (Figure 4.9). We see that there could be megasupramolecular species approximately 3x the M_w with the same pervaded volume compared to the linear chains formed when adding metal at a unimer concentration of $c < c^*$ (from 1 MDa to 3 MDa, indicated by the black arrow in Figure 4.9). A topology that might be able to explain this is sketched in Figure 4.10, which represents something like a poly-catenanes.

Metallo-supramolecular poly-catenane has recently been developed, and although it uses a different associative binding scheme, the end products may be comparable [5]. GPC and NMR have been used to differentiate between the different species that can exist in such a system, and it is reasonable to assume that our polymers might manifest similar shapes, such as chains of cyclical "monomers" that link to form linear, larger cyclical, or branched supramolecules. It has even been shown that the topology varies significantly when mixed at different concentrations [6]. To our surprise and excitement, it has also been reported that interesting rheological, even elastic, behavior can result from the formation of such species. While this all hints at an intriguing and unexpected discovery, more work must be done to fully characterize the topology of these megasupramolecules and understand a fuller scope of their properties. The following sections describe one additional attempt to gain more insight using the tools available to us at present, leading up to a compelling

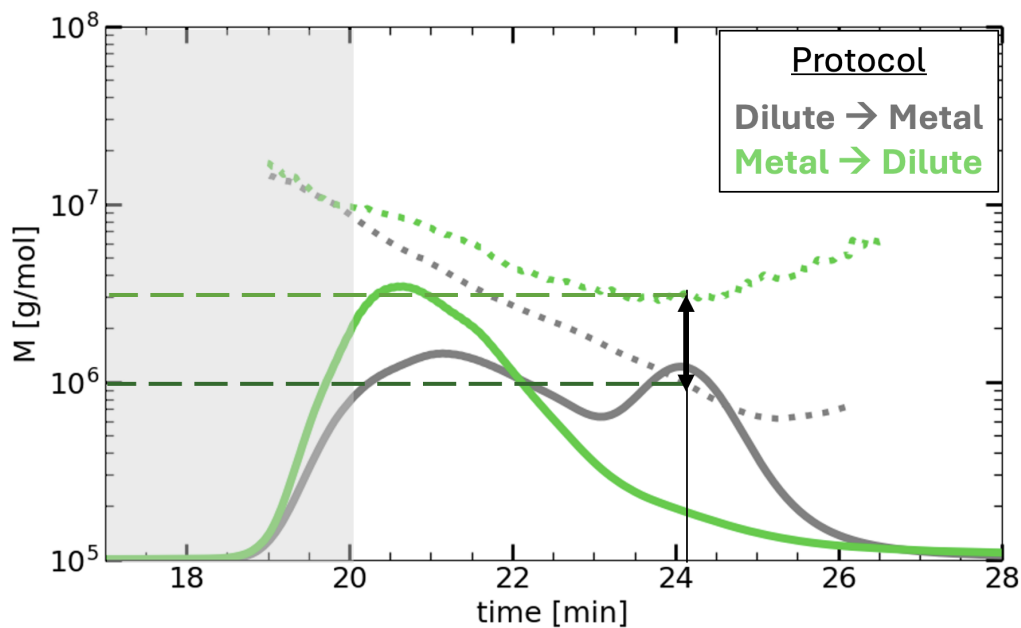


Figure 4.9: GPC results for solutions prepared at Metal \rightarrow Dilute versus Dilute \rightarrow Metal. The black line indicates the 3x difference in M_w at the same elution time for the different protocols (from 1 MDa to 3 MDa).

$M_{uni} = 0.84$ MDa; Solvent = unbuffered MilliQ; $c = 0.04$ wt%; M:L = 0.5; Vial storage.

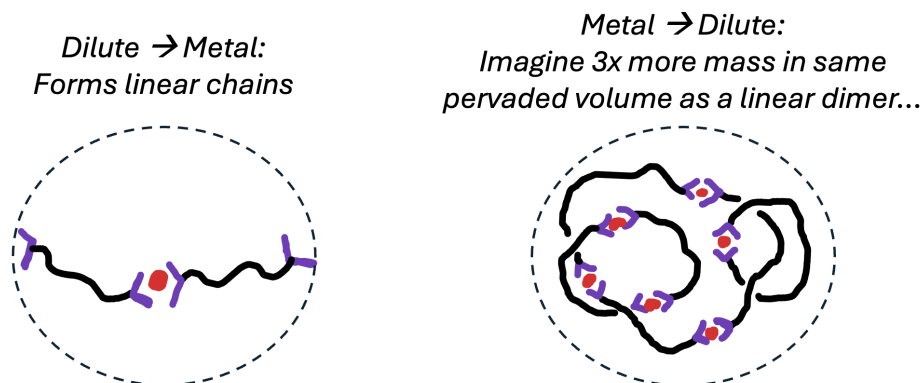


Figure 4.10: A speculative sketch of what the topology of the current TPAM supramolecules might look like with Metal \rightarrow Dilute protocol.

enough question to begin a collaboration with fellow researchers that have access to novel molecular characterization techniques that may provide a clearer picture.

4.3.2 Two paths forward: What are they, and what can they do?

The associative polymers made in this present chapter using the Metal \rightarrow Dilute protocol appear to have a totally different topology than the linear and/or ring chains made with the Dilute \rightarrow Metal protocol presented in Chapter 3. At this point, we can search for further insight on two, interrelated, but connected questions: what type of molecule have we created (topologically speaking), and what can this molecule do (rheologically speaking). Considering this, we will compare our results to what was observed on these molecules by Kim, and provide further insight on the molecular size extending to fractionation experiments. Lastly, we will explore how this molecule behaves in the context of turbulent drag reduction and chain scission resistance.

4.3.3 Comparison to previous results shows effect of filtration

TPAM unimers were synthesized by Kim, and to prove their efficacy, he also examined their megasupramolecular weight (as outlined in the Introduction) [2]. However, there is a key detail in the GPC procedure that affected the accuracy of Kim's analysis. Kim ran each solution through 0.45 μm syringe filters immediately prior to running them through GPC which, we emphasize, is an appropriate and common procedure taken to sterilize a solution and eliminate contaminant particles that can clog the column and disrupt GPC usage. Reasonably, it was not suspected that this filter would disrupt the passage of molecules. It was only until our current study, where we explicitly connected observations of bulk fluid performance with underlying molecular structure, that we noticed inconsistencies which led us to this revelation.

We can highlight the importance of this realization by comparing our samples with and without 0.45 μm syringe filtration to Kim's results on solutions under similar conditions. Kim added Ni(II) at M:L = 0.5 to a 1 wt% 0.82 MDa TPAM solution

and then diluted to 0.01 wt% before the GPC measurements (i.e., a Metal \rightarrow Dilute protocol). Our TPAM unimers were 0.84 MDa and our final concentration was 0.04 wt%, but we can still draw a reasonable comparison between the two which illuminates the consistent effect of syringe filtration. By comparing the GPC traces, we already see an obvious shift towards larger megasupramolecules in our unfiltered distribution compared to Kim's (Figure 4.11). While Kim reported a maximum $M_w = 4.09$ MDa (PDI = 1.56) for his TPAM solutions, our unfiltered solution measured $M_w = 6.8$ MDa (PDI = 1.2). The GPC traces for our syringe filtered solution overlaps with Kim's and has a very similar $M_w = 4.2$ MDa (PDI = 1.53), indicating that while Kim's results did not capture the complete picture for the megasupramolecules created with the Metal \rightarrow Dilute protocol, they are at least consistent with what we see now when we reproduce Kim's procedures.

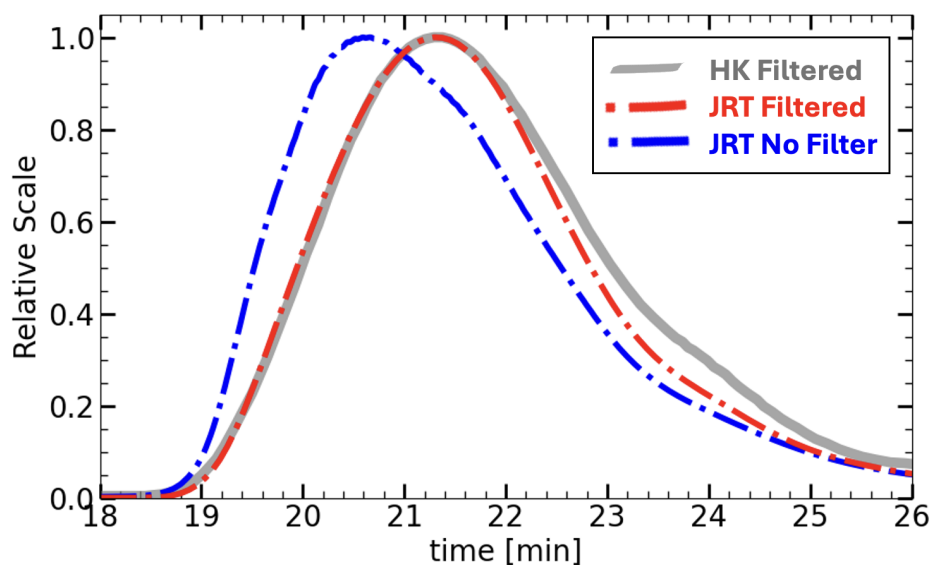


Figure 4.11: A comparison between the GPC traces for Kim's 0.45 μm syringe filtered solutions (HK Filtered) versus the current solutions, both filtered (JRT Filtered) and not (JRT No Filter).

This realization that 0.45 μm syringe filters interact with the megasupramolecules enough to drastically alter the filtrated solutions average M_w and distribution led us to another curiosity—can we use filtration in a systematic way to gain more

insight on the size of the megasupramolecules that go beyond our GPC upper limit? We explore this in the following section.

4.3.4 Using filtration to help characterize and fractionate megasupramolecules

Fractionation of polymers is highly relevant to industrial chemical processing and scientific research, and thus, researchers have been exploring the topic for decades [7]. In both natural and synthetic solutions, a variety of molecules or suspended particles can be present. Often, it is of interest to separate out different sized species, whether it be for industrial settings like waste, textile, and food processing, or for scientific sample purification. We have already discussed GPC, which is one method for eluting molecules at different times based on their size to obtain a molecular weight distribution. Another approach is ultrafiltration. Ultrafiltration requires a membrane with a specific pore size that can separate molecules based on a molecular weight cut-off—molecules over the cut-off are retained, and molecules below the cut-off are filtered through [8]. Typically, ultrafractionation is used to fractionate macromolecules with pore sizes ranging from 1-10 nm, while microfiltration is used to fractionate suspended particulate from a solution with pore sizes on the order of 0.1-10 μm . Considering these Metal \rightarrow Dilute TPAM polymers are much closer to the size regime for suspended particles, and outside the regime for our GPC (10 MDa), we can instead use a membrane filter with a known pore diameter to get a sense of how big the polymers are.

We use cellulose acetate centrifuge filters with two different pore sizes: 0.22 μm and 0.45 μm . 0.75 mL of solution is pipetted into the centrifuge filters, which are centrifuged at 10,000 relative centrifugal forces (rcf) for 15 minutes. Within that time, approximately half of the solution permeates the filter creating a "filtrate" solution, while the rest is left behind as "retentate" solution (Figure 4.12).

The GPC traces reveal that there is a higher concentration leftover in the retentate,

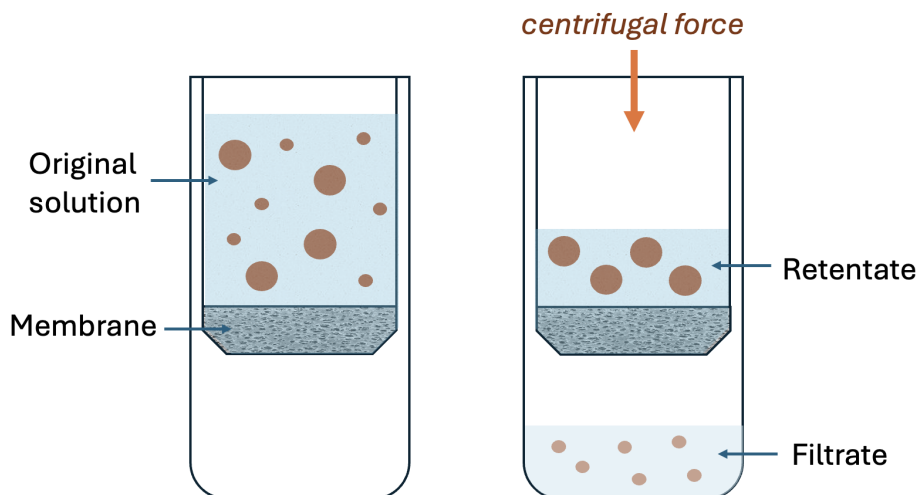


Figure 4.12: A sketch of the fractionation of polymers with microfiltration. Polymers are represented as big and small molecular species. When the centrifugal force is applied to the solution, the smaller molecules can pass through, while the larger ones are retained and unable to permeate the membrane.

and that the M_w vs elution time curve still indicates a high population of the mystery topology species (Figure 4.13). The filtrate contains a lower concentration of megasupramolecules overall, and the M_w vs elution time curve is back to the standard slope that we repeatedly observed in the Dilute \rightarrow Metal protocol. Considering the filter size was $0.45 \mu\text{m}$, this indicates that it is likely some truly massive species around this size are retained by the filter. Further, the GPC trace also indicates that a non-trivial amount of smaller linear or cyclical species may be present in the mixture.

Using DoSER and a smaller filter size of $0.22 \mu\text{m}$, we compare the λ_E change for the retentate and filtrate (Figure 4.14). We see here that a smaller filter size results in a higher retentate λ_E , indicating that megasupramolecular species exist at sizes within the range of these filter pores sizes, and that there are enough of them to contribute significantly to the extensional behavior.

Combining all of this insight leads us to the conclusion that the Metal \rightarrow Dilute protocol forms a wider range of megasupramolecular sizes and structures. The

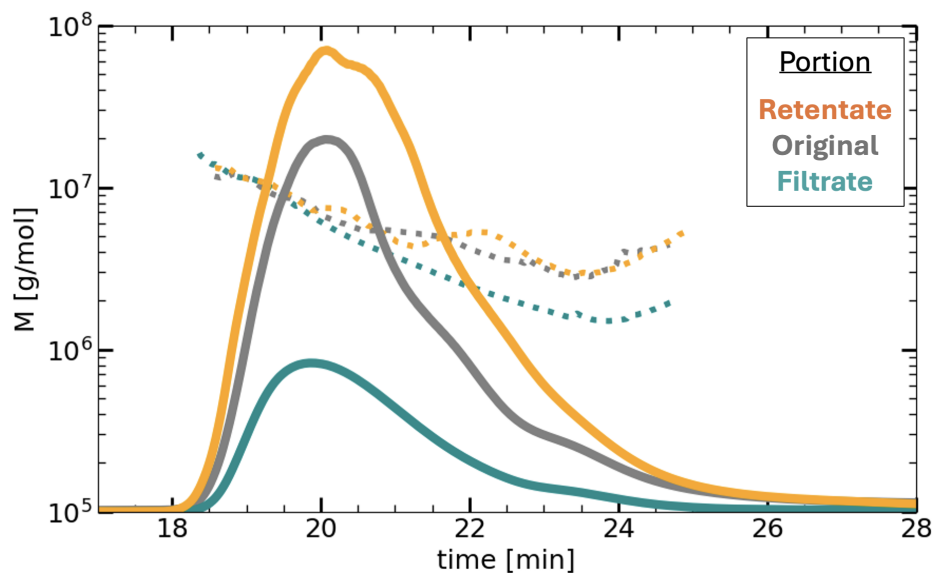


Figure 4.13: GPC curves on the original, retentate, and filtrate solutions. Solutions were filtered with $0.45 \mu\text{m}$ using centrifuge. $M_{uni} = 0.84 \text{ MDa}$; Solvent = unbuffered MilliQ; $c = 0.04 \text{ wt}\%$; M:L = 0.5; Metal \rightarrow Dilute; Vial storage.

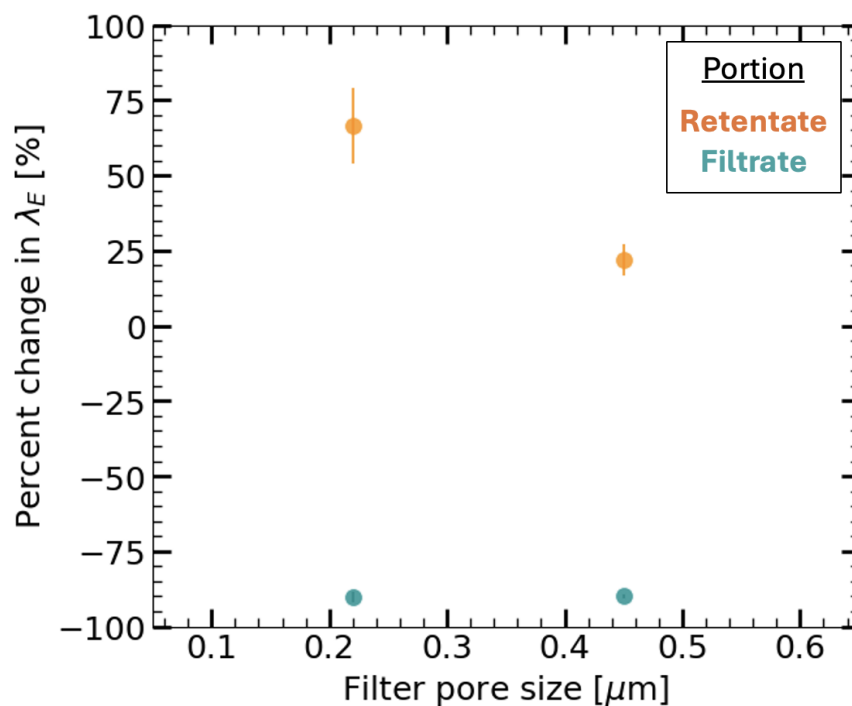


Figure 4.14: Percent change in λ_E for the retentate and filtrate within 0.22 and $0.45 \mu\text{m}$ centrifuge filters, compared to the original unfiltered solution. Error bar: $n_{drop} \geq 3$. $M_{uni} = 0.84 \text{ MDa}$; Solvent = unbuffered MilliQ; $c = 0.04 \text{ wt}\%$; M:L = 0.5; Metal \rightarrow Dilute; Vial storage.

potential for using this unique distribution of molecules in drag reduction and an investigation into its scission resistance is presented in the following section.

4.4 TPAM reduces turbulent drag and resists chain scission, but Metal \rightarrow Dilute molecules are not "self-healing"

The following results were obtained using a polymeric drag reduction and mechanical chain scission instrument that was conceptualized and constructed in a collaboration between Professor Beverley McKeon and Professor Julie Kornfield with their previous graduate students, Dr. Ryan McMullen, Dr. Huynh, and Dr. Red Lhota. My contribution in improving and validating crucial elements of the experiment are detailed in Appendix B. In summary, I first characterized the instrument's drag reduction, degradation, and particle image velocimetry (PIV) capabilities. After this validation step and subsequent improvements, using polyethylene oxide (PEO) I identified polymeric drag reduction structures using PIV at $Re \approx 7.5 \times 10^4$, which are shown in Chapter 1. Bulk effects of the drag reduction induced by PEO and polyacrylamide (PAM) were also identified with mass flow measurements, and their respective λ_E decay due to chain scission was measured (also reported in the thesis of Red Lhota [9]). Bulk drag reduction is determined based on the change in Reynolds number (4.4), which is determined via mass flow rate measurements.

$$Re_B = \frac{4\dot{m}}{\pi\mu D} \quad (4.1)$$

For the current chapter, this instrument was used to make the first observation of the turbulent drag reducing capabilities of end-associative terpyridine PAM (TPAM) made with the Metal \rightarrow Dilute protocol, and their subsequent decay.

4.5 Bulk drag reduction results for PEO, PAM, and TPAM

We assess the bulk drag reduction that occurs using 6 MDa PEO and 6.7 MDa PAM both at 66 wppm, and 0.83 MDa TPAM at 200 wppm using the Metal \rightarrow Dilute protocol. The results for PEO and PAM were presented in the thesis of Red Lhota [9] and are reproduced here for comparison with end-associative TPAM. Lhota details the interpretation of PEO and PAM's comparison, highlighting that PEO has a weaker backbone and is more susceptible to scission, which is evident by its clear decrease in bulk Reynolds number, Re_B , over pass through the system. PAM has a less obvious decrease in drag reducing abilities, but undergoes polymer chain scission. It is important to acknowledge the role that the contraction (from the supply tank to the pipe) and expansion (from the pipe to the receiving tank) may obscure the true change in bulk drag reduction abilities. While long, flexible, dilute polymers are known to increase the flow rate through turbulent pipes, they actually have the opposite effect on contractions and expansions. It should be noted that the scission that can occur with each pass might actually increase the flow rate through the contraction and expansion, which makes the Re_B characterization of bulk drag reduction less clear. However, we can still draw some important conclusions from this results as we compare standard PEO and PAM to TPAM.

Despite these complexities, important insights can still be drawn from our comparative analysis of standard PEO and PAM with TPAM. The choice of 200 wppm for the TPAM solution was based on achieving a comparable relaxation time to that of 6 MDa PEO and 6.7 MDa PAM at 66 wppm. This approach aimed to provide a more analogous comparison to the drag reduction achieved by the more standard polymers, which our results have confirmed within the experimental uncertainty.

The most noteworthy finding is that the megasupramolecules formed with the Metal \rightarrow Dilute protocol function as effective drag-reducing agents. Any amount of drag reduction and robustness was not a given, considering the apparent complexity of

the molecular topology produced by this method. Moreover, our results indicate a higher bulk drag reduction for TPAM in the initial pass compared to the tenth pass, suggesting that while drag reduction is achieved, molecular changes likely do occur with successive passes. This observation will be investigated further in the following section.

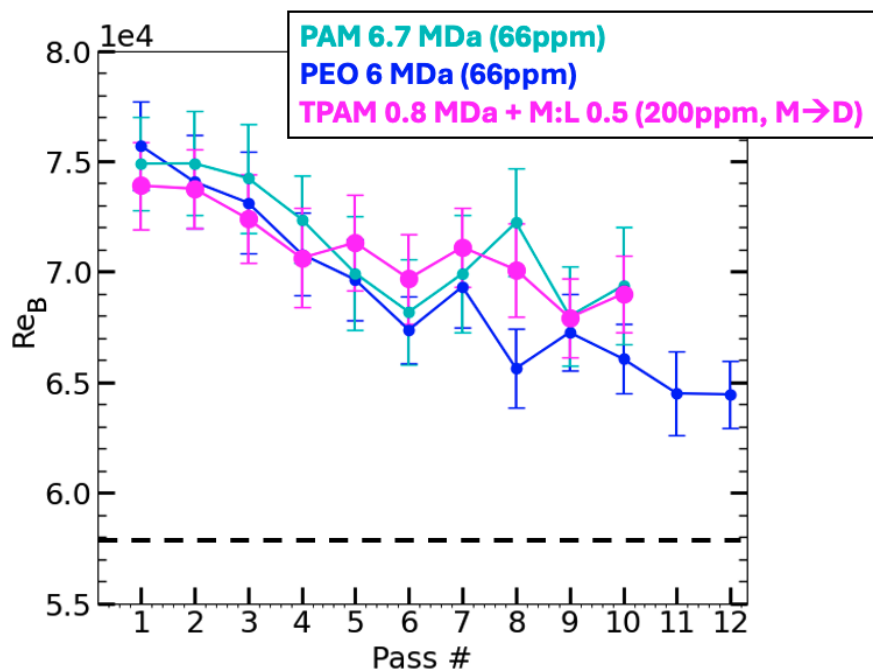


Figure 4.15: Re_B changes with pass through the system for 66 wppm 6 MDa PEO and 6.7 MDa PAM, and 200 wppm TPAM prepared with M:L = 0.5 using Metal \rightarrow Dilute protocol. All experiments were run with a 40 psi pressure drop. The dashed line represents the Re_B for DI water at 40 psi through the system. Error bars represent the 95% confidence intervals on the slopes calculated by measuring the changing mass in the receiving tank.

4.5.1 Changes in polymer property and structure with pass through the drag reduction apparatus

We used DoSER and GPC to assess the changes that occur in the λ_E for all three polymers. 10 mL samples were taken from the receiving tank at the completion of each pass, and upon the conclusion of the whole data set, DoSER and GPC were run immediately. GPC was only used on the TPAM solutions to assess their changing

molecular weight distribution, as the concentrations for PEO and PAM were too low to get a reliable signal. Red Lhota performed DoSER for the PAM and PEO solutions which are presented in their thesis and reproduced here for comparison with TPAM. I ran DoSER on the TPAM solutions as well as the GPC analysis.

While we mitigated the chain scission that can occur due to pumping by using a pressurized tank to push the flow, we were ultimately able to fully attribute the scission to the contraction and expansion before and after the pipe. Therefore, we cannot connect the scission to turbulence alone. However, we can still make some interesting observations on the changing λ_E in comparison to PAM and PEO as well as the molecular weight distributions over 10 passes compared to the unimer.

We see that while PAM and PEO both had initially higher λ_E relative to TPAM before any runs through the instrument, their subsequent decay is more steep. It is reasonable to suspect that these polymers did likely experience more chain scission due to their long length and lack of end-associative abilities, but for PAM and TPAM, it was not enough to cause as appreciable of a difference in the bulk drag reduction. We should highlight that while it is understood that longer λ_E generally contributes to higher drag reduction, there is not yet a clearly defined, predictable relationship between the two, especially when comparing different polymer backbones and structures.

The key observation here is that the TPAM megasupramolecules that form from the Metal \rightarrow Dilute protocol do not maintain a constant λ_E . This is not too surprising considering the complexity of the supramolecular structure may result in quasi-stability. We posit that the supramolecules exchange ions within individual clusters which can stretch out and elicit extensional properties, but once the fluid system is severely disturbed, the clusters may break apart into a system of more standard dilute end-associative solution of linear and ring species. In fact, it may be a misnomer at

this point to call them "supramolecules" as one essential element to a supramolecule is self healing. While the individual TPAM unimers may still be able to self heal, it would be entropically impossible for them to re-organize themselves back into the potentially tighter clusters that form when adding metal to the higher concentrated solution prior to dilution.

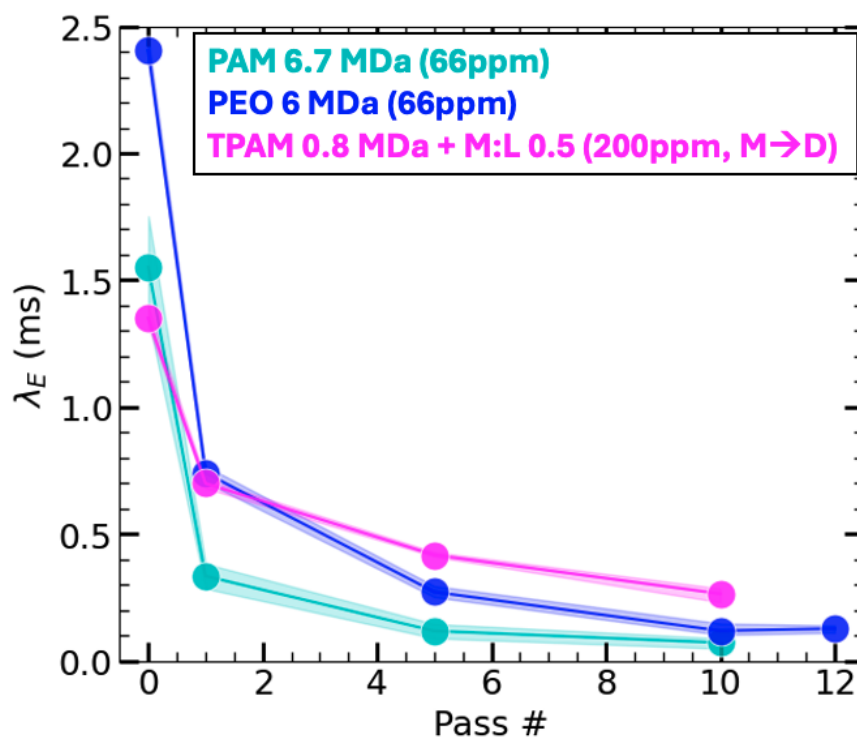


Figure 4.16: λ_E changes with pass through the system for 66 wppm 6 MDa PEO and 6.7 MDa PAM, and 200 wppm TPAM prepared with M:L = 0.5 using Metal \rightarrow Dilute protocol.

From the DoSER analysis alone, we are still left wondering if the TPAM unimers are still intact—GPC reveals that they are (Figure 4.17). This indicates that TPAM unimers can likely resist the mechanical scission that degraded the covalent PAM and PEO. Future work should assess the different preparation protocol, where the solution is diluted prior to the addition of metal (Dilute \rightarrow Metal) and the mega-supramolecules equilibrate to, what we hypothesize to be, a more robust distribution of drag reducing molecules.

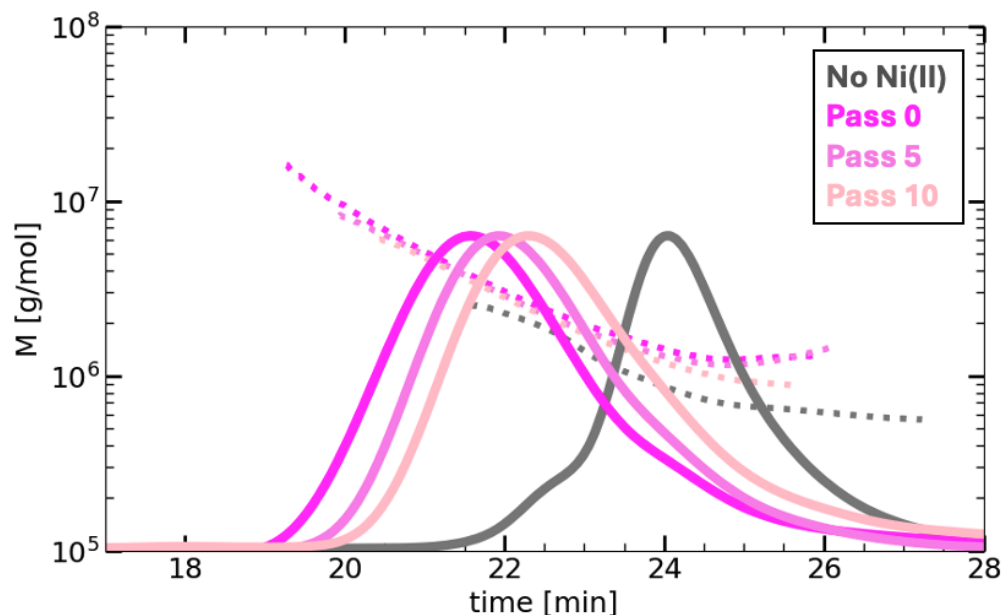


Figure 4.17: GPC traces change with pass through the system for 200 wppm TPAM prepared with M:L = 0.5 using Metal \rightarrow Dilute protocol, but the unimers remain intact.

4.6 Conclusions and Future Work

In this chapter, we have explored the impact of order of operations on the formation and stability of TPAM megasupramolecules, gleaned several key insights. It is evident that the order in which the materials are mixed has a profound impact on the resulting megasupramolecular structures and properties. The Dilute \rightarrow Metal protocol generally results in a gradual, initial rise in λ_E , whereas no such gradual increase is observed for Metal \rightarrow Dilute. Also, as the M:L ratio increases, the maximum observed λ_E also increases. However, excess metals tend to exacerbate the decay of λ_E over time, suggesting that while more metal ions can initially boost the formation of larger megasupramolecules, they may also accelerate their degradation and/or re-equilibration to smaller species, like we saw in the case of Dilute \rightarrow Metal.

GPC traces reveal that the Metal \rightarrow Dilute protocol creates species with approximately three times the molecular weight of those formed with Dilute \rightarrow Metal, yet

with the same pervaded volume, suggesting the formation of more intricate topologies. Filtration experiments further support the presence of megasupramolecular species with an exceptionally large pervaded volume (or radius of gyration). There are significant differences observed between retentate and filtrate solutions, indicating a variety of sizes and shapes.

The intriguing and unexpected discovery of these large, seemingly complex structures opens up new avenues for research, particularly in deepening our understanding of their topological nature and rheological behavior. Further characterization using advanced molecular characterization techniques are being pursued, such as a collaboration using Charge Detection Mass Spectrometry with colleagues at Berkeley [10] and/or Flow Field Fractionation with our DOW sponsors [11]. These techniques would provide deeper insight on the size and shape of the mystery molecules. In the meantime, we delve into the practical implications of these findings, exploring the use of these unique megasupramolecular distributions in turbulent drag reduction and their resistance to chain scission in the following chapter.

In terms of practical applications for these molecules, we showed that 200 wppm TPAM with M:L = 0.5 prepared with the Metal \rightarrow Dilute protocol is capable of a bulk drag reduction comparable to that of 6 MDa TPAM and 6.7 MDa PAM at 66 wppm. We confirmed that the λ_E of this TPAM solution does decrease after multiple passes through the system, but the unimers remain intact. This confirms that the particular topological distribution made with the solution preparation protocol is able to reduce drag, but it also suggests that the topological distribution is not robust to the turbulent and extensional disturbances within our system. However, the surviving unimers are very promising. Future work should investigate different preparation protocol for TPAM to see if other topological distributions are more robust and ultimately self-healing. The validation of TPAM as a self healing, chain-scission resistant polymer would not only have enormous impacts on industry, but it

would open up new avenues for polymeric drag reduction research. Namely, of great interest is visualizing the polymer drag reduction structures at ultra high Reynolds numbers that break standard drag reducing agents too quickly for robust reliable experiments. TPAM is potentially a viable option for exploring that avenue in future studies.

4.7 Supplementary Figures

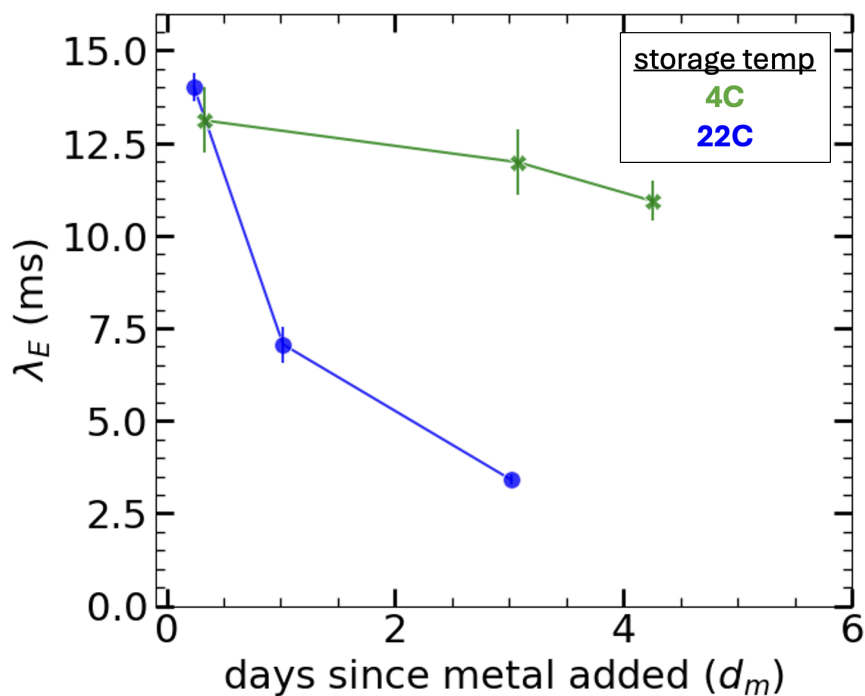


Figure 4.18: λ_E evolution over days since metal added at different storage temperatures (22°C and 4°C) for Metal \rightarrow Dilute protocol mixed with M:L = 1.5. This result indicates that the higher M:L solutions with excess metal exceeding the stoichiometric equivalent with the amount of terpys in solution are also more stable when stored in the fridge.

$M_{uni} = 0.83$ MDa; Solvent = unbuffered MilliQ; $c = 0.04$ wt%; M:L = 0.5; Metal \rightarrow Dilute; Vial storage.

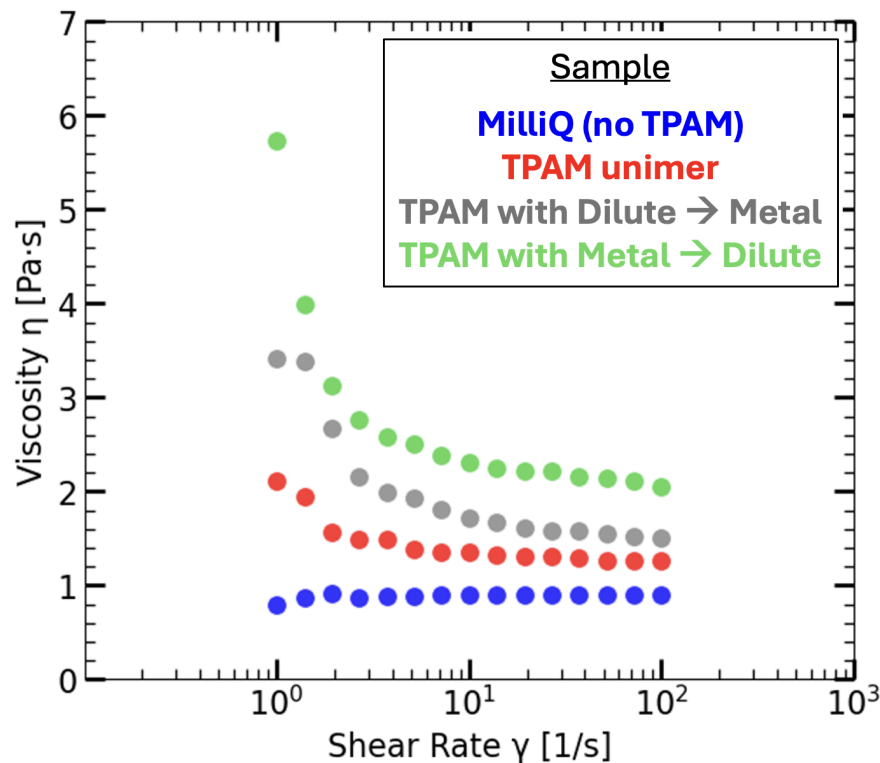


Figure 4.19: Shear viscosity data for MilliQ (no TPAM), TPAM unimers, TPAM + Ni(II) solution with Dilute \rightarrow Metal protocol, and TPAM + Ni(II) solution with Metal \rightarrow Dilute protocol. Measurements taken on an Anton Paar MCR 302 WESP rheometer using a cone-and-plate fixture.

$M_{uni} = 0.83$ MDa; Solvent = unbuffered MilliQ; $c = 0.04$ wt%; M:L = 0.5; Vial storage.

References

- [1] Reece W. Lewis et al. “Ultra-high molecular weight linear coordination polymers with terpyridine ligands”. In: *Chemical Science* 10.24 (2019), pp. 6174–6183. ISSN: 2041-6520, 2041-6539. DOI: [10.1039/C9SC01115C](https://doi.org/10.1039/C9SC01115C).
- [2] Hojin Kim. “New Long End-Associative Polymers for Mist Control in I. Aqueous Solutions and II. Hydrocarbon Solvents”. Medium: PDF Version Number: Final. PhD thesis. California Institute of Technology, Aug. 26, 2022. DOI: [10.7907/R SX9-QT39](https://doi.org/10.7907/R SX9-QT39).
- [3] Robert Learsch. “Droplet control in aqueous and hydrocarbon fluids: Long, end-associative polymers dictate fluid behavior under elongational flows”. PhD thesis. Caltech, Oct. 20, 2022.
- [4] Michael Rubinstein and Alexander N. Semenov. “Dynamics of Entangled Solutions of Associating Polymers”. In: *Macromolecules* 34.4 (Feb. 1, 2001), pp. 1058–1068. ISSN: 0024-9297, 1520-5835. DOI: [10.1021/ma0013049](https://doi.org/10.1021/ma0013049).

- [5] Qiong Wu et al. “Poly[n]catenanes: Synthesis of molecular interlocked chains”. In: *Science* 358.6369 (Dec. 15, 2017), pp. 1434–1439. ISSN: 0036-8075, 1095-9203. DOI: [10.1126/science.aap7675](https://doi.org/10.1126/science.aap7675).
- [6] Marissa M. Tranquilli, Qiong Wu, and Stuart J. Rowan. “Effect of metallosupramolecular polymer concentration on the synthesis of poly[n]catenanes”. In: *Chemical Science* 12.25 (2021), pp. 8722–8730. ISSN: 2041-6520, 2041-6539. DOI: [10.1039/D1SC02450G](https://doi.org/10.1039/D1SC02450G).
- [7] Abdul Mohammad et al. “Ultrafiltration in Food Processing Industry: Review on Application, Membrane Fouling, and Fouling Control”. In: *Food and Bioprocess Technology* 5 (May 2012). DOI: [10.1007/s11947-012-0806-9](https://doi.org/10.1007/s11947-012-0806-9).
- [8] Munir Cheryan. “Ultrafiltration and Microfiltration Handbook”. In: ().
- [9] Red C. Lhota. “Rheological Characterization of Polymer Additives for Mist Control and Drag Reduction”. Medium: PDF Version Number: Final. PhD thesis. California Institute of Technology, May 27, 2022. DOI: [10.7907/WAV1-4T47](https://doi.org/10.7907/WAV1-4T47).
- [10] Conner C. Harper et al. “Multiplexed Charge Detection Mass Spectrometry for High-Throughput Single Ion Analysis of Large Molecules”. In: *Analytical Chemistry* 91.11 (June 4, 2019), pp. 7458–7465. ISSN: 0003-2700, 1520-6882. DOI: [10.1021/acs.analchem.9b01669](https://doi.org/10.1021/acs.analchem.9b01669).
- [11] J. Calvin Giddings. “Field-Flow Fractionation: Analysis of Macromolecular, Colloidal, and Particulate Materials”. In: *Science* 260.5113 (June 4, 1993), pp. 1456–1465. ISSN: 0036-8075, 1095-9203. DOI: [10.1126/science.8502990](https://doi.org/10.1126/science.8502990).

Chapter 5

CONCLUSION

In this thesis, we have explored the chemical stability, rheological properties, and performance of aqueous, metallo-megasupramolecule, terpyridine-ended polyacrylamide (TPAM). With each chapter, we uncover insights into how these long, end-associative molecules may ultimately be used with greater robustness and effectiveness to control droplet size or reduce turbulent drag in engineering flows. By systematically investigating TPAM's behavior—from its equilibration to its degradation, topological distribution, and rheological performance—this work establishes a foundation for its application as an effective rheological modifier.

The study began by addressing the chemical stability of TPAM, focusing on the rise and decay of λ_E as it depends on molecular structure, preparation methods, and environmental conditions. The key factors we identified that influence degradation are metal-to-ligand ratio (excess metal ions elicit faster decay), air exposure, and storage temperature. Storing samples at 4°C delays degradation by several weeks, compared to 40°C that causes decay within the first 24 hours. Our findings established the need for further collaboration with mass spectrometry experts who can uncover precise degradation products and illuminate the exact mechanism(s). The development of protocols to mitigate TPAM's λ_E decay and a deeper understanding of what influences its rate enabled us to more robustly explore its behavior under diverse conditions.

Subsequent chapters examined how M_w distribution and metal-to-ligand ratios influence TPAM's topology and extensional behavior. Altering these parameters allowed for tuning megasupramolecular size and λ_E . When adding metal to dilute solutions (0.04 wt%), we can access λ_E ranging from 0.5 to 3 ms. By introducing metals at

higher concentrations (1 wt%) prior to dilution, we unlocked novel topologies with unprecedented M_w values exceeding 10 Mg/mol, increasing the maximum observed λ_E by 3 to 6 times. It was observed that TPAM does reduce drag to a similar degree as more standard additives (i.e. PEO, PAM). However, even with its reversible associative links, it did not maintain a steady λ_E under turbulent conditions when the metal \rightarrow dilute preparation protocol was used to make the solution. Fortunately, we found that the backbones remained intact through repeated contractions, expansions, and turbulence, even when the λ_E fell, indicating the lack of robustness could be due to the unconventional nature of the megasupramolecules made with the Metal \rightarrow Dilute protocol. This highlights the need for further exploration of the Dilute \rightarrow Metal protocol and a broader range of concentrations to better harness TPAM's reversible nature and achieve consistent properties.

The broader implications of this work are particularly relevant to aerospace engineering research. As highlighted in Saeed and Elbing (2023) "Polymer drag reduction: A review through the lens of coherent structures in wall-bounded turbulent flows", the next step towards a deeper understanding of polymer drag reduction flow phenomena requires high Reynolds number testing ($Re > 10^6$). However, polymer chain scission is a major roadblock as it results in nonuniform and uncontrolled polymeric conditions. This thesis provides a promising foundation for the use of TPAM to overcome this roadblock, which would pave an entirely uncharted path for polymeric drag reduction research. Chain scission is not only a challenge for aerospace research but also for practical applications, such as pipelines, where drag-reducing agents must be replenished at multiple pumping stations. TPAM's resistance to chain scission under turbulent conditions and intense expansion and contraction flows demonstrates its promise as a more robust alternative.

Looking ahead, future work should focus on expanding the testing of TPAM in turbulent flows and exploring its scalability for agricultural and aerospace systems.

The insights gained here provide a strong foundation for such efforts, emphasizing the importance of interdisciplinary collaboration to fully realize TPAM's potential. By integrating materials science, fluid mechanics, and engineering design, the development of TPAM can advance toward practical, high-impact applications that meet the demands of modern engineering challenges.

In conclusion, this thesis establishes TPAM as a promising platform for addressing critical challenges in flow control, from mitigating turbulent drag to optimizing droplet dynamics. The systematic approach taken here to characterize and optimize TPAM's behavior not only advances the fundamental understanding of these aqueous, metallo-megasupramolecules but also lays the groundwork for their integration into robust, real-world systems. This work highlights the potential of TPAM and opens new pathways for innovation in sustainable and efficient engineering practices. Its diverse applications, coupled with its self-healing properties and tunable performance, position TPAM as a transformative material in the field of rheological modifiers.

*Appendix A*QUANTIFYING UNCERTAINTY AND SAMPLE
REPRODUCIBILITY

To set bounds of the extensional relaxation time (λ_E) of TPAM megasupramolecules on stability and tunability, we need to establish the reproducibility of replicate sample solutions. Sources of unintended variation include impurities in the water used to prepare solutions, the type of container, measurement uncertainty of reagents, and method of mixing and storing solutions. We needed to mitigate these extraneous effects to discern the effects of sample composition (i.e. M:L ratio, unimer M_n , etc) on megasupramolecular formation, degradation, and rheological properties. To develop robust protocols and quantify reproducibility, we consulted with analytical chemistry expert, Dr. Nathan Dalleska, Lead Laboratory Administrator for Caltech's Water and Environment Lab.

Dr. Dalleska recommended that we use water freshly purified to ASTM Type 1 (resistivity $> 18 \text{ M}\Omega \text{ cm}$, total organic carbon TOC $< 50 \text{ ppb}$) which we obtain with a Millipore Direct-Q 3 purification system (referred to as MilliQ). The Kornfield group has been using glass vials for TPAM-metal solutions due to the gas barrier properties of glass. He noted that in our applications, the interaction of glass with ions could provide a source or sink of metal ions that could affect our results and suggested that we try single-use polyethylene vials. We also used a 0.5 mM concentrated NiCl_2 solution so that the volume of NiCl_2 was on the higher (and more accurate) measurement region for our pipette ($10 \mu\text{L}$). We also cover all solutions in aluminum foil to prevent UV degradation.

To quantify the remaining uncertainty with the above improvements, Dr. Dalleska recommended that we prepare two replicate TPAM "parent solutions", then multiple

replicate "child solutions" (diluting and adding metal) from each parent. Then, we measure the λ_E for each child solution (Figure A.1) to assess the variability between separate parent solutions as well as children from the same parent.

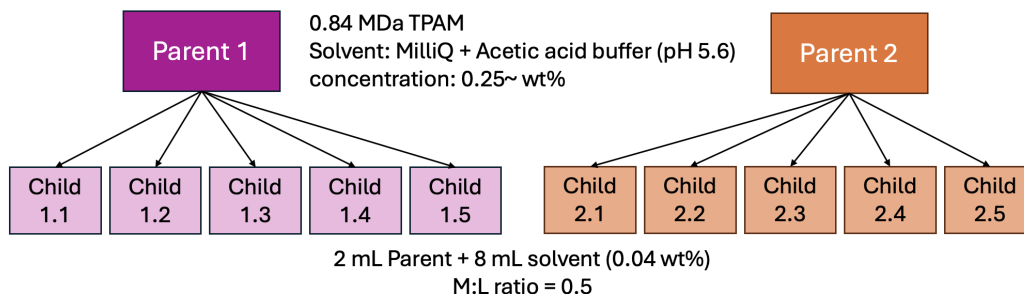


Figure A.1: Protocol for assessing variability between different higher concentration starting solutions ("parents") and their diluted + metal added megasupramolecular "child" solutions.

We first examined a complete set of parent-child solutions for a weakly acidic acetic acid pH 5.6 buffer. Then, partial parent-child studies were done for a neutral MOPS buffer, as well as unbuffered MilliQ with results of various studies aggregated from a range of 7 months. The potential interactions between the buffer and metal ions are described in Chapter 2 Section 2.6.3.

We captured the initial rise in λ_E for each child solution (described in Chapter 2 Section 2.2), then measured the λ_E 1 day after metal was added for each child solution, and then monitored the λ_E decay for a subset of child solutions (Figure A.2). Note that the short-term rise in λ_E and longer-term decay are described in Chapter 2. We calculate the standard deviation for the same parent solution to be 0.08 ms (a relative standard deviation of 5%), and the differing parent solutions to be 0.1 ms (a relative standard deviation of 6%). Over 15 days, we tracked two samples from parent 1 and one from parent 2. The mean λ_E for the batches of solutions 1 day since metal added to 15 decays from 1.63 ± 0.1 ms to 0.35 ± 0.13 ms, showing that confounding effects from decay can propagate and increase the relative uncertainty.

In the interest of reproducing similar results in another context, as well as searching

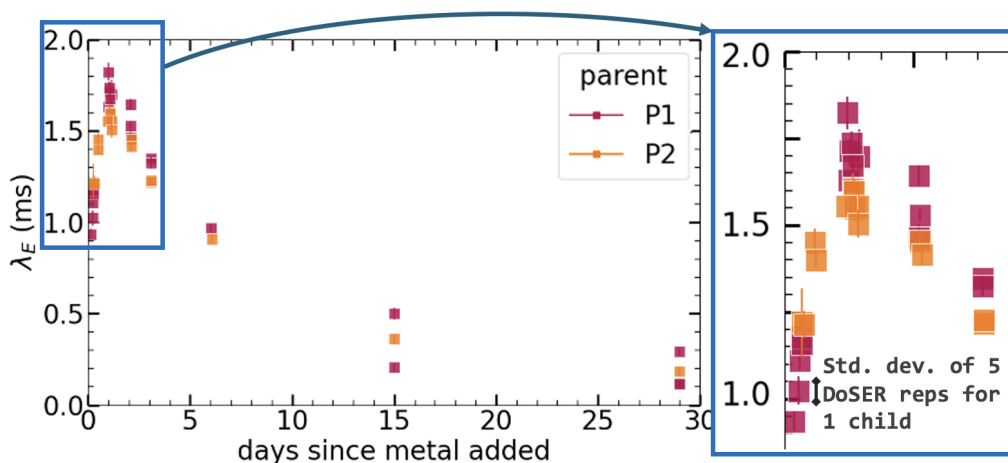


Figure A.2: λ_E over days since metal added for replicate solutions from two different parent solutions in acetic acid buffer (pH 5.6). For all samples taken on $d_m = 1$: $\lambda_E = 1.63 \pm 0.1$ ms.

$M_{umi} = 0.84$ MDa; solvent = acetic acid buffer (pH 5.6); $c = 0.04$ wt%; M:L = 0.5; $T_s = 22^\circ\text{C}$; Vial storage.

for potential ways to mitigate λ_E decay, we wanted to test another pH buffer. We tried a MOPS buffer of pH 7 on two parent solutions (Figure A.3). The MOPS child solutions from parent 2 fall within the bounds of those from parent 1, and in this case, the mean λ_E for $d_m = 1$ is now 0.77 ms with a standard deviation of 0.1 ms. The standard deviation is similar to that of the acetic acid buffer, but relatively speaking, it's a greater percentage when compared to the mean (relative standard deviation of 13%). However, we see a significant decrease in the maximum observed λ_E , in addition to no decay mitigation.

Next, we compare the acetic acid pH 5.6 and MOPS pH 7 buffers with un-buffered MilliQ water (Figure A.4). MilliQ water is typically between 5.6 to 6.8 due to exposure to carbon dioxide in air. We see that while the deviation between samples increases, so does the maximum λ_E relative to both buffers, in addition to a slower decay rate. We can dig deeper into the MilliQ experiments specifically, illuminating the variation that results from different parent, children, and handling conditions (i.e. how many times the solution is opened and exposed to air for sampling, the

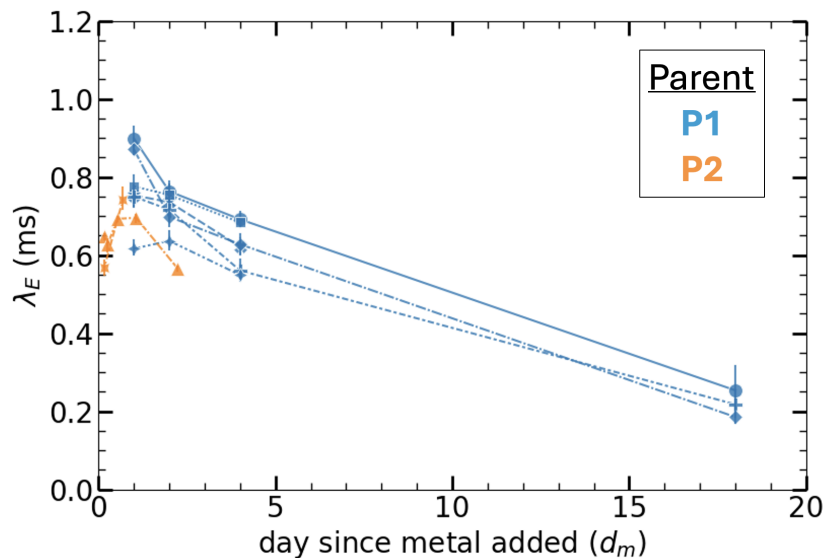


Figure A.3: λ_E over days since metal added for replicate solutions from two different parent solutions in MOPS buffer (pH 7). For all samples taken on $d_m = 1$: $\lambda_E = 0.77 \pm 0.1$ ms.

$M_{uni} = 0.84$ MDa; solvent = MOPS buffer (pH 7); $c = 0.04$ wt%; M:L = 0.5; $T_s = 22^\circ\text{C}$; Vial storage.

effects of which are described in Section 2.5).

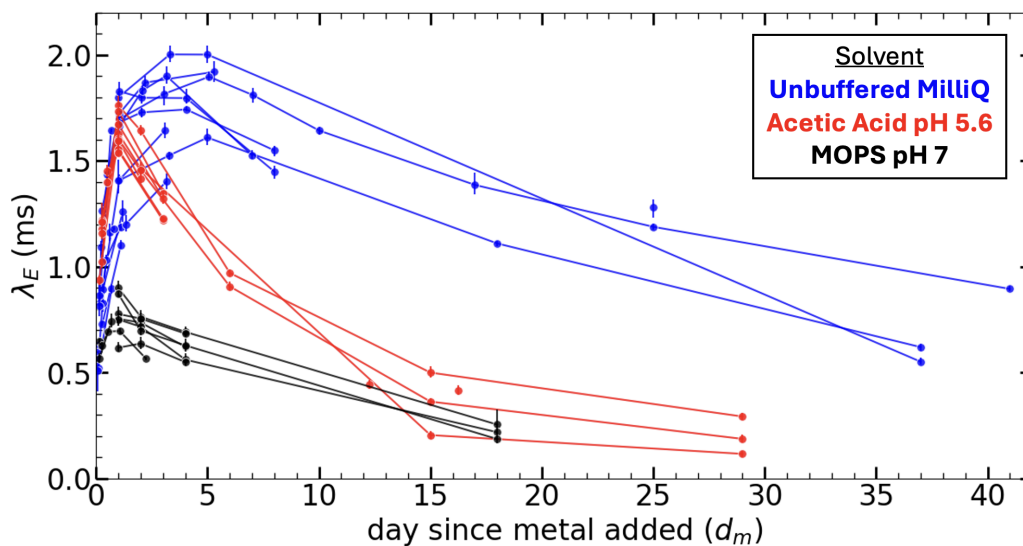


Figure A.4: λ_E over days since metal added for three different solvents: unbuffered MilliQ, acetic acid (pH 5.6), and MOPS (pH 7).

$M_{uni} = 0.84$ MDa; $c = 0.04$ wt%; M:L = 0.5; $T_s = 22^\circ\text{C}$; Vial storage.

The samples shown for unbuffered MilliQ come from a variety of solutions that

were made from four different parent solutions and exposed to varying amounts of air to capture the transient rise of λ_E at different time points (Figure A.5). Looking specifically at 1 day since metal added ($d_m = 1$), we see a mean λ_E of 1.55 ms and a standard deviation of 0.25 ms, which equates a relative standard deviation of 16%. This is higher than that of MilliQ and MOPS, but we're also considering a variety of parent solutions exposed to varying levels of air as the samples equilibrate to their maximum observed λ_E . We also emphasize that the samples considered here were prepared and examined over a range of 7 months. If we consider the same parent solution with the highest deviating child solutions (P3) that were both opened for the first time on $d_m = 1$, we get a relative standard deviation of 13%. This 13% uncertainty shall be considered when comparing solutions that were made from the same parent and sampled (i.e. exposed to air) the same number of times, while a 16% uncertainty is applied to cases where we compare samples that were made from different parent solutions. Both cases arise in Chapters 3 and 4, where we specify the represented uncertainty (indicated by shaded bands) and refer back to this Appendix. In Chapter 2, as we investigated TPAM degradation, we were primarily concerned with the trends seen in the rise and fall of λ_E over time instead of the absolute values of λ_E , so we use the standard deviation from the DoSER measurement in Chapter 2 figures (indicated by error bars).

We can compare the relative statistics for each buffer one day since metal added (Figure A.6). While unbuffered MilliQ has a larger uncertainty between replicate samples, it also represents a greater number of parent solutions and handling conditions. It also leads to the highest maximum observation of λ_E and a decrease in the decay rate. Buffers may also increase the chance of interference with metal-ligand dynamics (Section 2.6.3). For our exploratory studies on the effects of M:L ratio, unimer M_n , and concentration when metal is added (Chapters 4 and 5), we proceed with unbuffered MilliQ as our solvent, keeping in mind that we have shown here

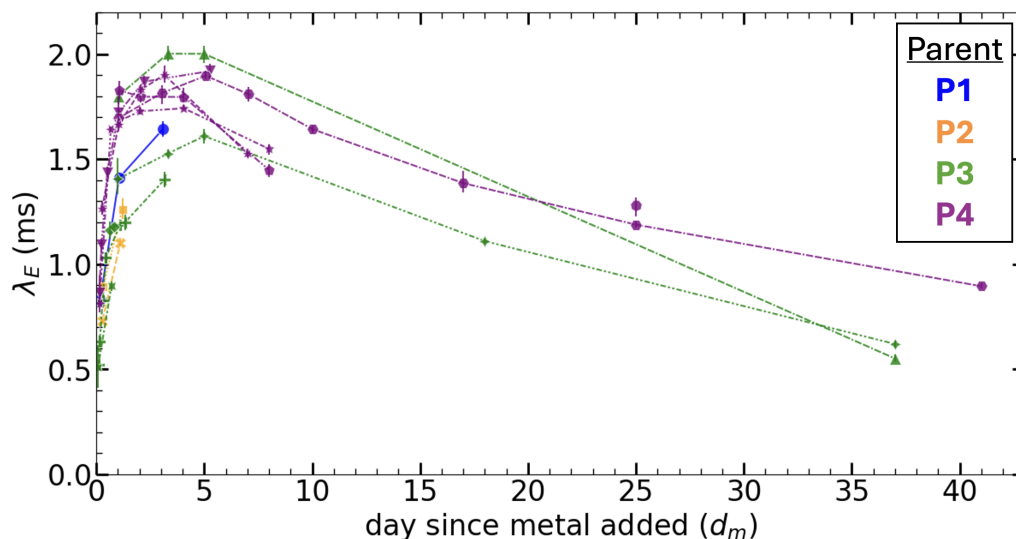


Figure A.5: λ_E over days since metal added for replicate solutions from four different parent solutions in unbuffered MilliQ water (typical pH range of 5.6 to 6.8). For all samples taken on $d_m = 1$: $\lambda_E = 1.55 \pm 0.25$ ms ($\pm 16\%$). For two child solutions from the same parent opened for the first time on $d_m = 1$: $\lambda_E = 1.63 \pm 0.22$ ms ($\pm 13\%$).

$M_{uni} = 0.84$ MDa; Solvent = unbuffered MilliQ; $c = 0.04$ wt%; M:L = 0.5; $T_s = 22^\circ\text{C}$; Vial storage.

that replicates made with the same parent solution and opened on the same day have exhibited a $\pm 13\%$ relative standard deviation, while solutions made with different starting solutions have exhibited a $\pm 16\%$ relative standard deviation. We remain cognizant of the possibility that the deviation may vary depending on the length of the megasupramolecules formed by changing the M:L ratio, unimer M_n , and concentration when metal is added. This change may be explored in future studies that wish to replicate the observations made in this thesis for more strict variance boundaries. To be transparent about the potential variation in the λ_E values that we have observed throughout our current data set, we apply the estimated uncertainties where appropriate. The uncertainties are given in figure captions, and a reference to the current appendix is given for more context.

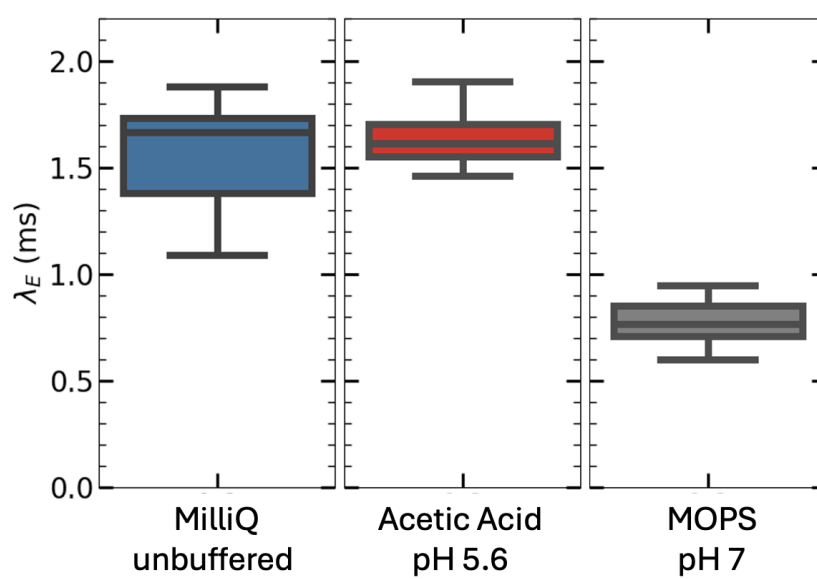


Figure A.6: Box and whisker plots for the statistics of λ_E variation on $d_m = 1$ for three different solvents: unbuffered MilliQ (4 parent solutions, $n_{samples} = 10$), acetic acid (pH 5.6) (2 parent solutions, $n_{samples} = 10$), and MOPS (pH 7) (2 parent solutions, $n_{samples} = 7$).

*Appendix B***DRAG REDUCTION AND CHAIN SCISSION INSTRUMENT DEVELOPMENT**

The experimental design for a polymeric drag reduction and mechanical chain scission study was conceptualized and constructed in a collaboration between Professor Beverley McKeon and Professor Julie Kornfield with their previous graduate students, Dr. Ryan McMullen, Dr. Huynh, and Dr. Red Lhota. In the current Appendix, I describe my contribution to the characterization of the instrument's drag reduction measurements, source of degradation, and particle image velocimetry (PIV) capabilities. After this validation step and subsequent improvements, using polyethylene oxide (PEO) I identified polymeric drag reduction structures using PIV at $Re_B \approx 7.5 \times 10^4$, which are shown in Chapter 1. I test PAM, PEO, and TPAM in the instrument to compare their drag reducing ability and susceptibility to chain scission.

B.1 Experimental Methods**B.1.1 Drag reduction instrument design and protocol**

The drag reduction instrument was designed to control and measure the mass flow rate and perform particle image velocimetry (PIV). The experiment also functions with as little as 3.5 kg of fluid, allowing for small batches of limited quantity polymers to be tested.

The solution is loaded into a supply tank, shown to the left in Figure B.1. The tank is supplied with compressed air, and pressure is regulated with an electronic pressure regulator (Proportion Air QB3) and measured with an electronic pressure gauge. After the sample is loaded and the tank is pressurized to the desired amount

(upper limit 80 psi), the automated ball valve is opened, the solution passes through flexible tubing and a quartz pipe, finally reaching a receiving tank where the mass flow rate is measured using a scale. These combined steps are considered one "pass" through the system. Once all the solution has been passed from the supply tank into the receiving tank, an air hose is connected to the receiving tank, and the solution is gently (<5 psi) transferred back into the supply tank. Once all of the solution is in the supply tank, the tank is pressurized, the the process is repeated for another "pass". This process is repeated for as many passes as desired for the experiment; in our case, 10 passes are performed on each solution.

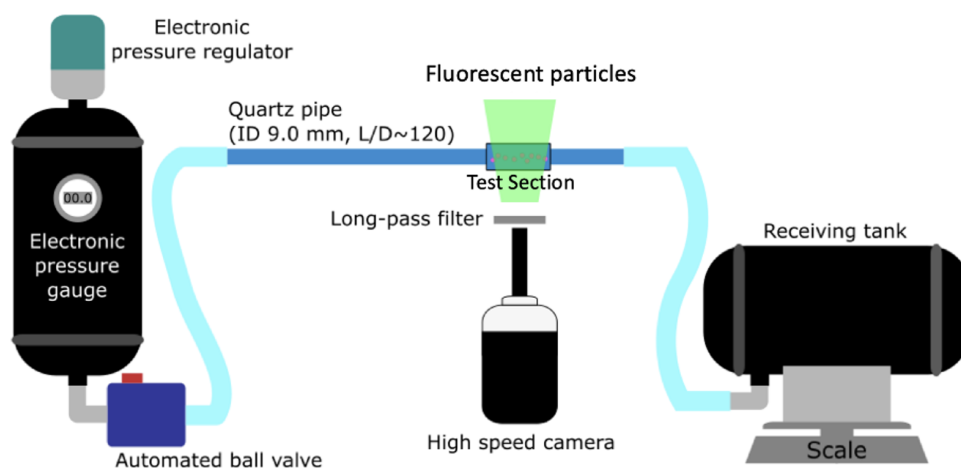


Figure B.1: Schematic of the drag reduction instrument, adapted from a DOW 2017 review by Dr. Ryan McMullen, Dr. David Huynh, and Dr. Red Lhota.

The quartz pipe contains an optical test section where PIV has been implemented to visualize flow structures. The tubing and pipe have an inner diameter of 8.8 cm. The flexible tubing between the quartz pipe and receiving tank can be interchanged to vary the total length and determine a pressure differential (dP) that excludes the head loss at the inlet (contraction) and outlet (expansion). The two total lengths were 4.27 m ("short") and 5.89 m ("long"). The pressure differential can be used to estimate the shear stress at the wall, which is integral to non-dimensionalizing the turbulence statistics obtained with PIV. Pressure taps were not implemented

to avoid any interference with the flow visualization in addition to avoiding the difficulties introduced with non-newtonian fluids. The drag reduction instrument was assembled by Dr. David Huynh and Dr. Ryan McMullen, and I adapted and validated it for the experiments presented in this chapter.

The use of pumps were avoided to limit shearing of the polymers, so that degradation is isolated at the contraction leaving the supply tank and the expansion entering the receiving tank. Dr. Red Lhota and I investigated the contraction and expansion degradation, and details on this procedure and results are reported in [2]. One benefit to having the degradation isolated to the supply tank exit and receiving tank entrance is that PIV data is taken on a steady solution (i.e. the polymer does not degrade over the length of the test section).

Dr. Red Lhota designed and prototyped the quartz test section which was manufactured by PGB Optical. Dr. Red Lhota designed and installed a custom Arduino-operated system and a LabVIEW graphical user interface for controlling and obtaining measurements with the electronic equipment. In collaboration with Dr. Lhota, I refined and rebuilt the custom electronics system to be more robust. I also enclosed all possible electrical components in a water-resistant enclosure for safety. I obtained all the mass flow rate and PIV measurements.

B.1.2 Polymer solutions and characterization

The polymers studied with the drag reduction instrument and discussed in the following sections are summarized in Table B.1.

Table B.1: Molecular weights (weight average and number average) for the polymers discussed in this chapter. HK: Synthesized by Dr. Hojin Kim.

Polymer	Mw	Mn	PDI	Source	Sample Name
PAM	6.70	5.00	1.3	HK	6.7M PAM
PEO	6.00	3.80	1.6	Dow WSR301	6M PEO
TPAM	0.9	0.84	1.1	HK	0.8 TPAM
TPAM + Ni(II)	6*	2*	1	HK	TPAM

For covalent 6.7 PAM and 6.0 PEO solutions, Dr. Red Lhota performed dripping onto substrate rheology (DoSER) and obtained the relaxation time. For the TPAM solutions, I performed DoSER and obtained the relaxation time (λ_E).

B.1.3 Drag reduction and degradation measurements

Reynolds number is calculated based on the mass flow rate, shown in Equation B.1.3. The bulk drag reduction is calculated based on the change in mass flow rate (or Re) caused by the polymer additives in comparison to that of water keeping the pressure drop constant at 40 PSI (Equation B.1.3). Drag reduction is typically calculated based on a change in the shear stress at the wall, but that measurement was not feasible for the current setup. Equation B.1.3 serves as a proxy for understanding the bulk effect of the polymer on the fluid's ability to flow through our apparatus at constant pressure. The mass flow rate is obtained by the scale and Arduino, exported as a csv, and analyzed with Matlab. The original code for data analysis in Matlab was written by Dr. Ryan McMullen and Dr. David Huynh, and I modified the code to account for multiple trials within the same pass through the system.

$$Re_B = \frac{4\dot{m}}{\pi\mu D} \quad (\text{B.1})$$

$$\%DR_B = \frac{\dot{m}_{poly} - \dot{m}_{water}}{\dot{m}_{water}} \quad (\text{B.2})$$

B.1.4 Particle Image Velocimetry (PIV) materials and methods

PIV is performed with a Photonics DM20-527(nm) YLF laser (double pulse, double exposure) and Phantom Miro 320 high-speed camera. DaVIS was used to process the raw images, and Matlab was used to process the instantaneous velocity data output from DaVIS.

Calibration was performed with a replicate of the quartz tube test section, called "the calibration section". The calibration section has the same cross sectional dimensions as the test section but is 10 inches long for ease of calibration target installation and alignment. Initially, the procedure involved mounting a 0.9x0.9x0.02cm tab with a printed dot pattern onto an acrylic rod, which was then inserted into the calibration section and aligned in the axial, span-wise, and wall normal directions. The calibration section was filled with water to and sealed with parafilm to replicate the index of refraction conditions present in the tests. This target and procedure was later modified to address distortion near the wall, as described in the following sections.

Non-dimensionalized mean velocity and variance profiles (Equations B.3 and B.4) are calculated based on the shear stress at the wall which is approximated by the pressure differential over a given pipe length, shown in Equation B.5.

$$u^+ = \sqrt{\frac{u}{u_\tau}} \quad (\text{B.3})$$

$$y^+ = y \sqrt{\frac{u_\tau}{\nu}} \quad (\text{B.4})$$

$$u_\tau = \sqrt{\frac{\tau_w}{\rho}} \approx \sqrt{\frac{(\Delta P)D}{4L\rho}} \quad (\text{B.5})$$

B.2 Initial PIV: Comparison to canonical flow, improvements, and under-resolved near-wall statistics

PIV was first performed with the previously existing experimental materials and protocol. My first round of PIV data spanned the entire pipe diameter, and results are shown for the top profile and the bottom profiles (above and below the center-line, respectively) (Figure B.2). Results show that the top and bottom velocity profiles overlap, indicating that asymmetry is achieved. However, comparison of the variance profiles show a significant deviation from the canonical flow. This deviation occurs

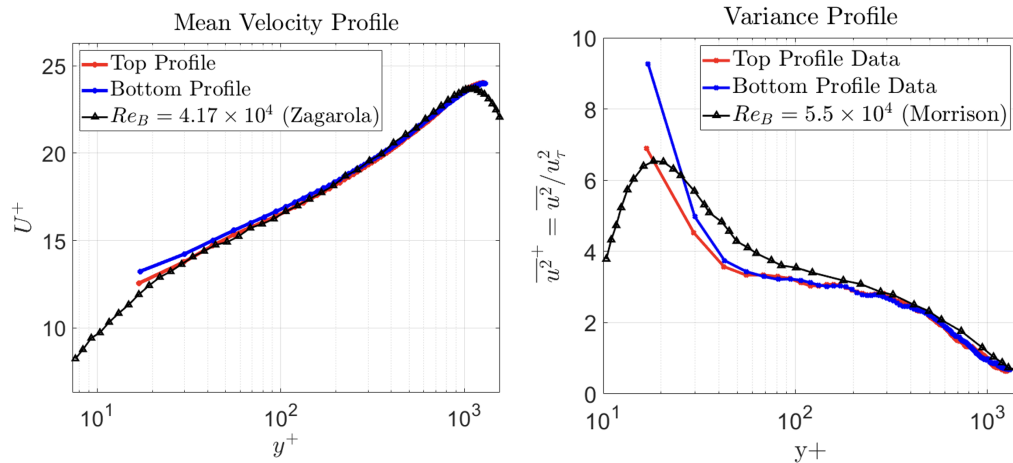


Figure B.2: First round of non-dimensionalized mean velocity and variance profiles of water at $Re_B = 5.2$, based on PIV data taken with the first calibration target (Figure B.3). Mean profile is compared to [3] and variance is compared to [4]. Top and bottom profiles indicate axisymmetric flow, with some deviation from canonical flow near the wall. Final iteration of improved profiles shown are shown in Figure B.4

around $y^+ = 150$, corresponding to the edges of the calibration target. In our setup, the calibration target was not only used to convert between pixels and millimeters, but also to correct for the image distortion with built-in DaVis software. The curved glass with refractive index mismatch between the water, glass, and air distorts the image, and the high zoom lens causes a commonly encountered "pin cushion" distortion. DaVis is capable of correcting these distortions, but only so far as the calibration target covers the distorted area. Being that the highest distortion occurs near the pipe walls, it was crucial to redesign the target to extend closer to the wall to obtain more accurate results in the near-wall region.

The calibration target was completely redesigned to be printed on a thin-film and mounted on a rod with a flat surface cut through the center. The improved target is able to reach much closer to the wall in comparison to the original (Figure B.3). Since axisymmetry was already exhibited in the first round of results, we zoomed in on the bottom wall as much as possible to focus on improving the spatial

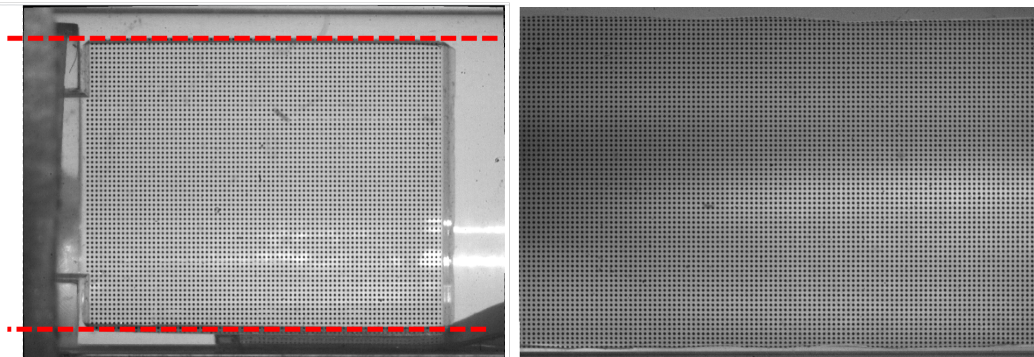


Figure B.3: Left: Original calibration target, with red dashed lines highlighting the edges and its distance from the pipe wall. Right: New calibration target reaching the pipe wall.

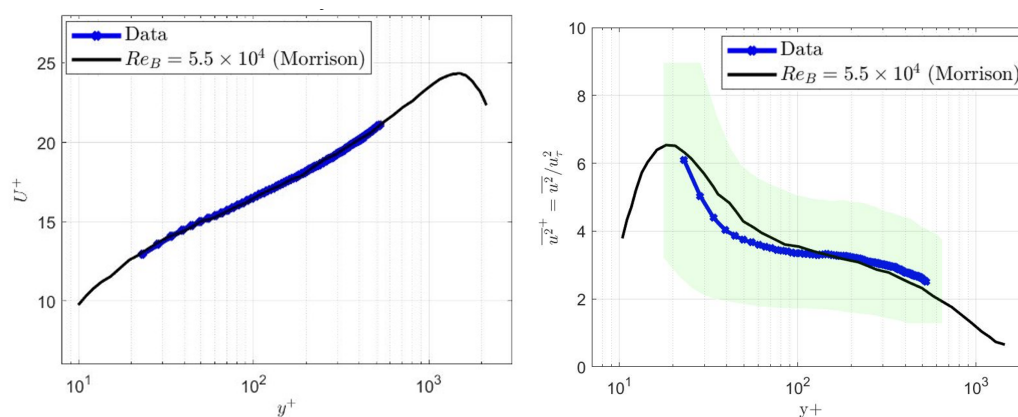


Figure B.4: Improved non-dimensionalized mean velocity and stream-wise variance profiles.

resolution. The match to canonical flow is closer for the new target and higher spatial resolution—mean velocity is spot on, but stream-wise variance is still low near the wall (Figure B.4).

We realized the low stream-wise variance may be due to the spatial averaging that occurs during PIV, and the higher energy fluctuations could be getting averaged out. Work by [5] studies this very issue, so we implement their techniques to gain insight on the source of our under-resolved intensities. The method uses DNS data generated with the same y^+ spatial resolution (SR) to find the missing energy, and uses that to estimate what the reference fluctuation profile would be at the same

resolution. With PIV set at 50% overlap and 98x98 pixel resolution, we had a y^+ spatial resolution of 50. We used the database of missing energies provided by [5] to "correct" the reference profile to account for the missing energy in our PIV setup, which shows that our inability to resolve the fluctuations at the wall was likely due to the spatial averaging (Figure B.5). While this limitation stopped us from pursuing the investigation into changing turbulence statistics with polymeric drag reduction, we still wanted to use PIV to more qualitatively assess the flow structures created within our apparatus.

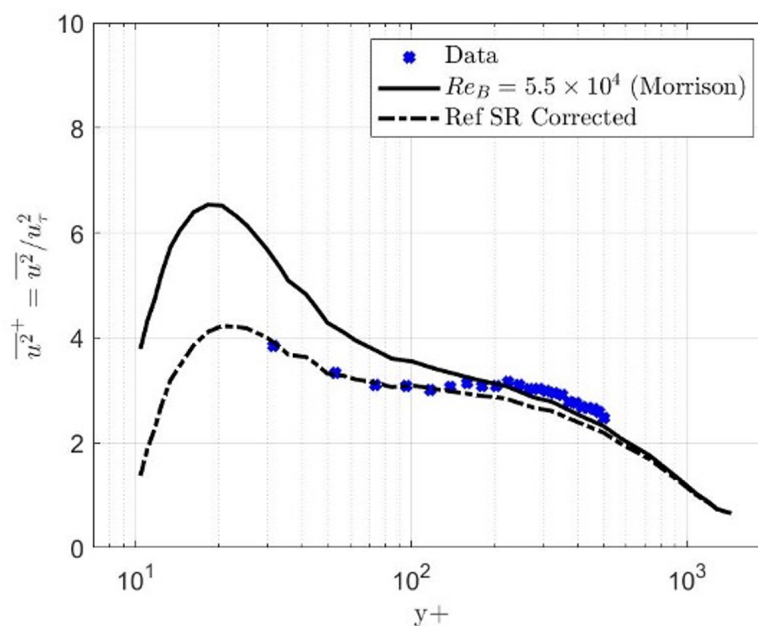


Figure B.5: Stream-wise variance data compared to adjusted reference profile. 50% overlap, 98x98 pixel resolution (y^+ SR 50. [5])

B.3 Identification of polymer-induced drag reduction structures

We compare the vorticity fields of deionized (DI) water and polymeric-induced drag reduction using polyacrylamide (PAM) at a concentration of 66 ppm. The experiments were conducted at 40 PSI, resulting in a bulk Reynolds number (Re) of 53,000 for DI water and 75,000 for the 66 wppm 6 MDa PEO solution.

For DI water, the vorticity field exhibits a multitude of small vortices near the

wall, indicative of the turbulent nature of the flow. These small-scale vortices are characteristic of high turbulence intensity and energy dissipation near the boundary layer. However, the introduction of PAM at 66 ppm not only increases the Re_B by 30%, but it also alters the vorticity structure. The drag reduction run reveals a clear reduction in the number of small-scale vortices. Instead, the flow exhibits high-strength, more coherent, and elongated inclined shear layers. These observations are consistent with the findings of AbdeIKader et al. (2022) [6], which build upon the foundational work of Zadrazil et al. (2012) [7], confirming that our experiment successfully induces polymeric drag reduction.

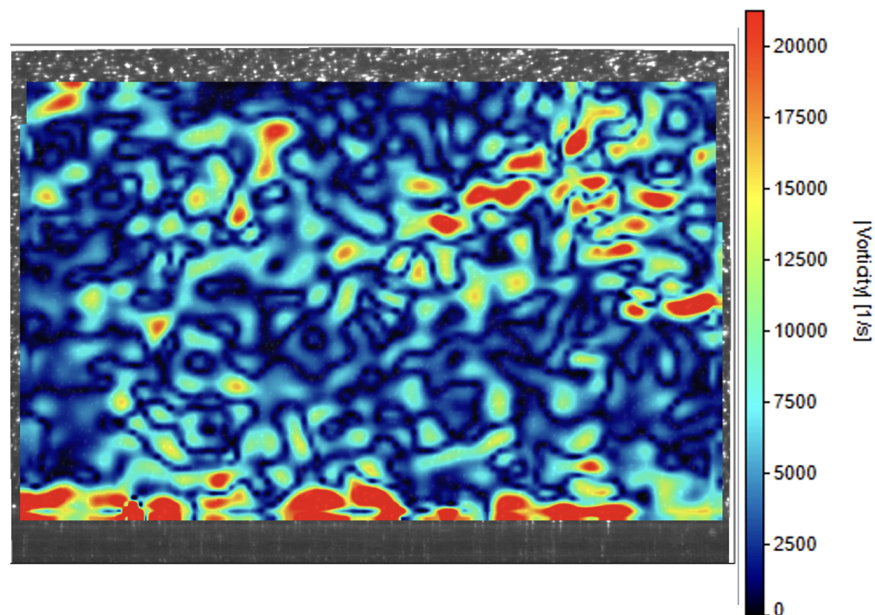


Figure B.6: Instantaneous vorticity map of DI water ($Re_B = 5.2 \times 10^4$).

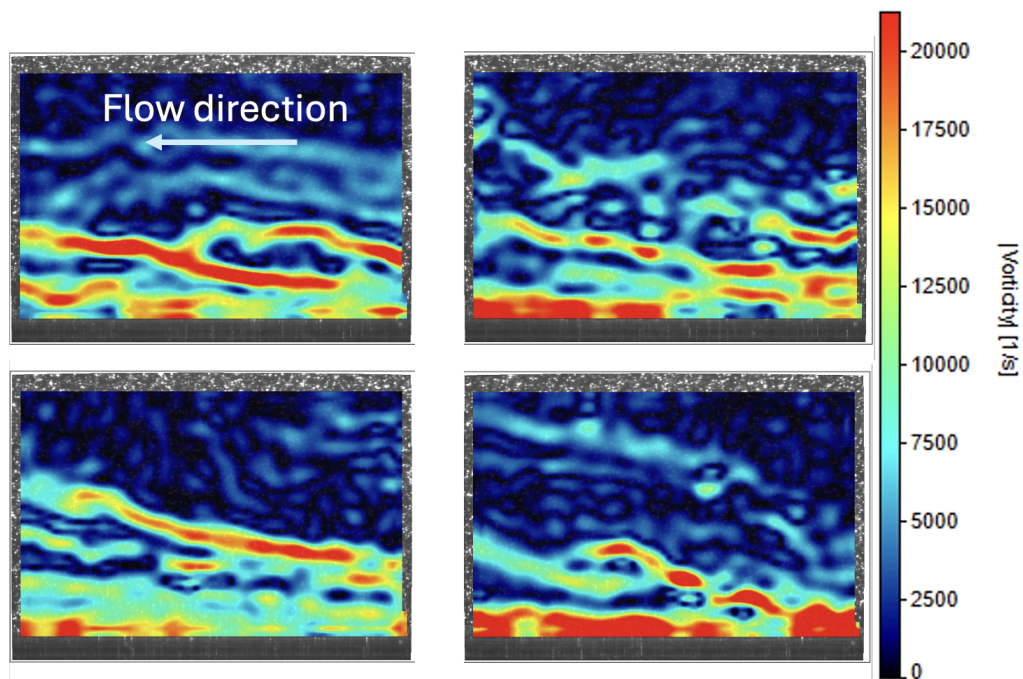


Figure B.7: Instantaneous vorticity maps of 6M PEO during the first pass through the drag reduction instrument ($Re_B = 7.5 \times 10^4$). Key changes between the newtonian (Fig B.6) and non-newtonian polymeric drag reduced flow shown in this figure are observed, namely the reduction in the amount of smaller scale vortices and higher strength, inclined, shear layers.

Appendix C

DOSER EQUATION DERIVATION FOR DETERMINING λ_E

Dripping onto Substrate Extensional Rheometry (DoSER) calculates λ_E based on a the fluid's filament diameter changing over time in the elasto-capillary regime. To derive this equation, which is presented in Chapter 1, we start with a constitutive model for a non-Newtonian, viscoelastic fluid, the Chilcott - Rallison version of the FENE equations. For the particular case of a stretching flow of a thin cylindrical element of polymeric fluid we have [8]:

$$\frac{dA}{dt} = 2EA - \frac{A}{\lambda} \quad (\text{C.1})$$

where A is the axial component of the elastic deformation tensor, E is the axial stretching rate, and λ is the relaxation time. The elastic stress σ_E is related to the elastic deformation via the elastic modulus G :

$$\sigma_E = GA \quad (\text{C.2})$$

Considering a thin cylindrical bridge of a polymeric fluid with diameter D , if the volume is assumed constant then we have:

$$E = -\frac{2}{D} \frac{dD}{dt} \quad (\text{C.3})$$

Substitute (C.3) in (C.1) we get:

$$\frac{dA}{dt} = -\frac{4A}{D} \frac{dD}{dt} - \frac{A}{\lambda} \quad (\text{C.4})$$

Multiply by dt , divide by A , and integrate from t_0 to t :

$$\ln\left(\frac{A}{A_0}\right) = \ln\left(\frac{D_0}{D}\right)^4 - \frac{(t-t_0)}{\lambda} \quad (\text{C.5})$$

$$A = \left(\frac{D}{D_0}\right)^4 e^{-(t-t_0)/\lambda} \quad (\text{C.6})$$

where the initial condition at t_0 is $A_0 = 1$ because the fluid is initially undeformed.

From the axial force balance on a cylindrical fluid element, the axial stress σ_{xx} equals the hydrostatic pressure p plus the elastic stress σ_E :

$$\sigma_{xx} = -p + \sigma_E \quad (\text{C.7})$$

For radial force balance, the capillary pressure is equal to the hydrostatic pressure:

$$\frac{-2\alpha}{D} = \sigma_{rr} = -p \quad (\text{C.8})$$

where α is the surface tension. Substituting (C.8) into (C.7) we get:

$$\sigma_{xx} = \frac{-2\alpha}{D} + \sigma_E \quad (\text{C.9})$$

Experimental measurements of the filament tension show the axial stress is small compared to the capillary pressure [8], so we can assume:

$$\frac{2\alpha}{D} = \sigma_E \quad (\text{C.10})$$

Substituting (C.2) into the above we get:

$$\frac{2\alpha}{D} = GA \quad (\text{C.11})$$

Substituting (C.11) into (C.6) we get:

$$\frac{2\alpha}{D} = G \left(\frac{D}{D_0} \right)^4 e^{-(t-t_0)/\lambda} \quad (\text{C.12})$$

With some algebra, we find the commonly used expression:

$$\frac{D}{D_0} = \left(\frac{GD_0}{2\alpha} \right)^{1/3} e^{-(t-t_0)/3\lambda} \quad (\text{C.13})$$

BIBLIOGRAPHY

- [1] Robert Learsch. “Droplet control in aqueous and hydrocarbon fluids: Long, end-associative polymers dictate fluid behavior under elongational flows”. PhD thesis. Caltech, Oct. 20, 2022.
- [2] Red C. Lhota. “Rheological Characterization of Polymer Additives for Mist Control and Drag Reduction”. Medium: PDF Version Number: Final. PhD thesis. California Institute of Technology, May 27, 2022. DOI: [10.7907/WAV1-4T47](https://doi.org/10.7907/WAV1-4T47).
- [3] Mark V. Zagarola and Alexander J. Smits. “Mean-flow scaling of turbulent pipe flow”. In: *Journal of Fluid Mechanics* 373 (Oct. 25, 1998), pp. 33–79. ISSN: 0022-1120, 1469-7645. DOI: [10.1017/S0022112098002419](https://doi.org/10.1017/S0022112098002419).
- [4] J. F. Morrison et al. “Scaling of the streamwise velocity component in turbulent pipe flow”. In: *Journal of Fluid Mechanics* 508 (June 10, 2004), pp. 99–131. ISSN: 0022-1120, 1469-7645. DOI: [10.1017/S0022112004008985](https://doi.org/10.1017/S0022112004008985).
- [5] J. H. Lee et al. “Validating under-resolved turbulence intensities for PIV experiments in canonical wall-bounded turbulence”. In: *Experiments in Fluids* 57.8 (Aug. 2016), p. 129. ISSN: 0723-4864, 1432-1114. DOI: [10.1007/s00348-016-2209-6](https://doi.org/10.1007/s00348-016-2209-6).
- [6] Mohamed AbdElKader et al. “Development of Drag-reduced Turbulent boundary layers on smooth walls with different polymer concentrations”. In: 12th International Symposium on Turbulence and Shear Flow Phenomena (TSFP12). July 19, 2022.
- [7] I. Zadrazil et al. “Shear layers in the turbulent pipe flow of drag reducing polymer solutions”. In: *Chemical Engineering Science* 72 (Apr. 2012), pp. 142–154. ISSN: 00092509. DOI: [10.1016/j.ces.2011.12.044](https://doi.org/10.1016/j.ces.2011.12.044).
- [8] V.M. Entov and E.J. Hinch. “Effect of a spectrum of relaxation times on the capillary thinning of a filament of elastic liquid”. In: *Journal of Non-Newtonian Fluid Mechanics* 72.1 (Sept. 1997), pp. 31–53. ISSN: 03770257. DOI: [10.1016/S0377-0257\(97\)00022-0](https://doi.org/10.1016/S0377-0257(97)00022-0).